

MICRO-/NANOFABRICATION IN ANALYTICAL CHEMISTRY AND
TEMPERATURE DEPENDENT STUDIES OF UNDERPOTENTIAL
DEPOSITION OF MERCURY(II) ON AU(111)

Lunsheng Zhang

Certificate of Approval:

Vince Cammarata
Associate Professor
Chemistry & Biochemistry

Curtis G. Shannon Chair
Professor
Chemistry & Biochemistry

Evert C. Duin
Assistant Professor
Chemistry & Biochemistry

Barton Prorok
Assistant Professor
Materials Engineering

George T. Flowers
Dean
Graduate School

MICRO-/NANOFABRICATION IN ANALYTICAL CHEMISTRY AND
TEMPERATURE DEPENDENT STUDIES OF UNDERPOTENTIAL
DEPOSITION OF MERCURY(II) ON AU(111)

Lunsheng Zhang

A Dissertation
Submitted to
the Graduate Faculty of
Auburn University
in Partial Fulfillment of the
Requirements for the
Degree of
Doctor of Philosophy

Auburn, Alabama
May 10, 2007

MICRO-/NANOFABRICATION IN ANALYTICAL CHEMISTRY AND
TEMPERATURE DEPENDENT STUDIES OF UNDERPOTENTIAL
DEPOSITION OF MERCURY(II) ON AU(111)

Lunsheng Zhang

Permission is granted to Auburn University to make copies of this dissertation at its discretion, upon request of individuals or institutions and at their expense. The author reserves all publication rights.

Signature of Author

Date of Graduation

VITA

Lunsheng Zhang (Allan), son of Jiwen Zhang and Miaozen Li was born on December 03, 1975 in Zhouning County, Fujian province, People's Republic of China. He graduated from Zhouning 2nd High School in 1992. He then attended China Textile University (now Donghua University) in Shanghai, China for four years and graduated with a Bachelor of Science degree in Applied Chemistry in July 1999. He entered the graduate school at China Textile University in September 1999, and graduated with a Master of Science degree in Applied Chemistry in April 2002. He entered the Chemistry department graduate program at Auburn University in September 2002 to pursue a Doctoral degree in Analytical Chemistry. He married Huiqing Liu (Allanie) on May 15 2002, and they have a daughter Allison L. Zhang.

MICRO-/NANOFABRICATION IN ANALYTICAL CHEMISTRY AND
TEMPERATURE DEPENDENT STUDIES OF UNDERPOTENTIAL
DEPOSITION OF MERCURY() ON AU(111)

Lunsheng Zhang

Doctor of Philosophy, May 10, 2007
(M.S., Donghua University, 2002)
(B.S., Donghua University, 1999)

169 Typed Pages

Directed by Curtis Shannon

This dissertation studies three routes to fabricate micro-/nano-sized structures for the purpose of analytical chemistry and the underpotential deposition (UPD) of mercury(II) onto Au(111) electrodes.

In Chapter 2, we have studied the temperature dependence of the underpotential deposition (UPD) of mercury(II) onto Au(111) electrodes from a series of electrolytes in which anion interactions could be varied from essentially zero (i.e., HClO₄) to strongly interacting with either the Au(111) substrate (i.e., H₂SO₄) or with solution phase Hg²⁺

ions (i.e., $\text{HC}_2\text{H}_3\text{O}_2$). Both isothermal and non-isothermal cells were used to make temperature dependent cyclic voltammetry measurements.

In Chapter 3, the two-component mixed self-assembled monolayers consisting of 4-aminothiophenol (4-ATP) and n-decanethiol (DT) were studied and the random arrays of polyaniline nano-/microelectrodes were fabricated based on the mixed SAMs. The features of the polyaniline nano-/microelectrodes were characterized and compared with theoretical results. A biosensor using the SAM-based polyaniline electrodes was tested and the preliminary results were discussed.

In Chapter 4, the nanosphere lithography combined with electrochemical deposition is demonstrated to be a powerful technique that is able to produce inexpensive parallel nanostructures with fine resolution. Several nanostructures including pores, particles and rings were made through nanosphere lithography templates. A process of growing the pore film was given based on the AFM analysis. The pore size of the film could be controlled by the sphere size and the condition of electrochemical deposition.

In Chapter 5, the connection of copper, silver and semiconductor CdSe microwires between anode and cathode was created through electrochemical deposition. The electrochemical reactions were studied. The semiconductor microwire has the potential of being applied in the detection of biomolecules

ACKNOWLEDGEMENTS

The author would like to thank Dr. Curtis Shannon for his assistance, mentorship, and guidance during the entire course of this research. Sincere gratitude and appreciation is also extended to the committee members and outside reader for their time, effort and insightful suggestions during the preparation of this manuscript. Much appreciation is also extended to the Shannon group members: Serdar, Tamer, Yuming, Qing, Joseph, Anand, Sunny, Amy, Chaokang, Weiping and Sridevi.

The author would also like to thank the members of his family: Dad, Mum, for their encouragement throughout the duration of this study.

Lastly, the author would like to express special thanks to his wife, Allaney for her support, love, care and concern during the graduate studies.

Style manual or journal used Journal of American Chemical Society

Computer Software used Microsoft Excel, Microsoft Word 6.0, Origin Pro 6.0, PSI-ProScan 1.41b

TABLE OF CONTENTS

LIST OF TABLES	xiii
LIST OF FIGURES	xiv
1. INTRODUCTION	
1.1 Nanomaterials in analytical chemistry	1
1.1.1. Nanomaterials in optical sensors	2
1.1.2. Nanomaterials in electrochemical sensors	5
1.1.3. Nanomaterials in separations and extraction techniques	5
1.2 Nanosphere Lithography	8
1.2.1 Fabrications	9
1.2.2 Applications	10
1.2.2.1 NSL as surfaces	10
1.2.2.2 NSL as masks	10
1.2.2.3 Fabrications with Reactive Ion Etching Variant of Nanosphere Lithography	13
1.2.2.4 Fabrication of Macroporous Materials	14
1.2.2.5 Other applications	14
1.3 Self-Assembled Monolayers (SAMs)	15

1.3.1	Formation of SAMs	16
1.3.2	Characterization of SAMs	17
1.3.3	Mixed SAMs	19
1.3.4	Applications of SAMs in nanoscience and nanotechnology	19
1.4	Polyaniline (PANI)	20
1.4.1	Structure of PANI	21
1.4.2	Polymerization of aniline	22
1.4.2.1	Chemical polymerization	22
1.4.2.2	Electropolymerization	23
1.5	References	25
2.	THE INFLUENCE OF COUNTER ANIONS ON THE UNDERPOTENTIAL DEPOSITION OF MERCURY(II) ON AU(111): TEMPERATURE DEPENDENT STUDIES	
2.1	Introduction	34
2.2	Experimental	36
2.3	Results and Discussion	39
2.3.1.	Room Temperature Cyclic Voltammetry	39
2.3.2.	Temperature Dependent Studies	44
2.3.3.	Hg UPD from perchloric acid and sulfuric acid	49
2.3.4.	Hg UPD from acetic acid	51
2.4	Conclusion	54

2.5 Reference	55
3. STUDY OF POLYANILINE NANO-ELECTRODE ASSEMBLES GROWN ON DECANETHIOL/4-AMINOTHIOPHENOL MIXED MONOLAYERS	
3.1 Introduction	58
3.2 Experimental	60
3.3 Results and Discussion	63
3.3.1 Investigation of two-component mixed SAMs containing 4-ATP and DT	63
3.3.2 Fabrication of polyaniline nanoelectrode ensemble through the electropolymerization of aniline on 4-ATP/DT surfaces	74
3.3.3 AFM characterization of aniline nanoelectrode arrays	76
3.3.4 Theoretical simulation for polyaniline electrode arrays	79
3.3.5 Study the binding between polyaniline and protein	84
3.3.6. Investigation the efficiency of protein immobilization on SAM-polyaniline electrodes	88
3.4 Conclusions	91
3.5 References	92
4. FABRICATION OF FILMS CONTAINING PERIODIC NANOFEATURES BASED ON NANOSPHERE LITHOGRAPHY	
4.1 Introduction	95
4.2 Experimental	97
4.3 Results and Discussion	99
4.3.1 Nanosphere template	99

4.3.2. Periodic pore-array film	100
4.3.3. Periodic particle-array film electrochemically deposited through a 600 nm diameter sphere template	118
4.4 Conclusions	120
4.5 References	122
5. WIRE CONNECTIONS BETWEEN ANODE AND CATHODE THROUGH DIRECT ELECTRODEPOSITION	
5.1 Introduction	124
5.2 Experimental	127
5.3 Results and Discussion	128
5.3.1 Growth of copper wire between copper-copper electrodes	128
5.3.2 Growth of other wires between copper-copper electrodes	132
5.3.3 Growth of copper wires between copper-gold electrodes	136
5.3.4. Resistance of CdSe wire in aqueous solution containing electrolytes	139
5.4 Conclusions	145
5.5 References	146
6. CONCLUSIONS AND FUTURE WORK	148

LIST OF TABLES

Table 1.1	Fractional content of amine vs nomenclature of polyaniline.	22
Table 2.1	Summary of Hg UPD thermodynamic data obtained from temperature-dependent cyclic voltammetry measurements	46
Table 3.1	Number density and average radius of polyaniline electrodes on 4-ATP from AFM analysis.	79
Table 3.2	The number density and radius of polyaniline electrodes from fitting results and from AFM measurement.	82
Table 3.3	Surface coverage of polyaniline electrodes or surface coverage of 4-aminothiophenol (4-ATP)	83
Table 4.1	The components of the aqueous plating solutions and the potential applied.	98
Table 4.2	The value of r_b , h_{calc} and D/r_b for the copper films deposited through three different templates.	109
Table 5.1	Experimental conditions of electrochemical deposition	132
Table 5.2	Charge of copper deposited	139

LIST OF FIGURES

Figure 1.1	Mechanism of formation of conducting polyaniline	24
Figure 2.1	Room temperature cyclic voltammetry of an Au(111) electrode immersed in 0.10 M HClO ₄ + 1.0 mM Hg ²⁺ in the UPD region. The scan rate was 1 mV/s	40
Figure 2.2	Room temperature cyclic voltammetry of an Au(111) electrode immersed in 0.10 M H ₂ SO ₄ + 1.0 mM Hg ²⁺ in the UPD region. The scan rate was 1 mV/s	41
Figure 2.3	Room temperature cyclic voltammetry of an Au(111) electrode immersed in 0.10 M HC ₂ H ₃ O ₂ + 1.0 mM Hg ²⁺ in the UPD region. The pH of each solution is indicated on the graph. The scan rate was 1 mV/s in all cases	42
Figure 2.4A	Temperature dependent cyclic voltammetry of an Au(111) electrode immersed in 0.10 M HClO ₄ + 1.0 mM Hg ²⁺ in the UPD region. The temperature range was from 298 K to 358 K. Arrows indicate the direction that the peaks shift. The scan rate was 1 mV/s.	45
Figure 2.4B	Plots of $j_{p,cathodic}$ (left hand y-axis) and q_{ads} (right hand y-axis) as a function of temperature	47
Figure 2.4C	Determination of dE_{UPD}/dT values using $E_{p,cathodic}$ (filled circles) and E_f° (open circles)	48
Figure 2.5	Plot of experimental values of ΔS_{UPD} (circles) and ΔH_{UPD} (triangles) versus the calculated free mercury(II) concentration. See text for details	53
Figure 3.1	Voltammetric behavior of (a) 4-aminothiophenol (4-ATP) and (b) decanethiol (DT) single-component SAMs on Au in a solution containing 1 mM K ₃ Fe(CN) ₆ and 0.5 M Na ₂ SO ₄ supporting electrolyte.	64

Figure 3.2	Voltammetric behavior of a 4-aminothiophenol (4-ATP) monolayer on Au in a solution containing 100 mM HClO ₄ electrolyte. The anodic wave (A) at 0.73V corresponds to the oxidation of 4-ATP to the cation radical	66
Figure 3.3	Plot of surface coverage of 4-aminothiophenol in mixed SAM as a function of the molar fraction of 4-aminothiophenol in solution, based on the anodic peak (at 0.73 V) height of 4-aminothiophenol (4-ATP) in a solution containing 100 mM HClO ₄ .	67
Figure 3.4	Voltammetric behavior of the mixed SAMs on Au in a solution containing 1 mM K ₃ Fe(CN) ₆ and 0.5 M Na ₂ SO ₄ supporting electrolyte. The mole fractions of decanethiol (DT) in the assembling solutions were (a) 0.0, (b) 0.5, (c) 0.67, and (d) 1.0.	70
Figure 3.5	Plot of surface coverage of decanethiol in mixed SAM as a function of the mole fraction of decanethiol in solution.	72
Figure 3.6	Plots of (a) ◆ surface coverage of 4-ATP, (b) ■ surface coverage of DT as the functions of the mole fraction of 4-aminothiophenol in solution.	73
Figure 3.7	Voltammetric behavior of a 4-aminothiophenol (4-ATP) monolayer on Au immersed in a solution containing 100 mM aniline and 100 mM HClO ₄ supporting electrolyte. The anodic wave at 0.97 V corresponds to the oxidation of solution phase aniline to the aniline cation radical. The smaller wave at 0.73V is assigned as the one electron oxidation of 4-ATP to its cation radical.	75
Figure 3.8	AFM image of polyaniline nanoelectrode assemble. The mole fraction of 4-ATP in assembling solution is 0.4. The surface coverages of 4-ATP is 0.0834. The scale bar = 1 μm.	77
Figure 3.9	AFM image of polyaniline nanoelectrode assemble. The mole fraction of 4-ATP in assembling solution is 0.7. The surface coverages of 4-ATP is 0.3600. The scale bar = 1 μm.	78
Figure 3.10	Plots of I vs t ^{-1/2} obtained by chronoamperometry with polyaniline nanoelectrode arrays with surface coverages of 4-ATP of 0.360, 0.136, 0.0834, 0.0424, 0.0230. Solid curves are the theoretical ones.	81
Figure 3.11	Voltammetric behavior of Ru(NH ₃) ₆ Cl ₃ on oxidized polyaniline (a) before and (b) after reacting with decanethiol.	86

Figure 3.12	Voltammetric behavior of $\text{Ru}(\text{NH}_3)_6\text{Cl}_3$ on oxidized polyaniline (a) no reaction, (b) after reacting with glycine for 5 min, and (c) after reacting with glycine for 30 min	87
Figure 3.13	Plot of polyaniline peak current as a function of the mole fraction of 4-aminothiophenol in mixed SAM.	89
Figure 3.14	Plot of protein-polyaniline binding efficiency as a function of the mole fraction of 4-aminothiophenol in mixed SAM.	90
Figure 4.1	AFM image of the template spin-coated from 600(\pm 20) nm diameter polystyrene spheres	101
Figure 4.2	Periodic porous films electrochemically deposited through the sphere template. The diameter of the sphere = 600(\pm 20) nm	103
Figure 4.3	Periodic porous films electrochemically deposited through the sphere template. The diameter of the sphere = 3600(\pm 20) nm.	104
Figure 4.4	Terms of the film. (a) The schematic top view of the periodic pore film. The white circular areas are the pores, which is previously occupied by polystyrene spheres. (b) The schematic cross section view of an ideal spherical pore in the periodic pore film. (c) Wetting. (d) The schematic cross section view of a real pore.	106
Figure 4.5	Plots of r_o as the functions of film thickness. (a) \blacktriangle measured value, $r_s = 300\text{nm}$, (a') calculated value, $r_s = 300\text{nm}$, (b) \blacksquare measured value, $r_s = 500\text{nm}$, (b') calculated value, $r_s = 500\text{nm}$, (c) \blacklozenge measured value, $r_s = 1800\text{nm}$, (c') calculated value, $r_s = 1800\text{nm}$.	107
Figure 4.6	Film thickness as a function of electrochemical deposition time. The diameter of the sphere on the template is 600(\pm 20) nm.	108
Figure 4.7	Cyclic Voltammetric behavior of ZnO pore film in 1mM $\text{K}_3\text{Fe}(\text{CN})_6$ and 0.5 M Na_2SO_4 with various scan rates	110
Figure 4.8	AFM image of copper film containing the areas previously covered or uncovered by polystyrene template. The diameter of the sphere = 600(\pm 20) nm.	112
Figure 4.9	AFM image of copper deposited on gold surface through sphere template. The diameter of the sphere = 600(\pm 20) nm. Potential = -100 mV. Time = 3 seconds	114

Figure 4.10	AFM image of copper deposited on gold surface through sphere template. The diameter of the sphere = 600(\pm 20) nm. Potential = -100 mV. Time = 8 seconds	115
Figure 4.11	AFM image of copper deposited on gold surface through sphere template. The diameter of the sphere = 600(\pm 20) nm. Potential = -100 mV. Time = 2 seconds. CTAB/methanol (1:200 by mass), was used to dilute the nanosphere suspension before the template preparation.	117
Figure 4.12	Periodic particle array electrochemically deposited through a 600(\pm 20) nm diameter sphere template	119
Figure 5.1	Diagram of wire formation between two particles under bipolar conditions.	126
Figure 5.2	Diagram of wire formation between two metal electrodes	129
Figure 5.3	Chronoamperometric curve of copper wire growth between copper-copper electrodes in a solution containing 100 mM CuSO ₄ and 100 mM Na ₂ SO ₄ supporting electrolyte. Potential applied is -0.2 V vs Ag AgCl(sat). The drastic current jump around 670 seconds is due to the connection between anode and cathode	130
Figure 5.4	SEM image of the copper wire grown between two copper electrodes in a solution 100 mM CuSO ₄ and 100 mM Na ₂ SO ₄ supporting electrolyte. The dash line shows the original position of working electrode before electrode deposition	131
Figure 5.5	Chronoamperometric curve of Ag wire growth between copper-copper electrodes in a solution containing 5 mM AgNO ₃ and 100 mM NaNO ₃ . Potential applied is 0 V vs Ag AgCl(sat). Connection occurred after depositing for around 150 second	133
Figure 5.6	EDS of the wire deposited between copper-copper electrodes in a solution containing 5 mM AgNO ₃ and 100 mM NaNO ₃ . Potential applied is 0 V vs Ag AgCl(sat)	134
Figure 5.7	SEM image of the silver wire between two copper electrodes grown at open circuit in a solution containing 5 mM 100 mM NaNO ₃ and 100 mM H ₂ SO ₄	135

Figure 5.8	Chronoamperometric curve of copper wire growth between copper-copper electrodes in a solution containing 200 mM CdSO ₄ , 1 mM SeO ₂ and 50 mM HClO ₄ . Potential applied is -0.6 V vs Ag AgCl(sat)	137
Figure 5.9	EDS of the wire deposited between copper-copper electrodes in a solution containing containing 200 mM CdSO ₄ , 1 mM SeO ₂ and 50 mM HClO ₄ . Potential applied is -0.6 V vs Ag AgCl(sat)	138
Figure 5.10	Plot of resistance of CdSe wire as a function of the concentration of NaCl in a solution containing 10 mM NaNO ₃	140
Figure 5.11	Plot of resistance of CdSe wire as a function of the concentration of CdSO ₄ in a solution containing 10 mM NaNO ₃	141
Figure 5.12	Plot of resistance of CdSe wire as a function of the concentration of NaClO ₄ in a solution containing 10 mM NaNO ₃	142
Figure 5.13	Specific adsorption leads to changes in surface charge and electrical properties of the nanowires. (a) Electrochemical codeposition of p-type CdSe. (b) Adsorption of cations: positive ‘gating’ of p-type CdSe leads to depletion of hole carriers and higher resistance. (c) Adsorption of anions: conversely, negative ‘gating’ of p-type CdSe leads to lower resistance.	114

CHAPTER 1

INTRODUCTION

1.1 Nanomaterials in analytical chemistry

Nanomaterials is a subdiscipline in the sciences of chemistry and materials.^{1,2} Nanomaterials have numerous commercial and technological applications in many areas including analytical chemistry.³⁻⁶ The synthesis of new nanomaterials presents challenges for the development of analytical chemistry methods which can be used to characterize the nanoscale structure of these materials. In addition, the unique properties of nanomaterials also offer opportunities for the invention of new analytical chemistry methods that exploit these properties.

Analytical characterization techniques have recently been developed to boost the advancement of nanomaterials. These techniques include scanning probe techniques (e.g. AFM, STM) and “beam methods” which are based on the spatially confined interaction of ions, electrons or electromagnetic radiation with a sample.⁷⁻¹⁰ The scanning probe techniques are powerful visualization/imaging tools for understanding the complex surface of nanomaterials while beam methods provide detailed analytical information of samples. In Adams’ review,^{7,11} beam methods were discussed, which include secondary ion mass spectrometry (SIMS) with focused primary ion beams, laser microprobe mass spectrometry(LMMS), X-ray photoelectron spectroscopy (XPS), transmission/scanning

electron microscopy (TEM, SEM), Auger emission spectroscopy and scanning Auger microscopy (AES, SAM), ion beam analysis (IBA) belonging to the category of microbeam methods together with techniques such as proton-induced X-ray emission and Rutherford backscattering spectroscopy (A-PIXE, RBS) and microscopic X-ray fluorescence analysis (A-XRF). Techniques such as XPS, SIMS, and LMMS do not have good spatial resolutions but remain extremely powerful due to the functional molecular (structural) information that they can provide.

In this chapter, we are more interested in exploiting the unique properties of nanomaterials for analytical chemistry. Research on the application of nanomaterials in analytical chemistry grows rapidly in terms of the number of literature reports over the recent years. A significant part of this research has been directed toward the area of life and biomedical sciences. Many interesting analytical applications utilizing nanomaterials often incorporate biological components in the sensor transducer elements or separations phase or extraction materials.

In this manuscript, electrochemistry coupled with several other techniques was used to fabricate nanomaterials for the purpose of being applied in analytical chemistry. Here, the applications of nanomaterials will be introduced according to analytical application types.

1.1.1. Nanomaterials in optical sensors

Nanomaterial-based optical sensors are one of the most important types of chemical sensors which are capable of continuous, real-time monitoring of diverse analytes. The optical properties of nanoparticles in the polymeric aggregate depend on

interparticle distance. Genzel and Van Duyne et al.^{12,13} found that gold-nanoparticle aggregates appear red as the interparticle distance is larger than the average particle diameter, and blue as the interparticle distance is smaller than the average particle diameter. This unique property of nanoparticles could be applied in preparing a highly selective, colorimetric sensor.¹⁴⁻¹⁷ Reynolds et al.¹⁸ prepared nanoparticle-based colorimetric sensor functionalized with separate oligonucleotide sequences. The lower limit of detection (LOD) could go to 500 pM for a 24-base, single-stranded target and 2.5 nM for a double-stranded target oligonucleotide. This kind of nanoparticle-based optical sensor has also been used by Thanh et al.¹⁹ in the immunoassay of anti-protein A. The nanoparticle aggregates have a absorption change at 620 nm that was monitored by an absorption plated reader. The LOD was 1mg/L of anti-protein A.

Nanomaterial-based sensors have also been used for the detection of DNA sequences, DNA hybridization and DNA mismatches. For example, DNA–gold nanoparticle conjugates with an attached organic dye as the fluorophore were used to detect DNA hybridization.²⁰ The fluorescence signal from the dye was quenched by the gold nanoparticles and was restored as hybridization of the DNA–gold nanoparticle conjugated with a complementary DNA target. A similar application of gold nanoparticles for detection of single-stranded DNA using dye-tagged probe was reported.²¹ One other detection of DNA sequence based on DNA-nanoparticles conjugates use fluorescent semiconductor nanocrystals, such as CdSe/ZnS core/shell nanocrystals, instead of organic dyes.²² Compared to organic dyes, semiconductor nanocrystals have several advantages; e.g. negligible photobleaching, higher quantum

yield and precise emission bands in the visible range which are tunable by varying the nanocrystal size. The disadvantage is the high toxicity of CdSe to human health.

Besides being used in bio-detection, nanomaterials were applied in the optical detections of chemicals or humidity. Some gas-sensing semiconductors synthesized by sol-gel and sputtering methods could change their optical transmittance in NO gas.²³⁻²⁵ For example, the transmittance changes, caused by NO, of the CoO/SiO₂ nanocomposite films deposited on a quartz-glass substrate were measured in the wavelength range of 400-800 nm at 350°C by a spectrophotometer with a special quartz cell.²⁶ Metal oxides nano materials, such as Mn₃O₄, Co₃O₄ and NiO have reversible change in the visible-near-IR absorbance in the atmosphere of a reducing gas, such as CO or H₂.²⁷ It was pointed out in a mechanism that this optical change was caused by the change of electron or positive-hole density during a catalytic reaction of anionically adsorbed oxygen on the surface. It has been proved that deposition of gold on NiO could effectively improve the sensitivity of NiO film as a CO-gas sensor, since the Au/NiO film has enhanced catalytic activity.²⁸ The LOD of CO in air using Au/NiO thin film can be as low as 100 ppm.²⁹ Similar modified metal oxides have been used to make sensors for CO and H₂.^{29,30} Co₃O₄ and NiO were also reported to have sensitive absorbance changes to humidity at room temperature.^{29,31} The response times of both oxides films are within several minutes.

Nanomaterial-based chemical sensors have been prepared based on the changes of photoluminescence phenomena induced by the interaction between nanomaterials and analytes. The photoluminescence emission observed from porous silicon greatly depends on the chemical nature of the silicon surface. For example, Germanenko reported that WO₃ and W₂O₅ suspended in methanol solution could quench the photoluminescence of

nanoporous Si.^{32,33} This phenomenon of photoluminescence quenching has been used to prepare various chemical sensors.³⁴ Nanoparticles or modified nanoparticles that could be used as optical labels have been discussed previously in the part of DNA-detection.²⁰⁻²²

1.1.2. Nanomaterials in electrochemical sensors

Compared to optical sensors, electrochemical sensors may be less sensitive. However, electrochemical sensors offer elegant routes for interfacing, at the molecular level, biological recognition events and electronic signal-transduction processes.³⁵ In addition, electrochemical sensors coupled with nanotechnology may be developed into portable systems which are low cost, simple to use and rapid in response.

Enzyme detection with amperometric sensors face a big challenge since the redox center of the enzyme is normally electrically insulated by a protein shell and cannot be reduced or oxidized. Aligned carbon nanotubes prepared by self assembly can build a electrical communication between electrode and redox protein covalently attached to the ends of the single-wall nanotubes.^{36,37} In this way, direct electron-transfer between enzymes and electrode surfaces is possible. For enzyme electrodes which detect released NADH or hydrogen peroxide, the detection is often fouled by the large overvoltage in their oxidation. The carbon nanotube-modified electrodes could greatly enhanced redox activity of NADH and hydrogen peroxide.^{38,39} Platinum nanoparticles deposited on the carbon nanotubes could further improve the detection of the peroxide species.⁴⁰

DNA hybridization detection with electrical sensors has attracted considerable research efforts.^{41,42} Tamiya's group⁴³ reported the use of *Escherichia coli* single-stranded DNA binding protein as the probe for the electrochemical detection of DNA

hybridization. This protein probe attached to gold nanoparticles was used as the hybridization label. Changes in the Au oxidation signal was monitored to inform whether binding had occurred between the protein–gold nanoparticle probe and DNA target. Pang et al.⁴⁴ reported an amplified voltammetric detection of DNA hybridization through ferrocene-capped gold nanoparticles/streptavidin conjugates. The voltammetric signal could be amplified by a large number of ferrocenes attached to one gold nanoparticle and with close proximity to the underlying electrode. Colloidal gold nanoparticles self-assembled on gold electrode could enhance the DNA immobilization amount on a gold electrode and lower the detection limit of electrochemical DNA biosensor.⁴⁵ Single-stranded DNA probe was immobilized on the gold nanoparticles via a mercaptohexyl linker attached to the 5'-phosphate end of single-stranded DNA. The ssDNA-containing gold electrode was exposed to ferrocenecarboxaldehyde labeled complementary ssDNA in solution and the hybridization events were electrochemically determined via differential pulse voltammetry. A similar strategy was applied for generation of electrochemical response based on silver deposits, instead of redox-active ferrocenes.⁴⁶ Fang et al.⁴⁷ reported a new electrochemical DNA hybridization sensor. Tris(2,2-bipyridyl)cobalt(III) $[\text{Co}(\text{bpy})_3^{3+}]$ -doped silica nanoparticles were used as the oligonucleotide labeling tag and induced sensitive electrochemical signals at hybridization.

1.1.3. Nanomaterials in separations and extraction techniques

The applications of nanomaterials in separation science are mostly in miniaturized techniques including microchip electrophoresis and capillary electrophoresis.

Nanomaterials have been shown to be highly applicable and in several cases, demonstrating effective improvements over existing systems. Problems of aggregations and stability, as well as health and environmental safety issues, have been considered as main disadvantages in the applications of nanomaterials in separation.

Nanoparticles were used in microchip electrophoresis to improve separation of DNAs in these systems. Ultradilute polymer solutions have been used for the separation of long DNA in microchip electrophoresis. Resolution could not be improved further beyond a critical polymer concentration, when the DNAs become entangled with the polymer matrix. Chang et al.⁴⁸ demonstrated an application of gold nanoparticles in capillary electrophoresis for the rapid and highly efficient separation of long double strands of DNA. The gold nanoparticles were modified with poly(ethylene oxide) to avoid aggregation and to allow strong interactions with DNA molecules. The resolving power of separation rely on the interactions between DNA and poly(ethylene oxide) adsorbed on gold nanoparticles. Compared to polymer, polymer-modified gold nanoparticles have improved separation due to the much heavier density and thus the greater capability to slow the entangled DNA fragments. Polystyrene latex nanoparticles grafted with poly(ethylene glycol) polymer on the surface were also used to improve DNA separation.⁴⁹ Gold nanoparticles were reported to be applied to stationary phases in gas chromatography using monolayer protected nanoparticles.⁵⁰

Barron's group^{51,52} developed sparsely cross-linked "nanogels", as novel DNA sequencing matrices for capillary electrophoresis. The nanogels, which retain fluidity of solution for ease of filling and removal from the capillary, improve the selectivity for large DNAs. This mechanism is similar to selectivity mechanism in slab-gel

electrophoresis and reduced sample peak widths. Wang et al.⁵³ reported gold nanoparticles coated on capillary wall of a chip-based capillary electrophoresis technique. Citrate stabilized gold nanoparticles were adsorbed onto the cationic polymer, poly-(diallyldimethylammonium chloride) coated on capillary wall. The resolutions and plate numbers of solutes were doubled.

In extraction applications, a novel method based on the application of cationic polystyrene nanoparticles has been developed for solid-phase extraction of phosphorothioate oligonucleotides from human plasma.⁵⁴ The hydrophobic and multiple electrostatic interactions between the oligonucleotides and the nanoparticles, which could be controlled by pH, mediated the high binding affinity that is required for an effective isolation out of complex mixtures. Zhang et al.⁵⁵ reported another application of nanomaterials in extraction. Here, multiwalled carbon nanotubes were used as a solid-phase extraction sorbent for chlorobenzenes. Results showed that multiwalled carbon nanotubes had high adsorption capacity and high extraction recoveries for chlorobenzenes.

Nanomaterials have many other applications not discussed here. It is believed that nanomaterials will play a more important role in analytical chemistry.

1.2 Nanosphere Lithography

Nanosphere lithography is a simple inexpensive method for nanofabrication. The concept of “nanosphere lithography” (NSL) came after “Natural lithography” which was given by Deckman and Dunsmuir in 1981.^{56,57} Natural lithography was referred to as a microfabrication technique which textures large surface areas with either a random or

mosaic array of identical microstructures from a lithographic template of spherical colloidal particles (polystyrene latexes). The initial stimulus of this work was to fabricate random and periodic roughness on a nano scale that can be use to produce a variety of optical elements such as gratings, interferometers, and antireflection coatings.⁵⁶ Deckman and Dunsmuir achieved several surface profiles by etching the polymer spheres on the mask with a oxygen ion beam. The resulting microstructures could be used to produce a variety of optical effects and devices, such as improved optical absorption of solar cell and surface enhanced Raman effects.

In 1995, driven by developing nanofabrication techniques that combine the outstanding resolution of electro-beam lithography and the large throughput of X-ray lithography, Hulteen and Van Duyne sought help from Deckman's "natural lithography" which was substituted by an operationally more descriptive term—"Nanosphere lithography".⁵⁸ Compared to natural lithography, which has only one layer of nanospheres, NSL was extended by Van Duyne et al. to double layers. In this manuscript, multilayers of nanosphere will also be included in this technique.

1.2.1 Fabrications

There are four techniques used for fabricating large areas of NSL templates. These methods are (1) spin coating; (2) convective self-assembly ; (3) assembly by slow evaporation; and (4) tilting technique.⁵⁷⁻⁶⁷ Spin coating is the most often used method to produce NSL templates of a single layer. Convective self-assembly is a rather new technique in producing single layer NSL.⁶⁷ Assembly by slow evaporation produces NSL templates of multilayers with fewer defects. The disadvantage of this technique is that it

takes several days to prepare a sample. Tilting technique has been studied only by Ng et al.⁶⁵ The NSL template prepared by this technique is heterogeneous with one end monolayer and the other end multilayers.

1.2.2 Applications

1.2.2.1 NSL as surfaces

NSL template itself is an interesting material for study. Goldenberg et al. has studied the diffraction properties of monolayer or multilayers of 0.2 – 6.0 μm spheres assembled with different techniques.⁶⁸ Deckman et al. modified the nanospheres on the substrate surface into different shapes and studied the optical properties of the textured surface and their potential for being used in optical devices.⁵⁷ Zhou et al.⁶⁹ reported on the use of NSL to construct two-dimensional arrays of polystyrene particles coated with multilayered polyelectrolyte shells and truncated eggshell structures composed of polyelectrolyte thin layers. The truncated eggshell structure could be vessels for the extraction and storage of charged aniline monomer from solution. The aniline monomers stored in the polyelectrolyte shells could be electropolymerized to polyaniline inside the structure.

1.2.2.2 NSL as lithographic masks

One other application of NSL is to use the nanosphere layers as a mask for depositing desired species, usually a metal or a semiconductor, through the mask by physical or chemical deposition. In Van Duyne's⁵⁸ paper published in 1995, two periodic particle array surfaces were deposited in a modified vapor deposition system—

“consolidated vacuum corporation” through single-layer or double-layer NSL masks. The substrates for NSL included insulators (e.g. Mica or glass), semiconductors (e.g. Si single crystals), and metals (e.g. Au(poly) or Cu(100)). Thereafter, more surface features were constructed by similar processes or with further modifications and the resulted particle arrays have attracted intensive interests. TiO₂ nanoparticle arrays, which were expected to have prominent chemical and photochemical reactivity in many areas such as solar energy conversion and catalysis, were prepared by Garrett et al.⁷⁰

Nanoparticles of metal and semiconductors exhibit size-dependent properties that are different from the corresponding bulk materials. These properties include optical, magnetic, catalytic, thermodynamic, electrochemical and electrical transport.⁶⁰ To understand the size-dependent properties and to exploit the potential of creating new functional materials and advanced devices using the nanoparticles, it is important to fabricate size-tunable nanoparticles. Van Duyne et al. controlled the size of the particles physically deposited through the NSL templates.⁶⁰ The in-plane diameter could be as small as 21nm. The smallest silver particle prepared with this technique contains around 40,000 atoms. One other method provided by Van Duyne et al.⁷¹ is electrochemical tuning of electrochemical reactive species of the nanoparticles. Thermal annealing has also been used for tuning the size of the particles on the substrates. Li and coworkers have studied the hexagonal-patterned Ge nanoparticles on Si substrates through NSL templates.⁷² With annealing at 650° C, the Ge nanoparticles, originally in triangular shape, transform into spherical dots. This process could modulate the size of the after-annealing Ge nanoparticles by controlling the thickness of the initial Ge deposition.

NSL-fabricated silver nanoparticles have been extensively studied by surface plasmon resonance spectrum (SPR) and localized SPR (LSPR).^{59,61-63,73-77} Schmidt et al. examined the effect of the NSL-fabricated silver nanoparticle substrates on the surface-enhanced Raman spectrum (SERS) of rhodamin 6G and found that silver nanoparticles prepared by NSL illustrated an order-of-magnitude enhancement relative to amorphous silver films.⁷⁸

Other surface features have been fabricated besides the triangular and hexagonal-shaped particles made through single-layer and double-layer NSL templates. Bonegerg et al. found hillocks and rings arrays on the substrate surfaces after thermal deposition on the NSL single-layer.⁷⁹ Haynes and Van Duyne fabricated the extended nanostructures using the so-called angle-resolved nanosphere lithography.^{80,81} The nanostructure included nano-overlaps, nanocontacts, nanogaps and nanochains. The optical characteristics of these nanostructures made of noble metals were studied. Polarized microextinction spectroscopy illustrated that dichroic contrast varied between 20 and 200 nm upon comparing the optical spectra of the transverse and longitudinal LSPR modes. Results show that the nanostructures hold significant potential as chemical and biological nanosensor and dichroic filters. A similar method was used in Giersig's papers and the experimental results were in good agreement.^{82,83}

The NSL-fabricated nanoparticles could be used to produce vertically aligned nanowires. Fan et al. fabricated well-ordered ZnO nanowire arrays in a large scale on epitaxial GaN substrates by using NSL and mask transfer technique as well as optimized vapor-liquid-solid growth.⁸⁴ Vertically aligned carbon nanowires were grown by plasma-enhanced chemical-vapor deposition methods on the 9-nm-thick Ni catalyst particles,

which were deposited via evaporation or sputtering through the NSL template.⁸⁵ Schubert et al. grew silicon nanowires by molecular beam epitaxy using the gold nanoparticles previously deposited on the silicon(111) surface with NSL.⁸⁶

1.2.2.3 Fabrications with Reactive Ion Etching Variant of Nanosphere

Lithography

Reactive ion etching (RIE) technique makes NSL more powerful. Ordered arrays of in-plane, triangular cross-section nanopores were made with NSL combined with reactive ion etching by Van Duyne et al.⁸⁷ The in-plane widths and the depths of the nanopores were adjustable with angle-resolved NSL. A novel film using nanosphere lithography was fabricated by adding a thin silver layer on the surface containing the nanopores. This film exhibited remarkably narrow plasmon band in reflectance spectra and greater sensitivity to external dielectric environment than observed in other nanoparticle systems.⁸⁸ Tan et al. took advantage of the nanopores by depositing gold into the nanopores followed by thermal annealing to obtain nanoparticles.⁸⁹

Size-tunable arrays of nanoholes have been produced by reducing the diameter of spheres on NSL templates with RIE, and subsequently evaporating MgF_2 on to the template. An array of holes appeared after the removal of the spheres. The holes could be filled with desired species with electrodeposition.^{90,91} Analysis using high-field torque magnetometry and three-dimensional micromagnetic modeling demonstrated a change in anisotropy as the diameter of Co particles that filled in the hole array was reduced.⁹²

Cheung et al. demonstrated that the combination of the NSL and the RIE could be a alternative to conventional top-down fabrication technique.⁹³ An array of silicon

nanowires was fabricated from NSL on silicon substrate by two RIE steps. The first RIE step tailored the size of the nanospheres and second step the exposed silicon area by deep RIE using the 'Bosch' process.

Combined with RIE, NSL has also been used to fabricate nanoimprinting molds, which could be transferred on to a polymer film or poly (methyl methacrylate)-coated silicon substrate. It has been shown that this technique is a promising way to fabricate 2D photonic crystals.⁹⁴

1.2.2.4 Fabrication of Macroporous Materials

NSL templates have been widely used to synthesize highly ordered 3-D macroporous materials, which include, but not limited to, ceramics^{95,96}, metals^{97,98} and polymers.⁹⁹⁻¹⁰¹ These macroporous materials attracted much interest because of their special optical and photonic band gap properties. The extension of NSL templates to magnetic materials is of particular interest.^{64,102} The techniques of depositing materials in to the NSL templates are various. Electrochemical deposition, which was first described by Braun and Wiltzius, is of significant advantage compared with other techniques.¹⁰³ The advantages in using the electrochemical deposition through NSL templates to produce three-dimensional ordered macroporous metal films were discussed by Bartlett et al.^{64,66}

1.2.2.5 Other applications

Smooth, well-ordered nanostructure surfaces could produce superhydrophobic surfaces if the ratio of the liquid-solid contact area to the overall projected area remains

small. NSL technique combined with oxygen plasma treatment was successfully used in fabricating well-ordered, tunable superhydrophobic surface whose water contact angle could be tuned from 132° to 170°. ¹⁰⁴ The dynamic water contact angle measurement confirmed that well-ordered 2-D nanostructured systems have relatively large water contact angle hysteresis.

By incorporating NSL and surface silane chemistry using vapor and solution deposition processes, hexagonally patterned lysozyme nanoarrays have been assembled on the surface of silicon wafers. This approach offered a fast, reliable and economical method to fabricate protein arrays over large areas with feature sizes comparable to scanning-probe based techniques. ¹⁰⁵ The size of the island prepared was around 120 nm for solution-prepared template and 60nm for the vapor-prepared template. The size and density of the protein islands could be tunable by using nanospheres of different sizes. Antibody tests showed that the patterned lysozyme maintains its bioactivity on the surface.

1.3 Self-Assembled Monolayers (SAMs)

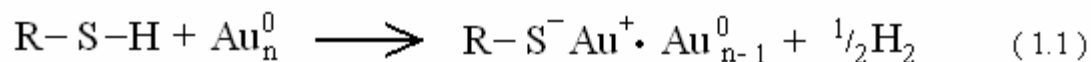
Self-assembled monolayers (SAMs) can be prepared using different types of molecules and different substrates. Well known examples are alkylsiloxane monolayers, fatty acids on oxide materials and alkanethiolate monolayers. SAMs can be assembled from gas phase or solutions. In this section, we will concentrate exclusively on SAMs of functionalized alkanethiols on gold surfaces from solution. Gold is used because gold is a reasonably inert metal -- it does not have a stable oxide under ambient conditions. The thiol molecules adsorb readily from solution onto the gold, creating a dense monolayer

with the tail group pointing outwards from the surface. By using thiol molecules with different tail groups, the resulting chemical surface functionality can be varied within wide limits. Alternatively, it is also possible to chemically functionalize the tail groups by performing reactions after assembly of the SAMs.

1.3.1 Formation of SAMs

SAMs on gold surface can be prepared simply by immersing a clean gold substrate into a dilute (~1-10 mM) ethanolic solution of the desired thiols and washing off the excess.¹⁰⁶ The growth of thiols on to the gold surface is very fast at the first few seconds and slows down. Dense coverage (80-90%) of thiol molecules could be obtained quickly from millimolar solutions (in milliseconds to minutes). The follow up process requires several hours to several days to maximize the density of molecules and minimize the surface defects in the SAMs. The process of assembly and the structure of SAMs are affected by several experimental factors, such as solvent, temperature, concentration of adsorbate, immersion time, purity of the adsorbate, cleanness of the gold surface, and the structure of the thiol molecules.¹⁰⁷

The mechanism of assembly from solution has not been fully understood yet. But, it is well known that both the thiol head group and organic chain play important roles in the process leading to the formation of SAMs. The thiol head groups chemically adsorb onto the gold surface via the formation of a gold-thiol bond.^{108,109} This interaction (~44 kcal/mol) is very strong and makes the resulting monolayers quite stable.¹¹⁰ The noncovalent lateral interactions (the enthalpy of lateral interaction per CH₂ group is ~1.5 kcal/mol) among the organic chains help the molecules to form high ordered monolayers.



1.3.2 Characterization of SAMs

SAMs have been thoroughly characterized using a large number of surface analytical tools. Among the most frequently used techniques are infrared spectroscopy, ellipsometry, studies of wetting by different liquids,^{106,111-113} x-ray photoelectron spectroscopy,¹⁰⁶ electrochemistry,^{111,114} and scanning probe measurements.¹¹⁵⁻¹¹⁷

It has been clearly shown that SAMs with an alkane chain length of 12 or more methylene units form well-ordered and dense monolayers on Au(111) surfaces. The alkyl chains of the thiols are in the all trans-conformation, tilted at an angle of ~20 - 30° from normal to the metal surface. The lattice of the high-coverage thiol phases on Au(111) is generally accepted as ($\sqrt{3} \times \sqrt{3}$)R30° adlayer.^{110,118-120} Some domains show a superlattice of this structure in which individual chains either protrude or recede by 0.07 nm. These molecules define a rectangular unit mesh having dimensions of 0.85 and 1.0 nm, which is corresponding a c(4 x 2) superlattice.¹²¹⁻¹²³ At room temperature, the amount of the c(4 x 2) superlattice for long chain (n > 11) alkanethiolate SAMs on Au(111) is small compared to the ($\sqrt{3} \times \sqrt{3}$)R30° lattice, while the c(4 x 2) superlattice becomes predominant for medium-length (n = 6) alkanethiolate SAMs.¹⁰⁷

Extension of immersion time cannot eliminate defects in SAMs. Defects of alkanethiolate SAMs are various: straight or zigzag missing rows,¹²⁴ vacancies due to the roughness of the gold surface, molecule defects due to the molecule absence (pinhole) or molecule disorder, and domain boundaries.¹²¹ The amount of defects of SAMs depends

on the adsorption time, hydrocarbon chain length, terminal groups, temperature and substrate quality. Generally, defects decreases with increasing hydrocarbon chain length. Introduction of hydrophilic groups (-S, -COOH, -OH, -NH₂) as terminal groups or benzene rings in the hydrocarbon chains usually results in larger amount of defects.¹²⁵ Efforts have been made to reduce defects in SAMs.¹²⁶⁻¹³⁰ No procedure could produce defect-less monolayer.

Although the gold-thiol bond is very strong, the adsorbed alkanethiols still have the ability to move along the gold surface. This conclusion is supported by two observations. First, exchange occurs at the grain boundaries on the gold surface when a SAM grown on the gold surface is placed in a different alkanethiol solution.¹²⁰ Second, the alkanethiols in SAMs have been shown to surface diffuse to heal gaps of exposed gold.¹³¹

The stability of the SAM is very important. SAMs are stable in the potential window of between approximately +0.8 and -1.4 V versus SCE.^{132,133} This range satisfies most electrochemical applications. Beyond this range, the thiol molecules might be oxidatively or reductively desorbed.^{134,135} The exact potentials at which SAMs desorb are affected by the structure of thiol molecule. Generally, thiols with longer chains form SAMs with wider potential window in which SAMs are stable. A similar trend has been observed for the thermal stability of SAMs. The greater the forces of interaction between chains the greater the thermal stability. Aliphatic alkanethiols have been reported to desorb from gold at temperatures of 75°C for butanethiol¹³⁶ and above 100°C for dodecanethiol.¹³⁷ SAMs with hydrogen bonding¹³⁸ or π - π bonding¹³⁹ exhibit better thermal stability than aliphatic hydrocarbons.

1.3.3 Mixed SAMs

Mixed SAMs are the monolayers that comprise a well-defined mixture of molecular structures. The methods for synthesizing mixed SAMs include: (1) coadsorption from solutions containing thiol mixture ($\text{RSH} + \text{R}'\text{SH}$) (or substitution some thiol molecules on SAMs with second thiol), (2) adsorption of asymmetric disulfides (RSSR'), and (3) adsorption of asymmetric dialkylsulfides (RSR'). The first method is more versatile and most used for synthesizing mixed SAMs. It allows the formation of SAMs with widely varying compositions.¹⁴⁰ It is very hard for the approaches of adsorption of asymmetric disulfides or asymmetric dialkylsulfides to obtain mixed SAMs with mole fraction much different from 0.5. It is noteworthy to point out that the mole fraction of the specific thiol molecules in the SAM are not the same as the mole fraction of the thiol in solution.

Mixed SAMs provide desirable flexibility in design and synthesis of functional SAMs that span a wider range of chemical and physical properties than do pure SAMs.^{141,142} Mixed SAMs make it possible to continuously tune the interfacial properties of a SAM simply by varying the ratio of compositions of the thiols in the mixed SAMs.

1.3.4 Applications of SAMs in nanoscience and nanotechnology

The applications of SAMs in nanoscience and nanotechnology are diverse. For example, SAMs are used to stabilize or add function to nanostructures. SAMs are also used to link molecular-level structures to obtain desired macroscopic interfacial properties. Two major applications of SAMs in the area of nanomaterial are using SAMs to tailor the surfaces of pre-formed nanostructures and patterning SAMs to

nanostructures by various techniques. There are three common strategies for tailoring the composition of the SAM on nanoparticles and the functional groups exposed at the SAM-solvent interface. They are: (1) forming the nanoparticles directly in the presence of ω -functionalized thiols,^{143,144} (2) exchanging an existing ligand for an ω -functionalized thiol,^{145,146} and, (3) modifying the original thiol covalently by an interfacial reaction.¹⁴⁷ The techniques for patterning SAMs include microcontact printing,¹⁴⁸ photolithography or particle beam lithography,¹⁴⁹⁻¹⁵¹ and other methods such as ink-jet printing and topographically directed assembly.^{152,153}

1.4 Polyaniline (PANI)

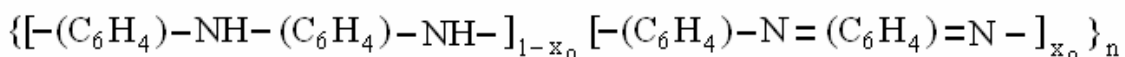
Polyaniline is a stable conducting polymer. Since the start of intensive research in conducting polymer in 1977, a variety of polymers with extended π -systems have been shown to display high electrical conductivities.¹⁵⁴ Polyaniline (PANI) was one of the earliest conjugated polymers with semiconductivity.¹⁵⁵ PANI is now known as a novel material in the field of conducting polymer. The technological potential of PANI relies in its outstanding stability and processibility.

Polyaniline was first known in 1835 as “aniline black” and in 1840 analysis of this product from the chemical oxidation of aniline in an acidic solution was carried out by Fritzsche.¹⁵⁶ In 1862, the electrochemical oxidation of aniline sulfate in aqueous solution formed an insoluble blue pigment.¹⁵⁷ Thereafter, similar phenomena were observed during the oxidation of aqueous hydrochloric acid solution of aniline.¹⁵⁸ The structure of PANI was then studied and different structures of PANI were proposed. A complex structure which does not fit present day understanding was proposed by

Bucherer.¹⁵⁹ A linear octameric structure was then proposed by Green et al.¹⁶⁰ Leucoemeraldine, the base of the octamer, has four oxidation states: protoemeraldine, emeraldine, nigraniline and pernigraniline.

1.4.1 Structure of PANI

Polyaniline can be categorized as a general class of conducting polymers composed of benzoid and quinoid character connected by nitrogen. PANI is built from two principle units: (1) the reduced form containing two benzoid rings and, (2) the oxidized form containing one benzoid ring and one quinonoid ring. Different structures could be obtained by changing the relative ratio of the two units.¹⁶¹



The x_0 values of the five compositions named by Green and co-workers are listed in the Table 1.1. MacDiarmid speculated that more compositions might exist.¹⁶² The PANI structure contains the repeating units up to 1000 and its conductivity varies from 10^{-11} to 10 S/cm. Of all the structures, only the emeraldine salt is electrically conductive. Deprotonation of the conductive emeraldine salt in an aqueous alkali affords the insulating emeraldine base. Reduction of emeraldine gives rise to a nearly colorless insulator, leucoemeraldine, whereas oxidation of emeraldine produces another insulator, pernigraniline.

1.4.2 Polymerization of aniline

1.4.2.1 Chemical polymerization

Polyaniline can be obtained by chemical synthesis and electrochemical synthesis. The systems for synthesis of PANI are various. In a classic system, PANI is precipitate from an aqueous solution contain aniline, ammonium peroxydisulphate and acids such as hydrochloric sulphuric, nitric or perchloric acids. Here the aniline monomer is directly converted to a conjugated polymer through condensation. This PANI is normally intractable.¹⁶³⁻¹⁶⁵ PANIs were also prepared from systems containing tetrafluoroborates such as NaBF_4 , NO_2BF_4 and Et_4NBF_4 . The PANIs prepared in this way were found to

Table 1.1. Fractional content of imine vs nomenclature of polyanilines.

x_0	Nomenclature
0	leuco-emeraldine
0.25	protoemeraldine
0.50	emeraldine
0.75	nigraniline
1.0	pernigranilin

have increased conductivity.¹⁶⁶ Four major parameters affecting the course of the reaction and the properties of PANIs synthesized were discussed by Syed and Dinesan: nature of the medium, concentration of the oxidant, duration of the reaction and temperature of the medium.¹⁵⁶ Some synthesis systems have been designed for controlling the molecular weight of PANIs.¹⁶⁷

It is usually hard or impossible to obtain PANI from substituted aniline monomers, because the *para*-position must be kept free for radical coupling and the *ortho*- and *meta*- substituted derivatives have steric hindrances and weak inductance effects.¹⁵⁶

1.4.2.2 Electropolymerization

Electropolymerization has some advantages: (1) electropolymerization is a route with a fine control of the initiation and termination steps, (2) polymerization can be controlled at desired positions on the electrode, (3) electropolymerization is much cleaner and completely pollution-free compared to the chemical polymerization.

PANI is usually prepared from the acidic medium. The electrochemical techniques employed for synthesizing PANI generally includes: chronoamperometry, chronopotentiometry and cyclic voltammetry. Cyclic voltammetry is able to produce a PANI film which adheres strongly to the electrode surface, while chronoamperometry produce a powder which adheres loosely to the electrode.¹⁶⁸

Electropolymerization mechanisms of aniline. Different mechanisms for electropolymerization of aniline were proposed.¹⁶⁹⁻¹⁷³ All mechanisms agree that the first step is the oxidation of aniline into the radical cation. The mechanism proposed by Genies and co-workers for electropolymerization of aniline in acidic environment is shown in Figure 1.1.

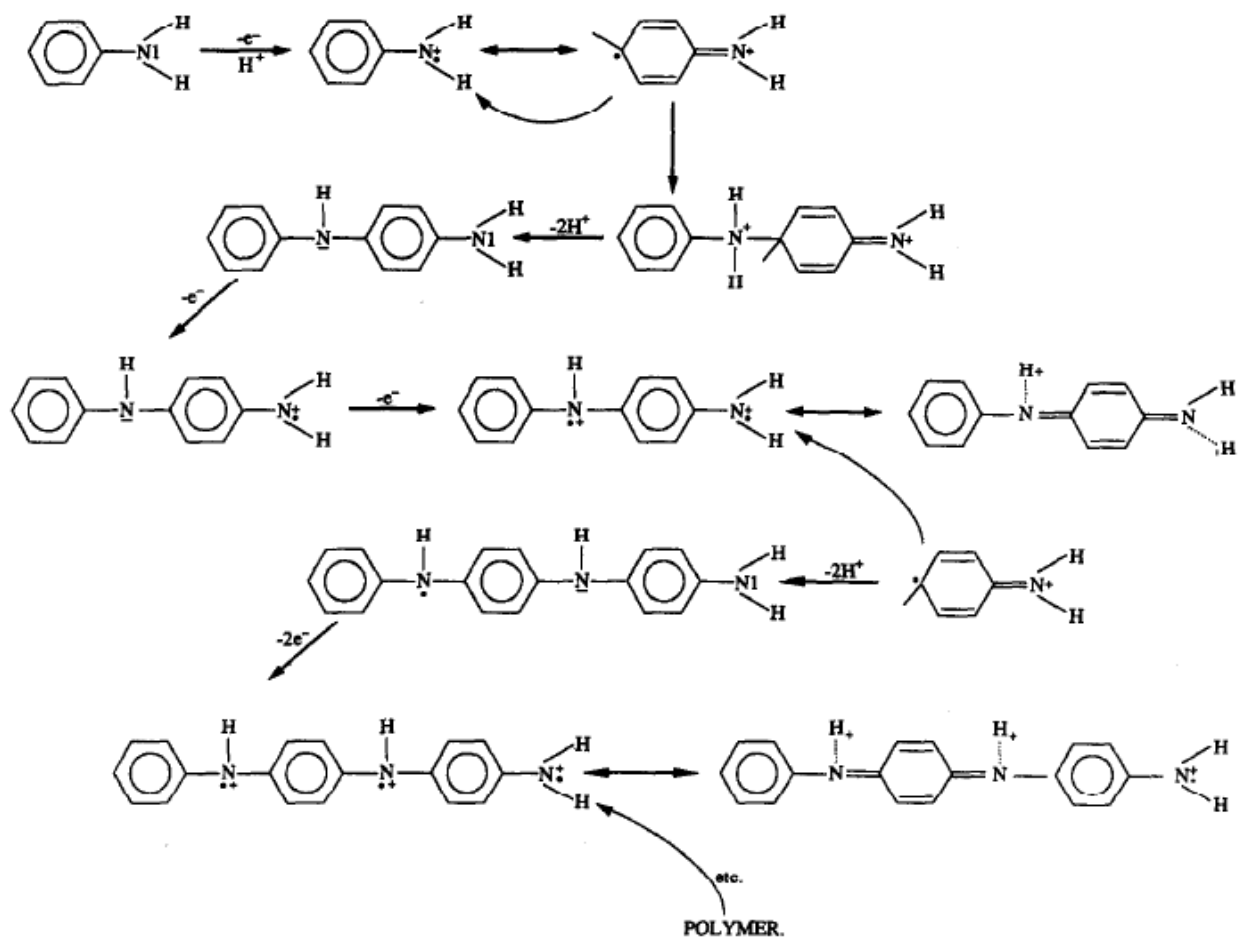


Figure 1.1. Mechanism of formation of conducting polyaniline.¹⁷³

1.5 References

1. Ozin, G. A. *Adv. Mater.* **1992**, *4*, 612.
2. Zhang, Y.; Ling, F.; Zhu, Q.; Xiao, Z.; Zhao, Z.; Zhang, Y.; Zheng, Y. *Nanoscience* **2006**, *11*, 137.
3. He, L.; Toh, C.-S. *Anal. Chim. Acta* **2006**, *556*, 1.
4. Kane, R. S.; Stroock, A. D. *Biotech. Prog.* **2007**, *23*, 316.
5. Na, N.; Zhang, S.; Wang, S.; Zhang, X. *J. Am. Chem. Soc.* **2006**, *128*, 14420.
6. Zhao, X.; Zhang, S. *Adv. Polymer. Sci.* **2006**, *203*, 145.
7. Heiderhoff, R.; Balk, L. J. *Inst. Phys. Conf. Ser.* **1997**, *160*, 1.
8. Hofmann, S. *Surf. Interface Anal.* **2000**, *30*, 228.
9. Leemput, V. d.; C., L. E.; Kempen, V.; H. *Reports on Progress in Physics* **1992**, *55*, 1165.
10. Rugar, D.; Hansma, P. *Physics Today* **1990**, *43*, 23.
11. Adams, F.; Vaeck, L. V.; Barrett, R. *Spectrochim. Acta, Part B* **2005**, *60*, 13.
12. Kreibig, U.; Genzel, L. *Surf. Sci.* **1985**, *156*, 678.
13. Yang, W.-H.; Schatz, G. C.; Duyne, R. P. V. *J. Chem. Phys.* **1995**, *103*, 869.
14. Elghanian, R.; Storhoff, J. J.; Mucic, R. C.; Letsinger, R. L.; Mirkin, C. A. *Science* **1997**, *277*, 1078.
15. Storhoff, J. J.; Elghanian, R.; Mucic, R. C.; Mirkin, C. A.; Letsinger, R. L. *J. Am. Chem. Soc.* **1998**, *120*, 1959.
16. Reynolds, R. A.; Mirkin, C. A.; Letsinger, R. L. *J. Am. Chem. Soc.* **2000**, *122*, 3795.
17. Storhoff, J. J.; Mucic, R. C.; Mirkin, C. A.; Letsinger, R. L.; Schatz, G. C. *J. Am. Chem. Soc.* **2000**, *122*, 4640.
18. Reynolds, R. A.; Mirkin, C. A.; Letsinger, R. L. *Pure Appl. Chem.* **2000**, *72*, 229.
19. Thanh, N. T. K.; Rosenzweig, Z. *Anal. Chem.* **2002**, *74*, 1624.

20. Glynou, K.; Ioannou, P. C.; Christopoulos, T. K.; Syriopoulou, V. *Anal. Chem.* **2003**, *75*, 4155.
21. Li, H.; Rothberg, L. J. *Anal. Chem.* **2004**, *76*, 5414.
22. Gerion, D.; Chen, F.; Kannan, B.; Fu, A.; Parak, W. J.; Chen, D. J.; Majumdar, A.; Alivisatos, A. P. *Anal. Chem.* **2003**, *75*, 4766.
23. Koshizaki, N.; Yasumoto, K.; Terauchi, S. *J. Appl. Phys.* **1995**, *34(Suppl.)*, 119.
24. Yasumoto, K.; Koshizaki, N. *Denki Kagaku oyobi Kogyo Butsuri Kagaku* **1996**, *64*, 1314.
25. Yasumoto, K.; Koshizaki, N. *J. Mater. Sci. Lett.* **1997**, *16*, 215.
26. Koshizaki, N.; Yasumoto, K. *Sens. Actuators B* **2000**, *66*, 122.
27. Kobayashi, T.; Ando, M.; Haruta, M. *Chemical Sensors* **1993**, *9*, 143.
28. Kobayashi, T.; Haruta, M.; Ando, M. *Sens. Actuators B* **1993**, *13*, 545.
29. Ando, M.; Kobayashi, T.; Haruta, M. *Sens. Actuators B* **1995**, *25*, 851.
30. Ando, M.; Kobayashi, T.; Iijima, S.; Haruta, M. *J. Mater. Chem.* **1997**, *7*, 1779.
31. Ando, M.; Kobayashi, T.; Haruta, M. *Solid State Ionics* **1999**, *121*, 307.
32. Germanenko, I. N.; Li, S.; Silver, S. J.; El-Shall, M. S. *Nanostruct. Mater.* **1999**, *12*, 731.
33. Li, S.; Germanenko, I. N.; El-Shall, M. S. *J. Phys. Chem. B* **1998**, *102*, 7319.
34. Shi, J.; Zhu, Y.; Zhang, X.; Baeyens, W. R. G.; Garcia-Campana, A. M. *Trend. Anal. Chem.* **2004**, *23*, 351.
35. Wang, J. *Analyst* **2005**, *130*, 421.
36. Gooding, J. J.; Wibowo, R.; Liu, J. Q.; Yang, W.; Losic, D.; Orbons, S.; Mearns, F. J.; Sharppter, J. G.; Hibbert, D. B. *J. Am. Chem. Soc.* **2003**, *125*, 9006.
37. Yu, X.; Chattopadhyay, D.; Galeska, I.; Papadimitrakopoulos; Rusling, J. F. *Electrochem. Commun.* **2003**, *5*, 408.
38. Wang, J.; Musameh, M.; Lin, Y. *J. Am. Chem. Soc.* **2003**, *125*, 2408.
39. Musameh, M.; Wang, J.; Merkoci, A.; Lin, Y. *Electrochem. Commun.* **2002**, *4*, 743.

40. Hrapovic, S.; Liu, Y.; Male, K. B.; Luong, J. H. T. *Anal. Chem.* **2004**, *76*, 1083.
41. Palecek, E.; Fojta, M. *Anal. Chem.* **2000**, *73*, 75A.
42. Gooding, J. J. *Electroanalysis* **2002**, *14*, 1149.
43. Kerman, K.; Morita, Y.; Takamura, Y.; Ozsoz, M.; Tamiya, E. *Anal. Chim. Acta* **2004**, *510*, 169.
44. Wang, J.; Li, J.; Baca, A. J.; Hu, J.; Zhou, F.; Yan, W.; Pang, D.-W. *Anal. Chem.* **2003**, *75*, 3941.
45. Cai, H.; Xu, C.; He, P.; Fang, Y. *J. Electroanal. Chem.* **2001**, *510*, 78.
46. Cai, H.; Wang, Y.; He, P.; Fang, Y. *Anal. Chim. Acta* **2002**, *469*, 165.
47. Zhu, N.; Cai, H.; He, P.; Fang, Y. *Anal. Chim. Acta* **2003**, *481*, 181.
48. Huang; Ming-Feng; Kuo; Yi-Chun; Huang; Chih-Ching; Chang; Huan-Tsung *Anal. Chem.* **2004**, *76*, 192.
49. Tabuchi, M. *Lab on a Chip* **2005**, *5*, 199.
50. Gross, G. M.; Grate, J. W.; Synovec, R. E. *J. of Chromatography, A* **2004**, *1060*, 225.
51. Doherty, E. A. S.; Kan, C. W.; Barron, A. E. *Electrophoresis* **2003**, *24*, 4170.
52. Doherty, E. A. S. *Anal. Chem.* **2004**, *76*, 5249.
53. Pumera, M.; Wang, J.; Grushka, E.; Polsky, R. *Anal. Chem.* **2001**, *73*, 5625.
54. Maier, M.; Fritz, H.; Gerster, M.; Schewitz, J.; Bayer, E. *Anal. Chem.* **1998**, *70*, 2197.
55. Liu, G.; Wang, J.; Zhu, Y.; Zhang, X. *Analytical Letters* **2004**, *37*, 3085.
56. Deckman, H. W.; Dunsmuir, J. H. *Appl. Phys. Lett.* **1982**, *41*, 377.
57. Deckman, H. W.; Dunsmuir, J. H. *J. Vac. Sci. Technol., B* **1983**, *1*, 1109.
58. Halteen, J. C. V. D., Richard P. J. *Vac. Sci. Tech., A* **1995**, *13*, 1553.
59. Jensen, T. R. *J. Phys. Chem. B* **1999**, *103*, 9846.
60. Hulteen, J. C.; Treichel, D. A.; Smith, M. T.; Duval, M. L.; Jensen, T. R. Van Duyne, R. P. *J. Phys. Chem. B* **1999**, *103*, 3854.

61. Traci R.; Schatz, G. C. V. D., Richard P *J. Phys. Chem. B* **1999**, *103*, 2394.
62. Jensen, T. R.; Malinsky, M. D.; Haynes, C. L.; Duyne, R. P. V. *J. Phys. Chem. B* **2000**, *104*, 10549.
63. Malinsky, M. D.; Kelly, K. L.; Schatz, G. C.; Duyne, R. P. V. *J. Phys. Chem. B* **2001**, *105*, 2343.
64. Bartlett, P. N.; Ghanem, M. A.; Hallag, I. S. E.; Grootb, P. d.; Zhukov, A. *J. Mater. Chem.* **2003**, *13*, 2596.
65. Ng, V.; Lee, Y. V.; Chen, B. T.; Adeyeye, A. O. *Nanotechnology* **2002**, *13*, 554.
66. Abdelsalam, M. E.; Bartleet, P. N.; Baumberg, J. J.; Coyle, S. *Adv. Mater.* **2004**, *16*, 90.
67. Ormonde, A. D.; Hicks, E. C. M.; Castillo, J.; Duyne, R. P. V. *Langmuir* **2004**, *20*, 6927.
68. Goldeberg, L. M. *Material Science and Engineering C* **2002**, *22*, 233.
69. Briseno, A. L.; Zhou, F. *Langmuir* **2004**, *20*, 219.
70. Bullen, H. A.; Garrett, S. J. *Nano Letters* **2002**, *2*, 739.
71. Zhang, X.; Hicks, E. M.; Zhao, J.; Schatz, G. C.; Duyne, R. P. V. *Nano Letters* **2005**, *5*, 1503.
72. Li, N.; Zinke-Allmang, M. *Japanese Journal of Applied Physics, Part 1: Regular Papers, Short Notes & Review Papers* **2002**, *41*, 4626.
73. Haes, A. J.; Duyne, R. P. V. *J. Phys. Chem. B* **2003**, *107*, 1772.
74. P, Y. C. R. J. E. Z. S. S. G. C. M. M. V. D. R. *J. Am. Chem. Soc.* **2004**, *126*, 12669.
75. Haes, A. J.; Schatz, G. C.; Duyne, R. P. V. *J. Phys. Chem. B* **2004**, *108*, 6961
76. Litorja, M.; Duyne, R. P. V. *J. Phys. Chem. B* **2001**, *105*, 6907
77. Malinsky, M. D.; Duyne, R. P. V. *J. Am. Chem. Soc.* **2000**, *123*, 1471
78. Schmidt, J. P.; Cross, S. E.; Buratto, S. K. *J. chem. phys.* **2004**, *121*, 10657.
79. Boneberg, J.; Burmeister, F.; Schafle, C.; Leiderer, P. *Langmuir* **1997**, *13*, 7080.
80. Haynes; Duyne, C. L. V.; P, R. *J. Phys. Chem. B* **2001**, *105*, 5599.

81. Haynes, C. L.; Duyne, R. P. V. *Nano Letters* **2003**, *3*, 939.
82. Kosiorek, A.; Kandulski, W.; Chudzinski, P.; Kempa, K.; Giersig, M. *Nano Letters* **2004**, *4*, 1359.
83. Kosiorek, A.; Kandulski, W.; Glaczynska, H.; Giersig, K. *Small* **2005**, *1*, 439.
84. Fan, H.; Fuhrmann, B.; Scholza, R.; Syrowatkab, F.; Dadgarc, A.; Krostc, A.; Zacharias, M. *J. Cryst. Growth* **2006**, *287*, 34.
85. Park, K. H.; Lee, S.; Koh, K. H.; Lacerda, R.; Teo, K. B. K.; Milne, W. I. *J. Appl. Phys.* **2005**, *97*, 024311.
86. Fuhrmann, B.; Leipner, H. S.; Hoche, H.-R.; Schubert, L.; Werner, P.; Gosele, U. *Nano letters* **2005**, *5*, 2524.
87. Whitney, A. V.; Myers, B. D.; Duyne, R. P. V. *Nano Letters* **2004**, *4*, 1507.
88. Hicks, E. M. *J. Phys. Chem. B* **2005**, *109*, 22351.
89. Tan, B. J. Y. *J. Phys. Chem. B* **2005**, *109*, 11100.
90. Weekes, S. M.; Ogrin, F. Y.; Murray, W. A. *Nano letters* **2005**, *5*, 1053.
91. Zheng, Y. B.; Wang, S. J.; Huan, A. C. H.; Wang, Y. H. *J. Appl. Phys.* **2006**, *99*, 034308.
92. Weekes, S. M.; Ogrin, F. Y. *J. Appl. Phys.* **2005**, *97*, 10J503.
93. Cheung, C. L.; Nikolic, R. J.; Reinhardt, C. E.; Wang, T. F. *Nanotechnology* **2006**, *17*, 1339.
94. Wang, B.; Zhao, W.; Chen, A.; Chua, S.-J. *J. Cryst. Growth* **2006**, *288*, 200.
95. Holland, B. T.; Blanford, C. F.; Stein, A. *Science* **1998**, *281*, 538.
96. Yan, H.; Blanford, C. F.; Holland, B. T.; Smyrl, W. H.; Stein, A. *Chem. Mater.* **2000**, *12*, 1134.
97. Jiang, P.; Cizeron, J.; Bertone, J. F.; Colvin, V. L. *J. Am. Chem. Soc.* **1999**, *121*, 7957.
98. Velev, O. D.; Tessier, P. M.; Lenhoff, A. M.; Kaler, E. W. *Nature* **1999**, *401*, 548.
99. Park, S. H.; Xia, Y. *Chem. Mater.* **1998**, *10*, 1745.
100. Johnson, S. A.; Ollivier, P. J.; Mallouk, T. E. *Science* **1999**, *283*, 963.

101. Jiang, P.; Hwang, K. S.; Mittleman, D. M.; Bertone, J. F.; Colvin, V. L. *J. Am. Chem. Soc.* **1999**, *121*, 11630.
102. Yan, H.; Blanford, C. F.; Smyrl, W. H.; Stein, A. *Chemical Communications (Cambridge, United Kingdom)* **2000**, 1477.
103. Braun, P. V.; Wiltzius, P. *Nature* **1999**, *402*, 603.
104. Shiu, J.-Y.; Kuo, C.-W.; Chen, P.; Mou, C.-Y. *Chem. Mater.* **2004**, *16*, 561.
105. Cai, Y.; Ocko, B. M. *Langmuir* **2005**, *21*, 9274.
106. Bain, C. D.; Troughton, E. B.; Tao, Y. T.; Evall, J.; Whitesides, G. M.; Nuzzo, R. G. *J. Am. Chem. Soc.* **1989**, *111*, 321.
107. Vericat, C.; Vela, M. E.; Salvarezza, R. C. *Phys. Chem. Chem. Phys.* **2005**, *7*, 3258.
108. Ulman; A. *Chem. Rev. (Washington, D. C.)* **1996**, *96*, 1533.
109. Li, Y.; Huang, J.; McIver, R. T.; Hemminger, J. C. *J. Am. Chem. Soc.* **1992**, *114*, 2428.
110. Dubois, L. H.; Nuzzo, R. G. *Annu. Rev. Phys. Chem.* **1992**, *43*, 437.
111. Collard, D. M.; Fox, M. A. *Langmuir* **1991**, *7*, 1192.
112. Dubois, L. H.; Zegarski, B. R.; Nuzzo, R. G. *J. Am. Chem. Soc.* **1990**, *112*, 570.
113. Lee, T. R.; Carey, R. I.; Biebuyck, H. A.; Whitesides, G. M. *Langmuir* **1994**, *10*, 741.
114. Hickman, J. J.; Ofer, D.; Zou, C.; Wrighton, M. S.; Laibinis, P. E.; Whitesides, G. M. *J. Am. Chem. Soc.* **1991**, *113*, 1128.
115. Widrig, C. A.; Alves, C. A.; M.D.Porter *J. Am. Chem. Soc.* **1991**, *113*, 2805.
116. Alves, C. A.; Smith, E. L.; Porter, M. D. *J. Am. Chem. Soc.* **1992**, *114*, 1222.
117. Poirier, G. E.; Tarlov, M. J. *Langmuir* **1994**, *10*, 2853.
118. Dubois, L. H.; Zegarski, B. R.; Nuzzo, R. G. *J. Chem. Phys.* **1993**, *98*, 678.
119. Schreiber; F. *Prog. Surf. Sci.* **2000**, *65*, 151.
120. Poirier, G. E. *Chem. Rev.* **1997**, *97*, 1117.

121. Delamarche, E.; Michel, B. *Thin Solid Films* **1996**, *273*, 54.
122. Poirier, G. E. *Langmuir* **1997**, *13*, 2019.
123. Nicholas; Camillone, I.; Chidsey, C. E. D.; Liu, G.; Scoles, G. *J. Chem. Phys.* **1993**, *98*, 3503.
124. Schonenberger, C.; Jorritsma, J.; Sondag-Huethorst, J. A. M.; Fokkink, L. G. J.
125. Azzaroni, O.; Vela, M. E.; Martin, H.; Creus, A. H.; Andreasen, G.; Salvarezza, R. *C. Langmuir* **2001**, *17*, 6647.
126. Delamarche, E.; Michel, B.; Biebuyck, H. A.; Gerber, C. *Adv. Ma.* **1996**, *8*, 719.
127. Delamarche, E.; Michel, B.; Gerber, C.; Anselmetti, D.; Guentherodt, H. J.; Wolf, H.; Ringsdorf, H. *Langmuir* **1994**, *10*, 2869.
128. Poirier, G. E. *Chem. Rev.* **1997**, *97*, 1117.
129. Bucher, J.-P.; Santesson, L.; Kern, K. *Langmuir* **1994**, *10*, 979.
130. Brett, C. M. A.; Kresak, S.; Hianik, T.; Brett, A. M. O. *Electroanalysis* **2003**, *15*, 557.
131. Satjapipat, M.; Sanedrin, R.; Zhou, F. *Langmuir* **2001**, *17*, 7637.
132. Everett, W. R.; Welch, T. L.; Reed, L.; Fritsch-Faules, I. *Anal. Chem.* **1995**, *67*, 292.
133. Finklea, H. O.; Avery, S.; Lynch, M.; Furtch, T. *Langmuir* **1987**, *3*, 409.
134. Widrig, C. A.; Chung, C.; Porter, M. D. *J. Electroanal. Chem. Interf. Electrochem.* **1991**, *310*, 335.
135. Walczak, M. M.; Popenoe, D. D.; Deinhammer, R. S.; Lamp, B. D.; Chung, C.; Porter, M. D. *Langmuir* **1991**, *7*, 2687.
136. Sandhyarani, N.; Pradeep, T. *Vacuum* **1998**, *49*, 279.
137. Delamarche, E.; Michel, B.; Kang, H.; Gerber, C. *Langmuir* **1994**, *10*, 4103.
138. Clegg, R. S.; Reed, S. M.; Hutchison, J. E. *J. Am. Chem. Soc.* **1998**, *120*, 2486.
139. Murty, K. V. G. K.; Venkataramanan, M.; Pradeep, T. *Langmuir* **1998**, *14*, 5446.
140. Bai, C. D.; Whitesides, G. M. *J. Am. Chem. Soc.* **1988**, *110*, 6560.

141. Petrucci, M. G. L.; Kakkar, A. K. *J. Chem. Soc., Chem. Commun.* **1995**, 1577.
142. Bain, C. D.; Whitesides, G. M. *J. Am. Chem. Soc.* **1988**, *110*, 6560.
143. Templeton, A. C.; ; Wuelfing, W. P.; ; Murray, R. W.; *Acc. Chem. Res.* **2000**, *33*, 27.
144. Shon, Y.-S.; ; Mazzitelli, C.; ; Murray, R. W.; *Langmuir* **2001**, *17*, 7735.
145. Hostetler, M. J.; Templeton, A. C.; ; Murray, R. W.; *Langmuir* **1999**, *15*, 3782.
146. Murayama, H.; ; Narushima, T.; ; Negishi, Y.; ; Tsukuda, T.; *J. Phys. Chem. B* **2004**, *108*, 3496.
147. Templeton, A. C.; ; Hostetler, M. J.; ; Warmoth, E. K.; ; Chen, S.; ; Hartshorn, C. M.; ; Krishnamurthy, V. M.; ; Forbes, M. D. E.; ; Murray, R. W.; *J. Am. Chem. Soc.* **1998**, *120*, 4845.
148. Xia, Y.; ; Whitesides, G. M.; *Angewandte Chemie, International Edition* **1998**, *37*, 550.
149. Dammel, R. R.; ; Houlihan, F. M.; ; Sakamuri, R.; ; Rentkiewicz, D.; ; Romano, A.; *PMSE Preprints* **2004**, *90*, 283.
150. Tseng, A. A.; ; Chen, K.; ; Chen, C. D.; ; Ma, K. J.; *IEEE Transactions on Electronics Packaging Manufacturing* **2003**, *26*, 141.
151. Altissimo, M.; ; Fabrizio, E. D.; *Conference Proceedings - Italian Physical Society* **2003**, *82*, 771.
152. Bietsch, A.; ; Hegner, M.; ; Lang, H. P.; ; Gerber, C.; *Langmuir* **2004**, *20*, 5119.
153. Black, A. J.; Paul, K. E.; Aizenberg, J.; Whitesides, G. M. *J. Am. Chem. Soc.* **1999**, *121*, 8356.
154. Chiang, C. K.; Fincher, C. R.; Park, Y. W.; Heeger, A. J.; Shirakawa, H.; Louis, E. J.; MacDiarmid, A. G. *Phys. Rev. Lett.* **1977**, *39*, 1098.
155. Pohl, H. A.; Engelhardt, E. H. *J. Phys. Chem* **1962**, *66*, 2085.
156. Syed, A. A.; Dinesan, M. K. *Talanta* **1991**, *38*, 815.
157. Letheby; *H. J. Chem. Soc.* **1841**, *15*, 161.
158. Gilchrist, L. *J. Phys. Chem* **1904**, *8*, 539.
159. Bucherer, H. T. *Ber.* **1907**, *40*, 3412.

160. Green, A. G.; Woodhead, A. E. *J. Chem. Soc.* **1910**, 97, 2388.
161. Shachlette, L. W.; Wolf, J. F.; Gould, S.; Baughman, R. H. *J. Chem. Phys* **1987**, 88, 3955.
162. MacDiarmid, A. G.; Chiang, J. C.; Richter, A. F.; Epstein, A. J. *Synthe. Met.* **1987**, 18, 285.
163. Surville, R. d.; Jozefowicz, M.; Yu, L. T.; Perichon, J.; Buvet, R. *Electrochim. Acta* **1968**, 13, 1451.
164. Jozefowicz, M.; Perichon, J. H.; Yu, L. T.; Buvet, R. In *Br. Patent*; Patent, B., Ed. 1970; Vol. No. 121656.
165. Syed, A. A.; Dinesan, M. K.; Genies, E. M. *Bull. Electrochem.* **1988**, 4, 737.
166. Erdem, E.; Sacak, M.; Karakisla, M. *Polym. Int.* **1996**, 39, 153.
167. Li, S.; Dong, H.; Cao, Y. *Synthe. Met.* **1989**, 29.
168. Diaz, A. F.; Logan, J. A. *J. Electroanal. Chem.* **1980**, 111, 111.
169. Mohilner, D. M.; Adams, R. N.; Argersinger, W. J. *J. Am. Chem. Soc.* **1962**, 84, 3618.
170. Breitenbach, M.; Heckner, K.-H. *J. Electroanal. Chem.* **1971**, 29, 309.
171. Hand, R. L.; Nelson, R. F. *J. Am. Chem. Soc.* **1974**, 96, 850.
172. Genies, E. M.; Tsintavis, C. *J. Electroanal. Chem.* **1985**, 195, 109.
173. Genies, E. M.; Syed, A. A.; Tsintavis, C. *Mol. Cryst. Liq. Cryst.* **1985**, 121, 181.

CHAPTER 2

**THE INFLUENCE OF COUNTER ANIONS ON THE UNDERPOTENTIAL
DEPOSITION OF MERCURY(II) ON AU(111): TEMPERATURE DEPENDENT
STUDIES**

2.1 Introduction

The underpotential deposition (UPD) of metallic elements on to dissimilar metal substrates has been known for nearly a century.¹ Research on UPD has led to important insights into the atomic-level processes involved in metal electrodeposition, two-dimensional nucleation and growth phenomena, and compound semiconductor growth. Metal UPD is governed primarily by the interactions between the substrate and the element being deposited, as evidenced by the high degree of correlation between the shift of the UPD wave from the bulk deposition potential (ΔE), with the metal-substrate work function difference ($\Delta\phi$) for nearly all known UPD pairs.²⁻⁴ Nevertheless, other factors, including the substrate's surface structure, metal-counter anion and substrate-counter anion interactions also have been shown to influence the UPD process.

The effects of the counter anion on metal UPD are well studied, and appear to be quite general.⁵⁻¹⁰ Specific adsorption of anions can hinder the adsorption of other, less strongly adsorbing species, and can therefore play a determining role in the kinetics of

the UPD process. For example, Ross et al. have shown that the presence of ordered halide layers exerts a strong influence on the initial stages of Cu UPD on Pt(111) surfaces.¹¹ These workers observed the formation and reconstruction of ordered CuX bilayers ($X = \text{Br}^-$, Cl^-) prior to the onset of Cu UPD. Laibinis and co-workers investigated the UPD of Ag onto Au(111) surfaces from sulfuric acid electrolyte in the presence of trace levels of chloride.¹² Repetitive deposition and stripping cycles resulted in a shift of the UPD potential to more negative values. The increased nobility of the Au(111) surface was attributed to the influence of chloride ions on the formation of the Ag monolayer. In a recent study of the same system, Kwak et al. used AFM to probe the influence of Cl^- adsorption on Ag UPD at Au(111).¹³ When Ag UPD was carried out in perchloric acid media, only two overlayer structures—a low coverage (4x4) and a saturation coverage (1x1)—were observed. On the other hand, when chloride ions were pre-adsorbed on the Au(111) surface, multiple ordered structures were observed by AFM which could be correlated to specific voltammetric features.

The deposition of Hg^{2+} on Au(111) surfaces exemplifies the wide range of behaviors that is possible in UPD systems. Moreover, this system is particularly well studied, and high quality electrochemical, spectroscopic, and structural data are available for a variety of supporting electrolytes.¹⁴⁻²³ In a non-interacting electrolyte such as perchloric acid, the single voltammetric wave in the UPD region is reversible (i.e., $\Delta E_p = 0$) with a nearly Gaussian peak shape characteristic of Langmuir adsorption (i.e., peak width = $90.6/n$ mV). In (bi)sulfate media, on the other hand, an order-disorder transition is observed prior to the onset of UPD, in which an ordered layer of pre-adsorbed (bi)sulfate is converted to an ordered mercury(I) sulfate layer. Finally, in acetic acid

solutions, mercury(II)-acetate complex ions exist in the electrolyte phase, hindering the UPD process, which leads to a shift of the peak potentials and peak separations.

In spite of the extensive literature on metal UPD, there is a lack of thermodynamic data available on these systems. Such information is of obvious fundamental interest, and is also important in determining optimum growth temperatures for the electrochemical deposition of compound semiconductors, for example. Weaver and co-workers pioneered the use of non-isothermal electrochemical cells to measure the reaction enthalpies and entropies of electron transfer reactions involving transition metal complexes.²⁴ More recently, Jerkiewicz and his group have taken the lead in developing similar approaches to probe surface reactions including H UPD,²⁵⁻³¹ oxide layer formation on Pd,³² and bismuth UPD.³³ In addition, Harrington and co-workers have used temperature dependent voltammetric measurements to investigate Ag UPD on naked Au(111) and I-Pt(111) surfaces.³⁴

In this paper, temperature dependent studies of the Hg²⁺ UPD on Au(111) surfaces were carried out in perchloric acid, sulfuric acid and acetic acid media in order to study the influence of counter anion on the thermodynamics of UPD under experimental conditions where anion interactions are expected to be small, where anion-surface interactions dominate, and where anion metal ion interactions are expected to play an important role, respectively.

2.2 Experimental

Materials. HgO (99.99 % purity) was obtained from the Merck Chemical Company and used as received. Au wire (0.762 mm diameter, 99.999% purity) was

obtained from Alfa Aesar. Millipore-Q purified distilled water (18 M Ω) was used to make up all solutions.

Substrate Preparation. Au wire electrodes were cleaned by rinsing sequentially with distilled water, absolute ethanol, piranha solution (1:3 v/v 30% H₂O₂, 18 M H₂SO₄), distilled water, and absolute ethanol. After being dried in a stream of flowing nitrogen, the clean Au wire was melted in a H₂/O₂ flame to form a 1.5-2.5 mm diameter droplet at the end of the wire. The droplet was then annealed in the flame until numerous small Au(111) facets appeared across the surface of the polycrystalline Au bead. Prior to all experiments, the Au electrodes were annealed in a H₂ flame for an additional 15 minutes. Individual (111) facets were then isolated using a nonconductive silicone-based epoxy. Control experiments comparing the electrochemical response of these surfaces to conventional polished Au(111) electrodes showed conclusively that the epoxy was chemically inert. This experimental protocol allowed freshly prepared Au(111) facets to be used for each experiment, and allowed us to make measurements on surfaces containing a minimum of concentration of surface defects (such as those induced by mechanical polishing).

Electrochemistry. All cyclic voltammetry experiments were performed in home made single compartment Teflon cells (ca. 20 mL total volume) using a BAS-Epsilon workstation. A standard three-electrode configuration was used in which the Au bead was the working electrode, a Pt wire was the counter electrode and Ag|AgCl|KCl(sat) was the reference electrode. All potentials are referenced to Ag|AgCl|KCl(sat). The electrochemical cell was placed in a Faraday cage to isolate it from environmental electronic noise sources. Before and after transferring the sample, the solution was

thoroughly degassed with ultrapure Ar and was isolated from air with a blanket of Ar during experiments. The scan rate was 1 mV/s unless otherwise noted.

Temperature-dependent electrochemical measurements. Two experimental approaches were followed to obtain thermodynamic functions from temperature-dependent electrochemical measurements: isothermal and thermal (non-isothermal) cells. In the former case, the compartment for the reference electrode (RE) was maintained at the same temperature as the compartment for the working electrode (WE). Because the temperature of the reference electrode changes in an isothermal cell, temperature dependent measurements will provide information about the overall cell reaction (i.e., including the half-reaction at the reference electrode). However, if the temperature dependence of the reference electrode is known independently, thermodynamic analysis of the half-reaction taking place at the WE can be carried out. In the case of the thermal (non-isothermal) cell, on the other hand, the temperature of the WE compartment changes while that of the RE is maintained at a constant temperature. In this case, the temperature coefficient of the RE need not be known.

In this work, we used both isothermal and thermal cells. For measurements using thermal cells, the reference electrode was placed in a compartment containing the same electrolyte as the working electrode compartment. The two compartments of the cell were connected using a capillary tube. For measurements with the isothermal cell, the reference electrode was kept in the electrochemical cell and the following equation was used to correct for the temperature dependence of the reference electrode potential.

$$E_{\text{Ag/AgCl}, 298} = E_{\text{Ag/AgCl}, T} + (T-298)dE/dT \quad (2.1)$$

In this equation, all of the symbols have their conventional meanings. The literature value of 7.3×10^{-4} V/K for dE/dT was used in our analysis. We found that thermodynamic functions calculated using both methods gave identical results within experimental error.

In our experiments, the electrochemical cell was immersed in a water bath whose temperature was controlled to within ± 0.1 K by means of a thermostat. The water level in the bath was maintained above that of the electrolyte in the cell to ensure uniformity of temperature. The temperatures in the water bath and the electrochemical cell were measured and found to agree to within ± 0.1 K.

2.3 Results and discussion

2.3.1. Room Temperature Cyclic Voltammetry

The steady state voltammetric response of an Au(111) electrode immersed in 0.10 M HClO₄ supporting electrolyte containing 1.0 mM Hg²⁺ (from HgO) at 23°C is shown in Figure 2.1. A single pair of waves corresponding to Hg UPD was observed at approximately +0.900 V when the potential was scanned between +0.650 and +1.05 V at 1 mV/s. The linear scan rate dependence of the peaks (not shown) and the nearly 0 mV peak separation are consistent with a surface-confined reaction such as UPD. In addition, the peaks are quasi-Gaussian in shape with a full width half maximum (FWHM) of ca. 47 mV, consistent with a two-electron reduction in which mercury adsorption is described by the Langmuir isotherm. Hg UPD from sulfuric acid supporting electrolyte displays a distinctly different behavior, and a representative voltammogram is shown in Figure 2.2. The main voltammetric features, labeled C1 and A1, occur at a potential close to what

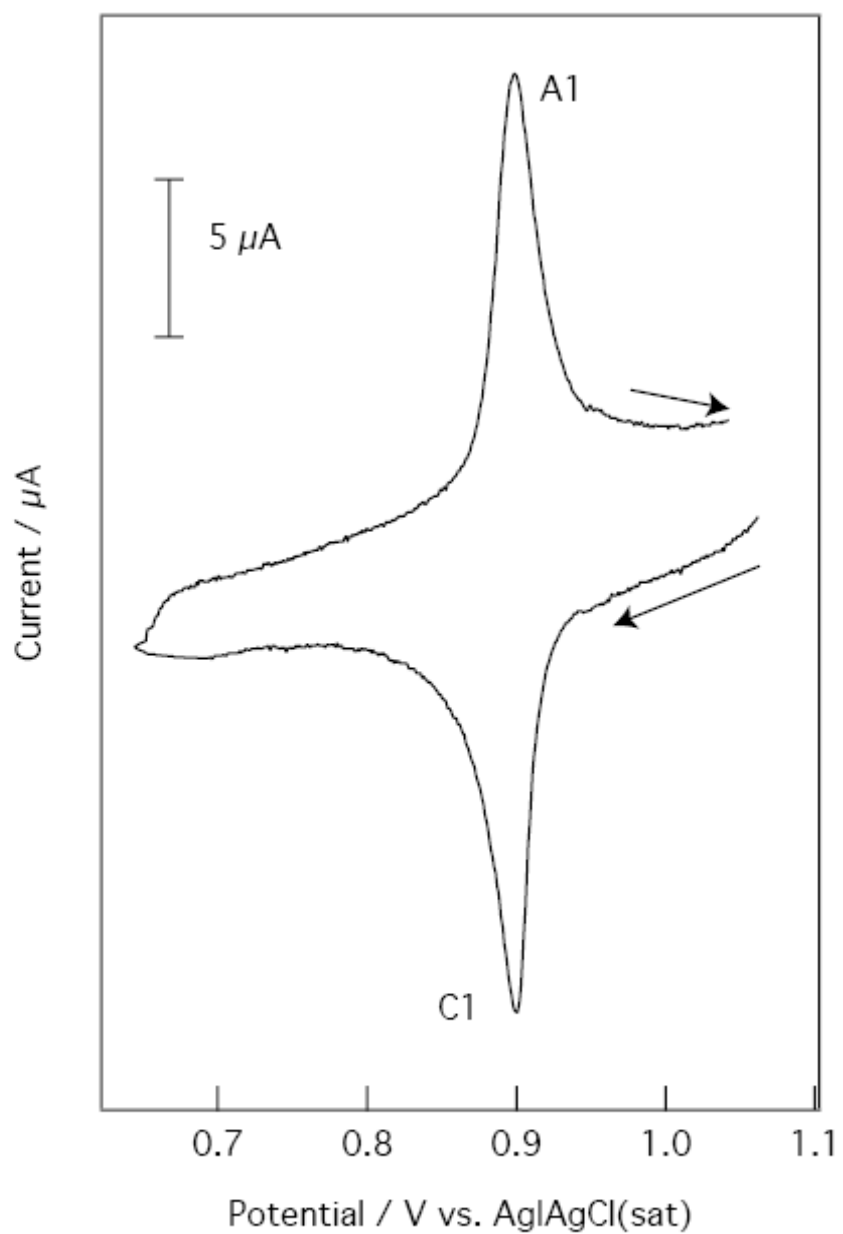


Figure 2.1. Room temperature cyclic voltammetry of an Au(111) electrode immersed in 0.10 M HClO₄ + 1.0 mM Hg²⁺ in the UPD region. The scan rate was 1 mV/s.

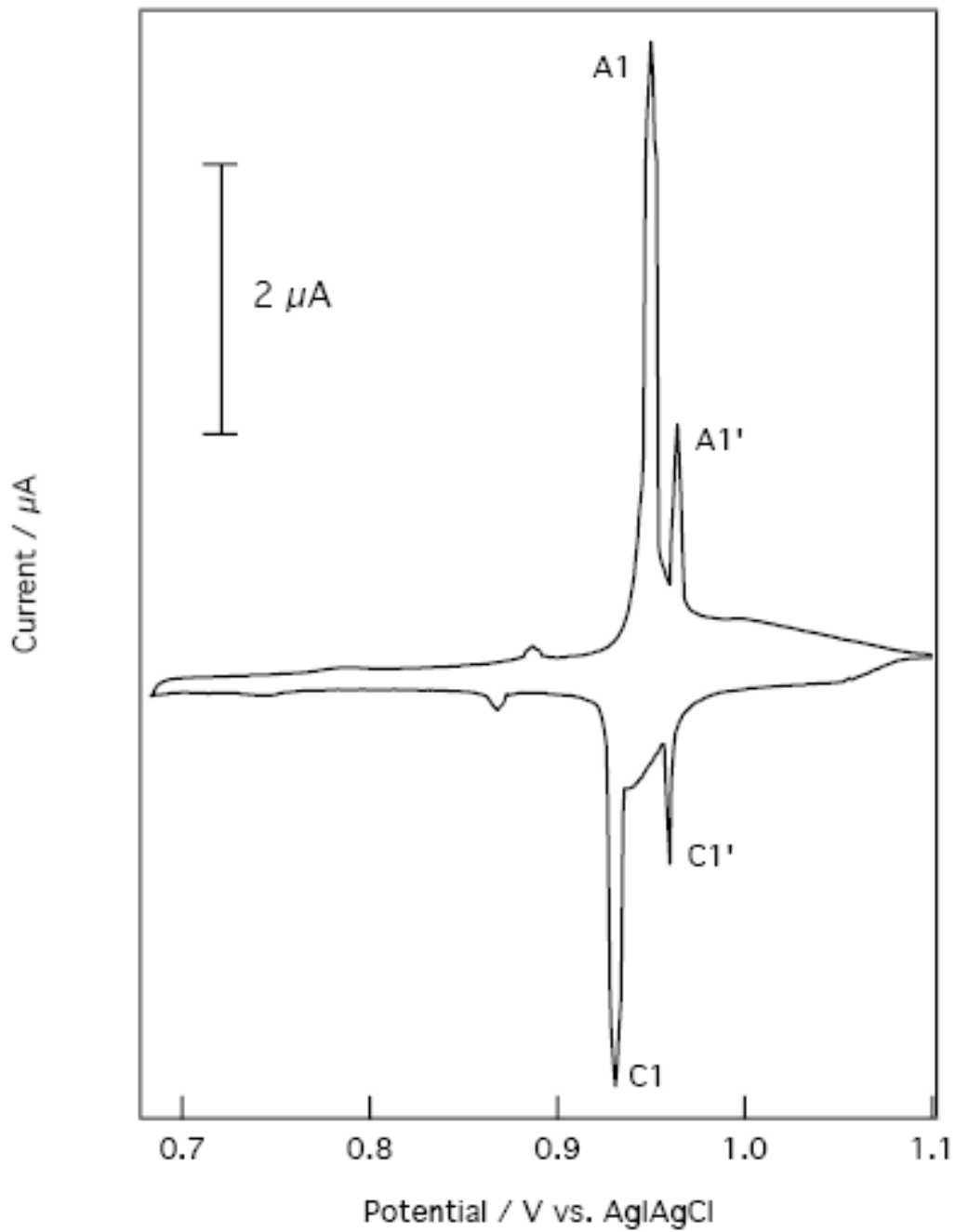


Figure 2.2. Room temperature cyclic voltammetry of an Au(111) electrode immersed in 0.10 M H₂SO₄ + 1.0 mM Hg²⁺ in the UPD region. The scan rate was 1 mV/s.

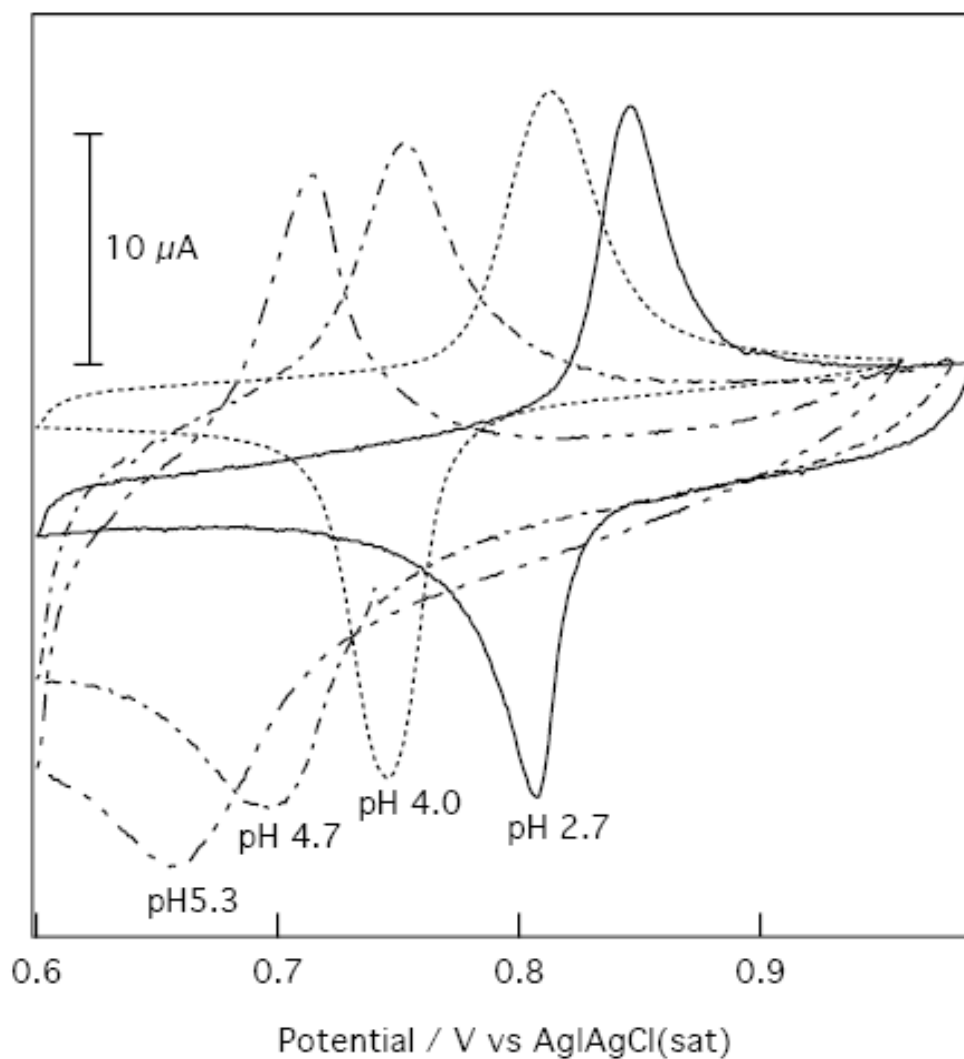


Figure 2.3. Room temperature cyclic voltammetry of an Au(111) electrode immersed in 0.10 M $\text{HC}_2\text{H}_3\text{O}_2$ + 1.0 mM Hg^{2+} in the UPD region. The pH of each solution is indicated on the graph. The scan rate was 1 mV/s in all cases.

was observed in perchloric acid, but the peaks are significantly sharper. In addition, peaks C1/A1 are accompanied by two current spikes, labeled C'1/A'1, that are the characteristic signature of an order-disorder phase transition. Indeed, previous research has shown that a stable $\sqrt{3}\times\sqrt{7}$ (bi)sulfate adlayer is present on the Au(111) surface in the region positive of the UPD potential, and that the initial stages of Hg UPD triggers the order-to-disorder phase transition. Finally, Hg UPD from acetic acid supporting electrolyte displayed a completely distinct behavior from what was seen in either perchloric acid or sulfuric acid media (Figure 2.3). This voltammetry, characterized by a negative shift of the formal potential (i.e., $E^{0'} = 1/2 (E_{p,c} + E_{p,a})$) from the value observed in HClO₄, and a non-zero peak separation, is consistent with the existence of Hg(II)-acetate complexes in solution. In fact, mercury(II)-acetate complex ions of up to a 1:4 stoichiometry are well known.¹⁵ Complex ion formation has the effect of stabilizing Hg(II) relative to Hg(I), shifting the formal potential to more negative values. The presence of Hg(II)-acetate complex ions was confirmed by varying the solution pH at a constant formal concentration of acetate (i.e., $[HC_2H_3O_2] + [C_2H_3O_2^-] = 0.10$ M), since the formation constants for mercury(II)-acetate complex ions are pH dependent. As the pH is increased from 1.3 to 5.3, the formal potential shifts from a value of about 890 mV to 785 mV, as shown in Figure 2.3. As noted previously, the fact that the peak separations (ΔE_p) are non-zero is characteristic of a kinetically slow chemical step coupled to a rapid electron transfer process. Presumably, this is related to the dissociation of Hg(II)-acetate complex ions upon reduction. Our observations in all three electrolyte systems are the same within experimental error as those previously reported by Abruna and co-workers.¹⁵

2.3.2. Temperature Dependent Studies

Cyclic voltammograms in the Hg UPD region in 0.10 M HClO₄ electrolyte recorded as a function of temperature are shown in Figure 2.4. Arrows indicate the direction that the peaks shift. The peak current density, j_p , and total charge density, q_{ads} , values for the deposition wave are plotted as functions of temperature in Figure 2.5. The fact that there is no significant variation of q_{ads} or j_p with T indicates that the surface coverage of Hg is not a sensitive function of temperature on the range of temperatures that were investigated (i.e., 298 – 358 K). The peak current density observed for peak C1 exhibits a slight but noticeable decrease as the temperature increases, but the magnitude of the overall decrease is only about 0.10%. This slight decrease could be due to changes in surface morphology as the temperature is changed. The value of q_{ads} has a nearly constant value of 175.2 $\mu\text{C cm}^{-2}$, which equates to a coverage of 0.88. This coverage is in good agreement with earlier work in which the coverage of Hg UPD layers was found to be between 0.9-0.92. At a constant Hg surface concentration, the reaction entropy for the Hg UPD process can be calculated from the temperature dependence of the UPD peak potential (or formal potential) according to equation 2.2.

$$\Delta S^0 = nF dE_{\text{UPD}}/dT \quad (2.2)$$

In this equation, n is the number of electrons exchanged and F is the Faraday constant. Experimentally, dE^0_{UPD}/dT factors were determined in two ways: by plotting

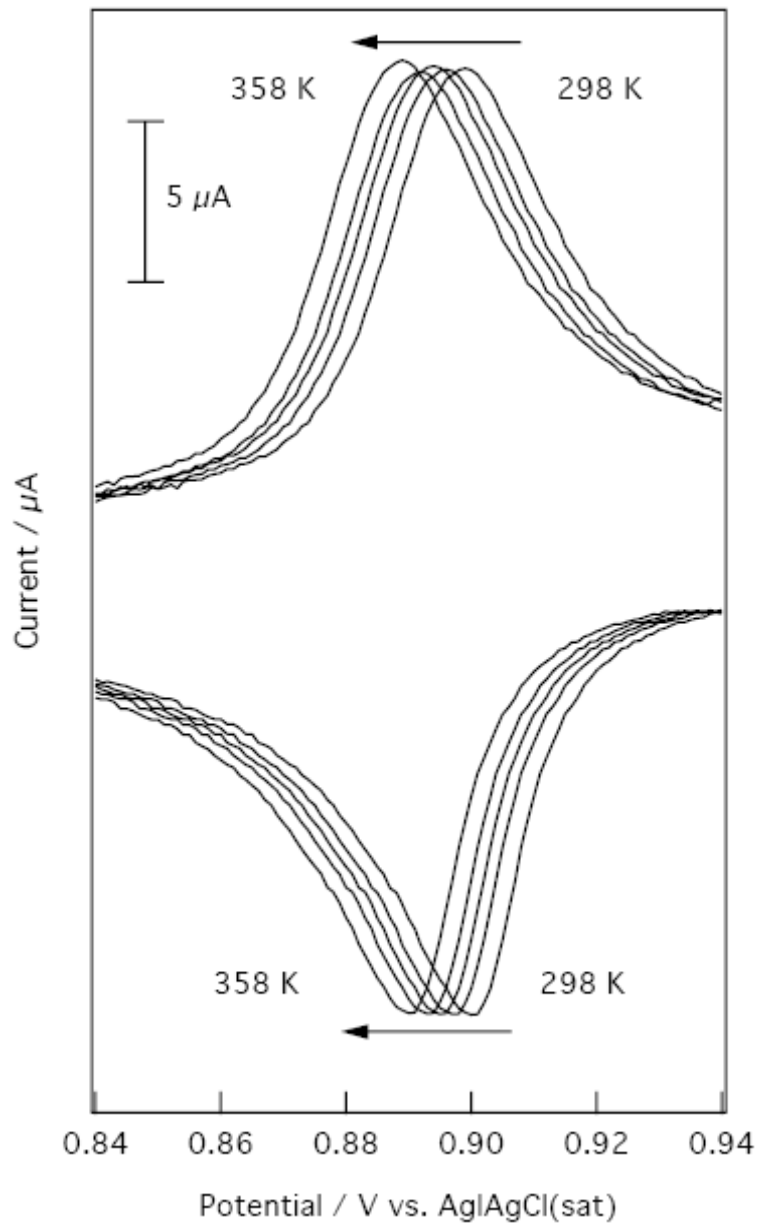


Figure 2.4. Temperature dependent cyclic voltammetry of an Au(111) electrode immersed in 0.10 M HClO_4 + 1.0 mM Hg^{2+} in the UPD region. The temperature range was from 298 K to 358 K. Arrows indicate the direction that the peaks shift. The scan rate was 1 mV/s.

cathodic peak potentials against temperature and by plotting the formal potential against temperature, Figure 2.6. The values obtained by each method were in good agreement, and the average of the two measurements is reported. For Hg UPD from 0.10 M HClO₄, the dE_{UPD}^0/dT factor was found to be -1.6×10^{-4} V/K, corresponding to a ΔS_{UPD}^0 of -30.9 J/mol-K, assuming n to be two. The electrosorption valency of mercury UPD has been determined by previous workers to be 2, validating this assumption.

The standard enthalpy of the UPD reaction, ΔH^0 , can also be determined from the temperature dependence of the cyclic voltammetry. According to equation 2.3, the slope of the (E_{UPD}^0/T) versus $1/T$ plot corresponds to ΔH_{UPD}^0 . ΔH_{UPD}^0 for perchloric acid electrolyte was found experimentally to be -182.1 kJ/mol.

$$\Delta H^0 = -nFd(E_{\text{UPD}}^0/T)/d(1/T) \quad (2.3)$$

Temperature dependent measurements for Hg UPD from 0.10 M H₂SO₄ acid and HC₂H₃O₂ were carried out as described above for the HClO₄ system, and analyzed in an identical fashion. The thermodynamic parameters for the Hg UPD system as a function of electrolyte are summarized in Table 2.1.

Table 2.1. Summary of Hg UPD thermodynamic data obtained from temperature-dependent cyclic voltammetry measurements.

Electrolyte	HClO ₄	H ₂ SO ₄	HC ₂ H ₃ O ₂			
			pH 2.7	pH 4.0	pH 4.7	pH 5.3
dE_{UPD}/dT (V/K)	$-1.61 \pm 0.03 \times 10^{-4}$	$-9.48 \pm 0.04 \times 10^{-5}$	$8.50 \pm 0.03 \times 10^{-5}$	$3.06 \pm 0.05 \times 10^{-4}$	$4.00 \pm 0.03 \times 10^{-4}$	$4.33 \pm 0.04 \times 10^{-4}$
ΔS (J/mol-K)	-30.9 ± 0.6	-18.3 ± 0.7	$+16.4 \pm 0.6$	$+59.1 \pm 0.9$	$+77.2 \pm 0.6$	$+83.5 \pm 0.8$
$d(E_{\text{UPD}}/T)/d(1/T)$ (V)	$9.43 \pm 0.06 \times 10^{-4}$	$9.54 \pm 0.05 \times 10^{-4}$	$7.75 \pm 0.05 \times 10^{-4}$	$6.55 \pm 0.05 \times 10^{-4}$	$5.77 \pm 0.07 \times 10^{-4}$	$5.27 \pm 0.05 \times 10^{-4}$
ΔH (kJ/mol)	-182 ± 1	-184 ± 1	-150 ± 1	-126 ± 1	-111 ± 1	-102 ± 1

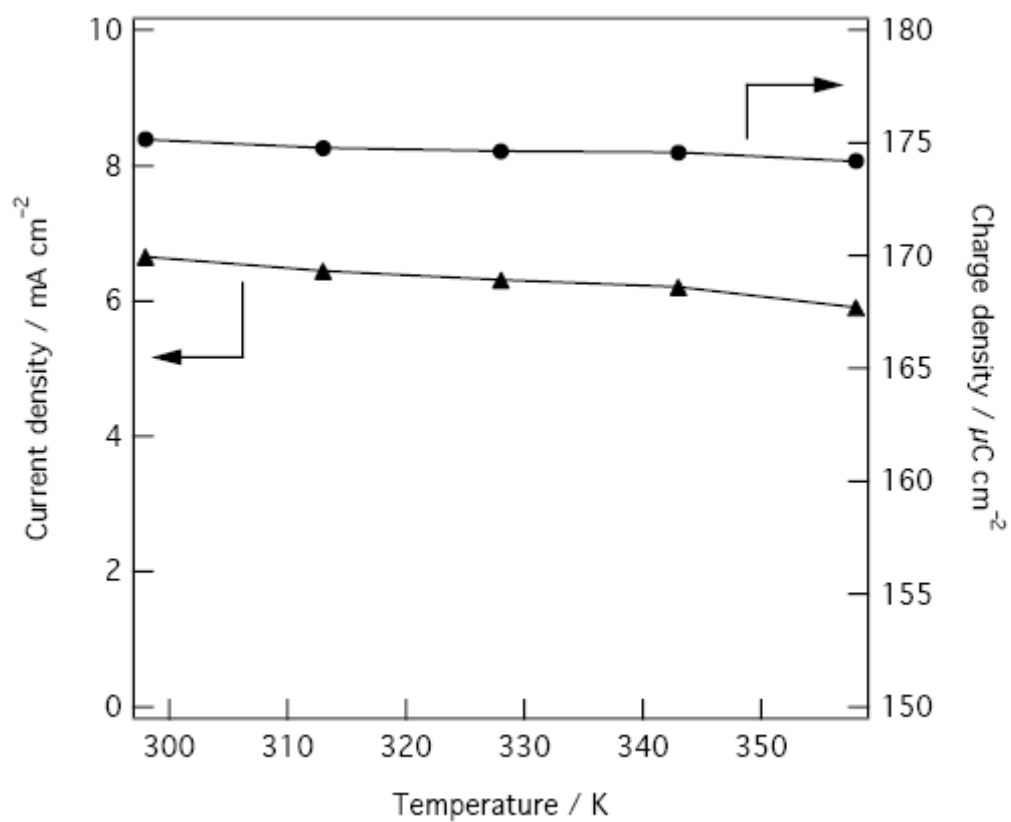


Figure 2.5. Plots of $j_{p,cathodic}$ (left hand y-axis) and q_{ads} (right hand y-axis) as a function of temperature.

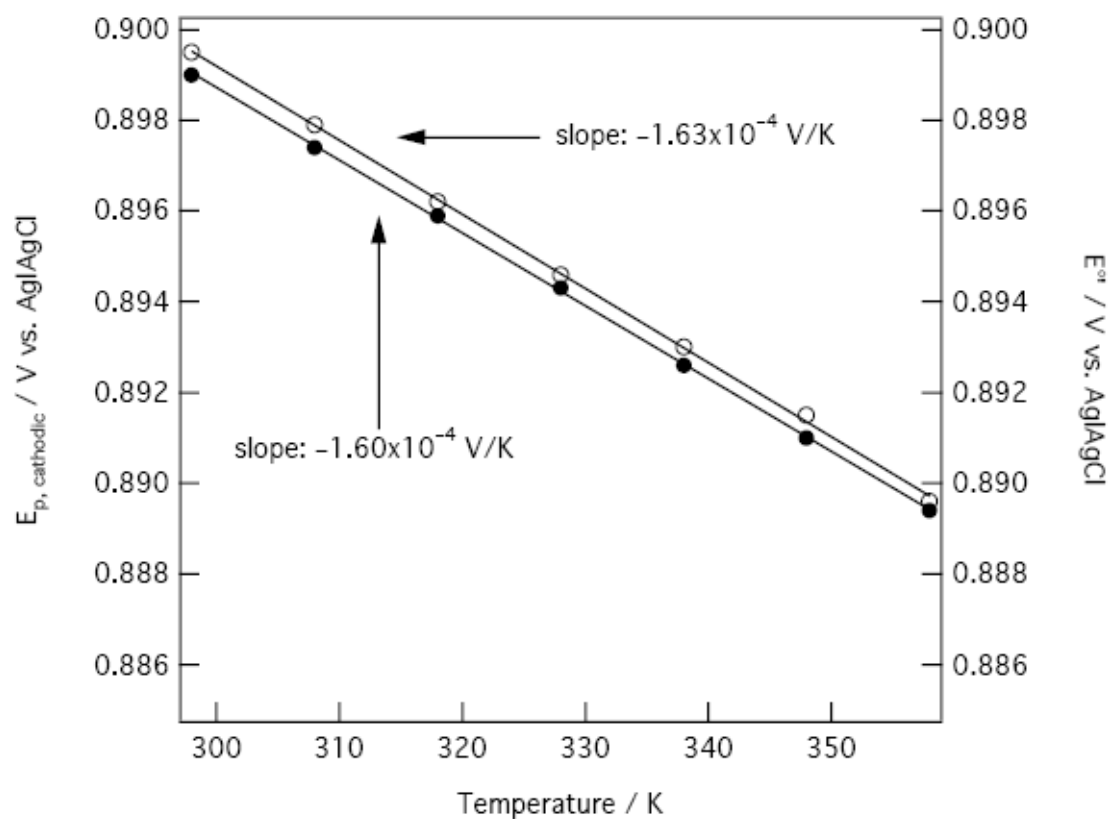


Figure 2.6. Determination of dE_{UPD}/dT values using $E_{p,cathodic}$ (filled circles) and E°_f (open circles).

2.3.3 Hg UPD from perchloric acid and sulfuric acid

The reaction entropy for Hg UPD from perchloric acid electrolyte of -30.9 J/mol-K can be compared to values obtained previously for similar UPD systems. Temperature dependent studies of Ag UPD on Au(111) have been reported recently.³⁵ Two voltammetric features, corresponding to low coverage and high coverage Ag UPD structures, respectively, were observed. However, the Ag coverage associated with both of these UPD peaks was found to be temperature dependent, which precluded calculation of the reaction entropy. Nevertheless, the coverage of both UPD structures was found to be constant over a subset of the temperatures investigated (i.e., $273 \text{ K} \leq T \leq 293 \text{ K}$). On this restricted temperature range, dE_{UPD}/dT values of $-2.074 \times 10^{-3} \text{ V/K}$ and $-1.7 \times 10^{-3} \text{ V/K}$ were reported for the first and second UPD peaks, respectively. The entropy value we measured for Hg UPD corresponds to a dE_{UPD}/dT value of $-1.69 \times 10^{-4} \text{ V/K}$, which is significantly smaller than the value observed for Ag UPD, even when taking the different number of electrons transferred into account. The only other UPD system for which entropy data have been reported is H atom UPD. Jerkiewicz et al. report $\Delta S = -44.8 \text{ J/mol-K}$ for H atom UPD on Pt(110).²⁵ On the other hand, entropies for H atom UPD on Pt(111) were found to vary from -79 to -63 J/molK , as the coverage increased from a limiting value of 0 to 0.67.³¹ The difference in entropy values observed on the two low Miller index planes was attributed to the more open surface structure and shallower chemisorption potential on the Pt(110) as compared to the Pt(111) surface. This was explained as arising because adsorbed H atoms have higher surface mobilities on the more open Pt(110) surface, accounting for the more positive entropy change. The coverage dependent behavior observed on the Pt(111) surface can also be qualitatively

understood in terms of relative surface mobilities. Specifically, at high coverage, adatom mobilities are significantly reduced compared to the low coverage case, leading to a less negative reaction entropy. It should be noted that this trend is also reflected in the Ag UPD data discussed earlier. The dE_{UPD}/dT value of the second UPD peak (higher coverage) is significantly smaller than that of the first peak (lower coverage). As mentioned previously, the coverage of the Hg UPD layer on Au(111) is ca. 0.88 in perchloric acid. Thus, the ΔS value we observe appears to be reasonable for the formation of a high coverage Hg atomic layer.

The observed entropy change in sulfuric acid electrolyte is more positive (less negative) than in perchloric acid media, and can be understood as follows. At voltages positive of the Hg UPD potential, Itaya and co-workers identified an ordered $\sqrt{3}\times\sqrt{7}$ (bi)sulfate adlayer on Au(111).³⁶ This ordered overlayer structure is lifted via an order-disorder phase transition initiated during the initial phases of Hg UPD. An ordered $\sqrt{3}\times\sqrt{19}$ mercurous sulfate structure is observed on Au(111) electrodes at potentials negative of the UPD potential. It is likely that the adsorbed sulfate and bi-sulfate ions interact electrostatically with Hg^{2+} prior to the onset of UPD and act to template the growth of the incipient Hg_2SO_4 layer. These interactions would reduce the mobility of the interfacial Hg^{2+} ions, resulting in a less negative entropy change for the UPD process. Strong electrostatic interactions between UPD monolayers and ions present in the supporting electrolyte have been observed in numerous electrochemistry-UHV studies. For example, previous work from our laboratory has shown the presence of sulfate ions in Zn UPD layers on Au surfaces.

It is interesting to compare the UPD of Hg onto $(\sqrt{3}\times\sqrt{7})\text{-HSO}_4^-/\text{Au}(111)$ to the UPD of Ag onto the $(\sqrt{7}\times\sqrt{7})\text{R19.1}^\circ\text{-I}/\text{Pt}(111)$ surface, a system whose temperature dependent electrochemistry has been investigated by Feliu and co-workers. A reaction entropy of +30 J/mol-K was reported for Ag UPD onto iodine modified Pt(111). As first noted by Hubbard, the behavior of this system is complicated by a place exchange reaction between the Ag UPD layer and the surface I atoms, although more recent measurements call this interpretation in to question.^{37,38} Thus, despite some obvious similarities, this system is not directly comparable to Hg UPD.

The enthalpy of reaction for Hg UPD was measured to be approximately -180 kJ/mol in both perchloric acid and sulfuric acid supporting electrolytes. Jerkiewicz and co-workers reported a ΔH of -125 kJ/mol for Bi UPD on Pt(111).³³ In addition, heats of adsorption for mercury on a number of transition metal surfaces (where it is known that no alloy forms) have been reported in the surface science literature.³⁹⁻⁴¹ Values range from about -50 to -150 kJ/mol, and are a sensitive function of Hg coverage. In contrast, Hg-Au alloys are well known, and this fact may account for the more exothermic reaction enthalpy observed in the present case.

2.3.4. Hg UPD from acetic acid

In acetic acid supporting electrolyte, solution phase mercury(II) acetate complexes of up to a 1:4 stoichiometry can form, leading to voltammetry that is both pH- and T-dependent. As the pH was made more basic, a larger fraction of the acetic acid exists in the form of acetate ions, which favors the formation of mercury(II)-acetate complex ions, and accounts for the observed negative shift of the UPD formal potential

with increasing pH. In addition, we would expect the entropy change for the UPD process to be more positive under conditions where the concentration of complex ions is higher, due to the dissociation of mercury(II)-acetate complex ions as mercury is reduced onto the Au(111) surface. On the other hand, as the pH was lowered, acetate is protonated to form acetic acid, and we expect the UPD behavior to converge to what is observed in pure perchloric acid supporting electrolyte, as is indeed the case. As can be seen from Table 2.1, the observed dependence of the reaction entropy on pH is in line with these expectations. The UPD reaction enthalpy becomes more endothermic as the electrolyte pH is increased. This suggests that the formation of mercury(II)-acetate complex ions weakens the interaction between mercury and gold. These effects are illustrated in Figure 2.7, which shows a plot of the ΔS_{UPD} and ΔH_{UPD} versus the logarithm of the free Hg concentration calculated using the known conditional formation constants for mercury acetate complexes. If the number of acetate ligands bound to Hg^{2+} were fixed, one would expect a linear log plot.

The non-linear log plot indicates that the identity of the mercury(II)-acetate complex is changing over the range of pHs investigated.

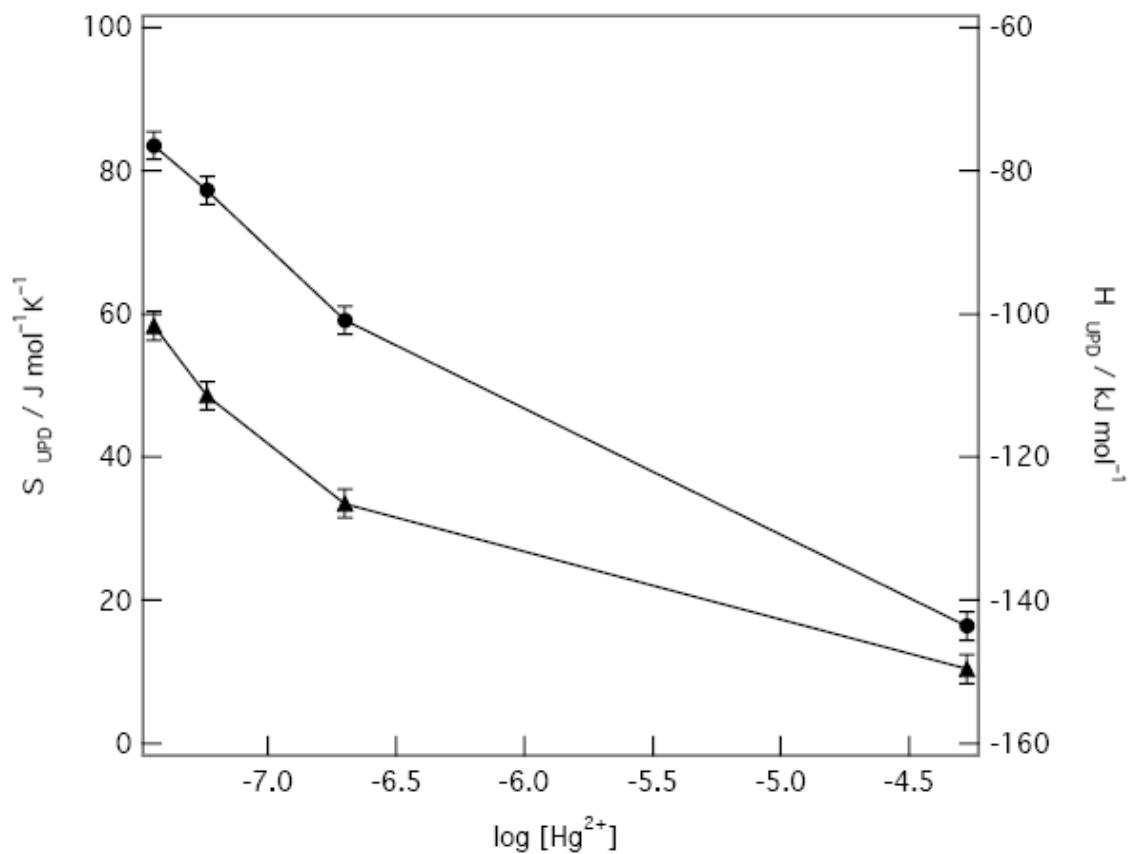


Figure 2.7. Plot of experimental values of ΔS_{UPD} (circles) and ΔH_{UPD} (triangles) versus the calculated free mercury(II) concentration. See text for details.

2.4 Conclusion

We have measured reaction entropy and enthalpy values for the UPD of mercury from a series of different electrolytes in which anion interactions could be varied from essentially non-interacting (HClO_4) to strongly interacting with either the Au(111) substrate (H_2SO_4) or the Hg^{2+} itself ($\text{HC}_2\text{H}_3\text{O}_2$). Although Hg UPD appears to be an enthalpy-controlled process overall, significant entropic effects were observed, especially in the case of Hg(II)-acetate complex ion formation.

2.5 References

1. Herrero, E.; Buller, L. J.; Abruna, H. D. *Chem. Rev.* **2001**, *101*, 1897.
2. Gerischer, H.; Kolb, D. M.; Pazasnyski, M. *Surf. Sci.* **1974**, *43*, 662.
3. Kolb, D. M.; Przasnyski, M.; Gerischer, H. *J. Electroanal. Chem. Interfacial Electrochem.* **1974**, *54*, 25.
4. Kolb, D. M.; Gerischer, H. *Surf. Sci.* **1975**, *51*, 323.
5. Arenz, M.; Stamenkovic, V.; Schmidt, T. J.; Wandelt, K.; Ross, P. N.; Markovic, N. M. *Surf. Sci.* **2003**, *523*, 199.
6. Soldo, Y.; Sibert, E.; Tourillon, G.; Hazemann, J. L.; Levy, J. P.; Aberdam, D.; Faure, R.; Durand, R. *Electrochim. Acta* **2002**, *47*, 3081.
7. Futamata, M.; *Chem. Phys. Letters* **2001**, *333*, 337.
8. Horanyi, G. *J. Solid State Electrochem.* **2000**, *4*, 177.
9. Nishihara, C.; Iwata, K.; Tai, T.; Yuasa, M.; Sekine, I.; Nozoye, H. *Electrochem. Commun.* **1999**, *1*, 104.
10. Herrero, E.; Glazier, S.; Buller, L. J.; Abruna, H. D. *J. Electroanal. Chem.* **1999**, *461*, 121.
11. Lucas, N. M. M. C. A.; Tidswell, I. M.; Ross, P. N. *Physica B* **1996**, *221*, 245.
12. Michalitsch, B. J. P. R.; Laibinis, P. E. *Langmuir* **2000**, *16*, 6533.
13. Lee, I. O. J.; Hwang, S.; Kwak, J.; *Langmuir* **2002**, *18*, 8025.
14. Li, J.; Herrero, E.; Abruna, H. D. *Colloids Surf. A* **1998**, *134*, 113.
15. Herrero, E.; Abruna, H. D. *J. Phys. Chem. B* **1998**, *102*, 444.
16. Herrero, E.; Buller, L. J.; Li, J.; Finnefrock, A. C.; Salomon, A. B.; Alonso, C.; Brock, D.; Abruna, H. D. *Electrochim. Acta* **1998**, *44*, 983.
17. Abruna, H. D.; Feliu, J. M.; Brock, J. D.; Buller, L. J.; Herrero, E.; Li, J.; Gomez, R.; Finnefrock, A. *Electrochim. Acta* **1998**, *43*, 2899.
18. Zeng, X. in State Univ. of New York, Buffalo, NY, USA. FIELD URL.; 1997, p. 219
19. Li, J.; Abruna, H. D. *J. Phys. Chem. B* **1997**, *101*, 244.

20. Li, J.; Abruna, H. D. *J. Phys. Chem. B* **1997**, *101*, 2907.
21. Herrero, E.; Abruna, H. D. *Langmuir* **1997**, *13*, 4446.
22. Herrero, E.; Li, J.; Abruna, H. D. *Proceedings – Electrochem. Soc.* **1997**, 97-17, 277.
23. Li, J.; Abruna, H. D. Book of Abstracts, 211th ACS National Meeting, New Orleans, LA, **March 1996**, 24-28, COLL.
24. Yee, R. J. C. E. L.; Guyer, K. L.; Tyma, P. D.; Weaver, M. J. *J. Amer. Chem. Soc.* **1998**, *101* 1131.
25. Radovic-Hrapovic Z.; Jerkiewicz, G. *J. Electroanal. Chem.* **2001**, *499*, 61.
26. Jerkiewicz, G.; Zolfaghari, A. *J. Phys. Chem.* **1996**, *100*, 8454.
27. Zolfaghari, A.; Jerkiewicz, G. *Proceedings – Electrochem. Soc.* **1997**, 97-16, 133.
28. Zolfaghari, A.; Jerkiewicz, G. *J. Electroanal. Chem.* **1997**, *422*, 1.
29. Zolfaghari, A.; Jerkiewicz, G. *J. Electroanal. Chem.* **1997**, *420*, 11.
30. Zolfaghari, A.; Jerkiewicz, G. *ACS Symposium Series* **1997**, *656*, 45.
31. Zolfaghari, A.; Jerkiewicz, G. *J. Electroanal. Chem.* **1997**, *467*, 77.
32. Dall'Antonia, G. T.-F. L. H.; Jerkiewicz, G. *J. Electroanal. Chem.* **2001**, *502*, 72.
33. Blais, G. J. S.; Herrero, E.; Feliu, J. M. *J. Electroanal. Chem.* **2002**, *519*, 111.
34. Labayen, E. H. M.; Feliu, J. B.; Harrington, D. A. *J. Electroanal. Chem.* **2000**, *488*, 32.
35. Radovic-Hrapovic, Z.; Jerkiewicz, G. Thin Films: Preparation, Characterization, Applications, [Proceedings of a Symposium of the American Chemical Society], San Diego, CA, United States, Apr. 1-5, 2001 (2002) 53.
36. Inukai, S. S. J.; Itaya, K. *J. Electroanal. Chem.* **1996**, *403*, 159.
37. Hubbard, A. T.; Stickney, J. L.; Rosasco, S. D.; Soriaga, M. P.; Song, D. J. *J. Electroanal. Chem. Interf. Electrochem.* **1983**, *150*, 165.
38. Shinotsuka, K. S. N.; Itaya, K. *Surf. Sci.* **1995**, *335*, 75.
39. Jones, A. W.-L. T. R. G. *Surf. Sci.* **1987**, *188*, 87.

40. Jones, D. L. P. R. G. *Vacuum* **1981**, *31*, 493.
41. Bowden, Y. J. K. P. A.; Hutchings, C. W.; Li, W.; Vidali, G. *Surf. Sci.* **1990**, *230*, 113.

CHAPTER 3

**STUDY OF POLYANILINE NANO-ELECTRODE ASSEMBLIES GROWN ON
DECANETHIOL/4-AMINOTHIOPHENOL MIXED MONOLAYERS**

3.1 Introduction

Self-assembled monolayers (SAMs) are highly ordered molecular assemblies that form spontaneously by chemisorption of functionalized molecules on surfaces, and organize themselves laterally; most commonly by van der Waals interactions between monomers.¹ Self-assembled monolayer of thiols on metal surfaces have attracted considerable scientific interest because of their capability of creating well-defined surfaces with controllable chemical functionality.² Thiol monolayer films have been used in electroanalytical chemistry for more than 20 years as the basis of electrochemical sensors. Sensors using SAM are widely used to monitor pH,³⁻⁵ inorganic species⁶⁻⁸ and, most frequently, organic or bio- molecules⁹⁻¹³ using both chemical and biological recognition elements.

The basis of a biosensor is the coupling of the biological sensing elements with a transducer. The biorecognition molecules are usually immobilized on to the surface of the transducer. It is required that the immobilization procedure must maintain the biorecognition molecule close to the transducer surface while retain its biological activity in a reproducible manner. Ideally, the immobilization layer should be robust and

applicable to different bio-molecules. SAMs provide a reproducible and robust method to immobilize biorecognition molecules. The biorecognition molecules can be immobilized to preformed SAMs via cross-linking with glutaraldehyde, non-covalent binding and direct covalent attachment to the SAM.⁹ Immobilization by cross-linking or non-covalent binding has the problems of irreproducibility or poor stability. Covalent attachment provides good reproducibility, stability and versatility. However, in this method, the biorecognition molecules usually need to be modified before the covalent attachment.

Conducting polymers, such as polyaniline, can potentially provide a method of immobilizing the biorecognition molecules to SAMs, which avoid the modification of the SAM or bio-molecules while retaining the good reproducibility and stability. Research of the conjugated polymers and SAMs has attracted a significant amount of interest during the past ten years. Conjugated polymers were selectively deposited on patterned thiol monolayers in which SAM was used as surface protective layer that resist the deposition of polymer. Monomers attached to the SAM were electropolymerized to form ultra-thin polymer films. Arrays of polymeric material in the size range of micrometers or nanometers were fabricated based on single-component or mixed thiol SAM.¹⁴⁻²¹

In this chapter, the two-component mixed self-assembled monolayers consisting of 4-aminothiophenol (4-ATP) and n-decanethiol (DT) were studied and the random arrays of polyaniline nano-/microelectrodes were fabricated based on mixed SAMs. The features of the polyaniline nano-/microelectrodes were characterized and compared with theoretical results. A biosensor using the SAM-based polyaniline electrodes were tested and the preliminary results were discussed.

It should be noted that the biosensor of SAM-polyaniline has the potential to increase sensitivity by reducing the nonspecific adsorption of protein through introducing molecules that resist the adsorption of protein, such as poly(ethylene glycol) (PEG) into the sensing surface.²² Ladd et al.²³ fabricated multichannel biosensors with DNA-directed protein immobilization. A mixed SAM with a PEG thiol molecules consist a nonfouling surface that resists the nonspecific protein adsorption, improving the performance of biosensors. The process of introducing PEG in the system is very simple and flexible by using the mixed SAMs.

3.2 Experimental Section

Chemicals. *4-Aminothiophenol (4-ATP) purification* 4-ATP was dissolved in water by adding sulfuric acid (1 N). The solution was decolorized by first adding activated charcoal followed by filtration to remove the charcoal. The remained solution was titrated with sodium hydroxide to a neutral pH. The organic phase was extracted with a small amount of dichloromethane. The light yellow solid 4-ATP was obtained by evaporating the dichloromethane and stored in the dark at 4 °C.

Aniline monomer (Fisher Scientific, Inc.) was distilled over zinc metal prior to use and stored in the dark at 4 °C in a nitrogen gas atmosphere. All other chemicals were reagent grade and used as received. Sodium chloride, magnesium chloride, sulfuric acid, hydrochloric acid and sodium hydroxide were purchased from Fisher Scientific, Inc.

Au microbead electrodes. Au wire (Gold wire 99.999%, 0.762 mm/0.030 inch in diameter, Alfa Aesar) was cleaned in deionized water, absolute ethanol, piranha solution (1:3 H₂O₂:H₂SO₄), deionized water and absolute ethanol sequentially. The gold

wire was then dried in a stream of dry Argon gas. The Au wire was melted in a H₂/O₂ flame and cooled in air in an up and down motion repeatedly until a gold ball with multiple facets formed at the end of the gold wire. The gold ball was annealed in a small hydrogen flame for 15 minutes prior to its use as a substrate for self-assembled monolayers.

Au foils Au foils (99.999%, purchased from Alfa Aesar) were cleaned in deionized water (1 min), absolute ethanol (1 min), piranha solution (30 min), deionized water (1 min) and absolute ethanol (1 min) sequentially.

Monolayer self-assembly Previously prepared and cleaned gold substrates were rinsed with ethanol, dried under nitrogen gas and then immersed for 24 hours in an ethanol solution containing a total thiol (one or two types of thiol molecules) concentration of 1mM. Upon emersion, the specimen was rinsed with copious amount of ethanol followed by a brief rinse with Millipore water. The Au electrode was then immediately placed in the electrochemical cell.

Covalent immobilization of immunoreagents Polyaniline films were made on the gold electrode using 0.1 M aniline monomer in 0.5 M H₂SO₄ aqueous solution. The electropolymerization of aniline was carried out by scanning potential from 0.0 V to 0.8 V (vs Ag/AgCl(sat)) for 25 cycles. The oxidized form was prepared by applying 600 mV to the polyaniline electrode for 3 minutes in 0.5 M sulfuric acid solution. The oxidized polyaniline-coated electrodes were cleaned by soaking them in deionized water three times for 3 minutes each to remove aniline and acid residue. In the sandwich immunoassay, the electrode with the oxidized polyaniline film was firstly soaked in 5 µg/mL anti-Rabbit IgG solution for 1 hour at room temperature and rinsed by buffer

solution of 0.135 M NaCl + 1% (v/v) Tween-20. Secondly, the modified electrode was soaked in 5 µg/mL antibody solution, and then in 5 µg/mL alkaline phosphatase labeled antibody for one half hour respectively. Once removed from the labeled antibody solution, the electrode was rinsed in distilled water. Finally, the substrate was transferred to a Teflon electrochemical cell containing 4 mM 4-aminophenyl phosphate in 0.1 M Tris buffer (pH 9.0) solution. The alkaline phosphatase label catalyzes the conversion of 4-aminophenyl phosphate to 4-aminophenol, which can be easily detected by cyclic voltammetry. Oxidative peak currents were recorded.

Electrochemistry All electrochemistry experiments were carried out using a BAS Epsilon Potentiostat workstation. A conventional three electrode configuration was employed and all cell components were constructed from either Teflon or Kel-F. In all cases, the gold electrode was the working electrode, a platinum net was the counter electrode, and Ag|AgCl(sat) was the reference electrode. When making electrochemical measurements, we made no attempt to mask the polycrystalline portions of the microbead electrodes. Therefore, all electrochemical behaviors obtained are corresponding to SAMs adsorbed on polycrystalline Au surfaces.

Total area of Au electrode Cyclic voltammograms of a clean Au electrode in a solution containing 1mM $K_3Fe(CN)_6$, and 100mM KNO_3 are recorded at a range of scanrates. The peak current was plotted against the square root of the scanrate. According to equation 3.1, the slope of the plot is $(2.69 \times 10^5)n^{3/2}AD_0^{1/2}C_0$ or $7.42 \times 10^{-4}A$ after substituting n , D_0 and C_0 with the corresponding value. Therefore, $A = slope/0.742$.

$$i_p = (2.69 \times 10^5)n^{3/2}AD_0^{1/2}C_0v^{1/2} \quad (3.1)$$

where i_p is the peak current in amperes, n is the number of electrons in the half redox reaction ($n = 1$ for $\text{Fe}(\text{CN})_6^{3-} / \text{Fe}(\text{CN})_6^{4-}$ redox couple), A is the total electrode area (cm^2), D_o is the diffusion coefficient of the analyte ($7.63 \times 10^{-6} \text{ cm}^2/\text{sec}$ for ferricyanide anion in 0.1 M KNO_3), C_o is the bulk concentration of $\text{K}_3\text{Fe}(\text{CN})_6$ and v is the scanning rate.

AFM imaging All AFM images were acquired using an Atomic Force Microscope Autoprobe CP from Park Scientific, and an Acquisition Module from Thermomicroscope. The imaging probes were ULNC-AUMT-AB mounted silicon cantilevers with spring constant 2.1 N/m (Digital Instruments). All images were acquired with a 100 μm Scanner Master with contact mode in air at room temperature. The images obtained were analyzed with PSI ProScan 1.5 data analysis software. The data obtained from AFM analysis were corrected with the method introduced in Dong's manuscript.²⁴

Curve Fitting The Non-linear curve fit program in the software Origin Pro 7.5 was used for curve fitting. The maximum number of iterations was set to 100.

3.3 Results and Discussion

3.3.1 Investigation of two-component mixed SAMs containing 4-ATP and DT

Electrical conductivity of the SAMs The electrical conductivity of alkyl thiol molecules was studied and it is commonly agreed that thiol molecule with long chain tail (number of carbon ≥ 12) are electrically non-conductive, while short-chain ones (number of carbon ≤ 8) are conductive. Here decanethiol (DT), whose number of carbon is in between, was chosen for study. The cyclic voltammograms shown in Figure 3.1 were

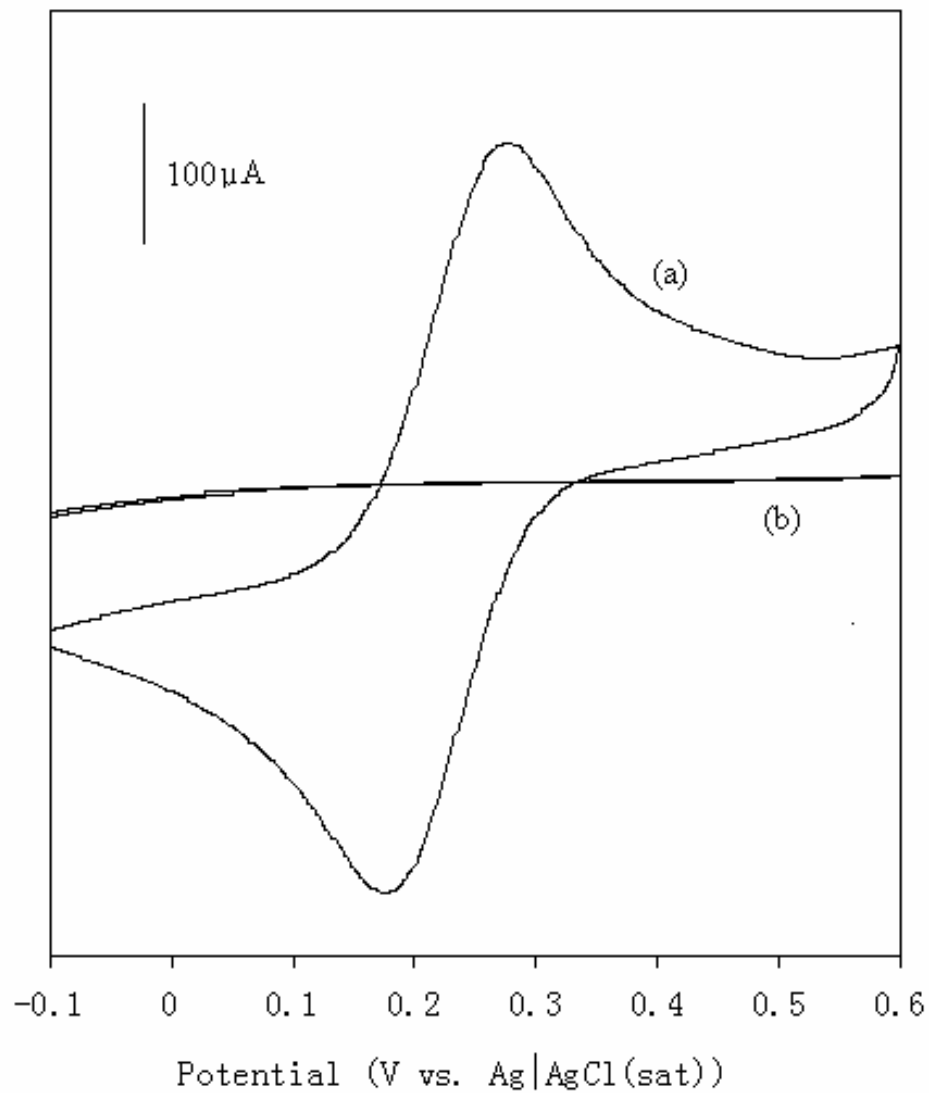


Figure 3.1. Voltammetric behavior of (a) 4-aminothiophenol (4-ATP) and (b) decanethiol (DT) single-component SAMs on Au in a solution containing 1 mM $\text{K}_3\text{Fe}(\text{CN})_6$ and 0.5 M Na_2SO_4 supporting electrolyte.

obtained from the electrodes prepared as described in the experimental section with pure 4-ATP or DT. The electrode potential was cycled between -100 mV and 600 mV at a scan rate of 100 mV s^{-1} in an aqueous electrolyte solution consisting of $1 \text{ mM K}_3\text{Fe}(\text{CN})_6$ and $0.5 \text{ M Na}_2\text{SO}_4$. In the Figure 3.1, the voltammogram shows no redox peak for the electrode modified with pure DT monolayer. This result indicates that monolayer self-assembled from DT solution forms an insulating layer which blocks the $\text{K}_3\text{Fe}(\text{CN})_6$ molecule from accessing the underlying gold electrode. In other words, the DT molecule is electrically non-conductive and the monolayer of pure DT on the gold substrate is highly ordered and the defect in the SAM is negligible. On the contrary, the cyclic voltammogram of the gold electrode covered with a pure 4-ATP monolayer showed reversible redox peaks that are similar to the ones displayed by bare gold electrodes. It is clear that electrons can be transported through the 4-ATP molecule.

Electroactivities of DT and ATP The cyclic voltammograms in Figure 3.2 were obtained from electrodes with pure 4-ATP or pure DT monolayers in 1 M HClO_4 solution. From the voltammograms, no redox reaction occurs for DT in the potential window from 0 V to 0.9 V . 4-ATP has an anodic peak at around 0.73 V and two cathodic peaks at around 0.3 V and 0.47 V . The anodic peak at 0.73 V was assigned to the one electron oxidation of 4-ATP to its cation radical. The cathodic peak at 0.47 V corresponds to reaction between 4-ATP cation radical with a neighboring 4-ATP molecule to form a dimer. The other cathodic peak at 0.3 V may be corresponding to the electrooxidation via an ECE mechanism which yields a desorbed product.

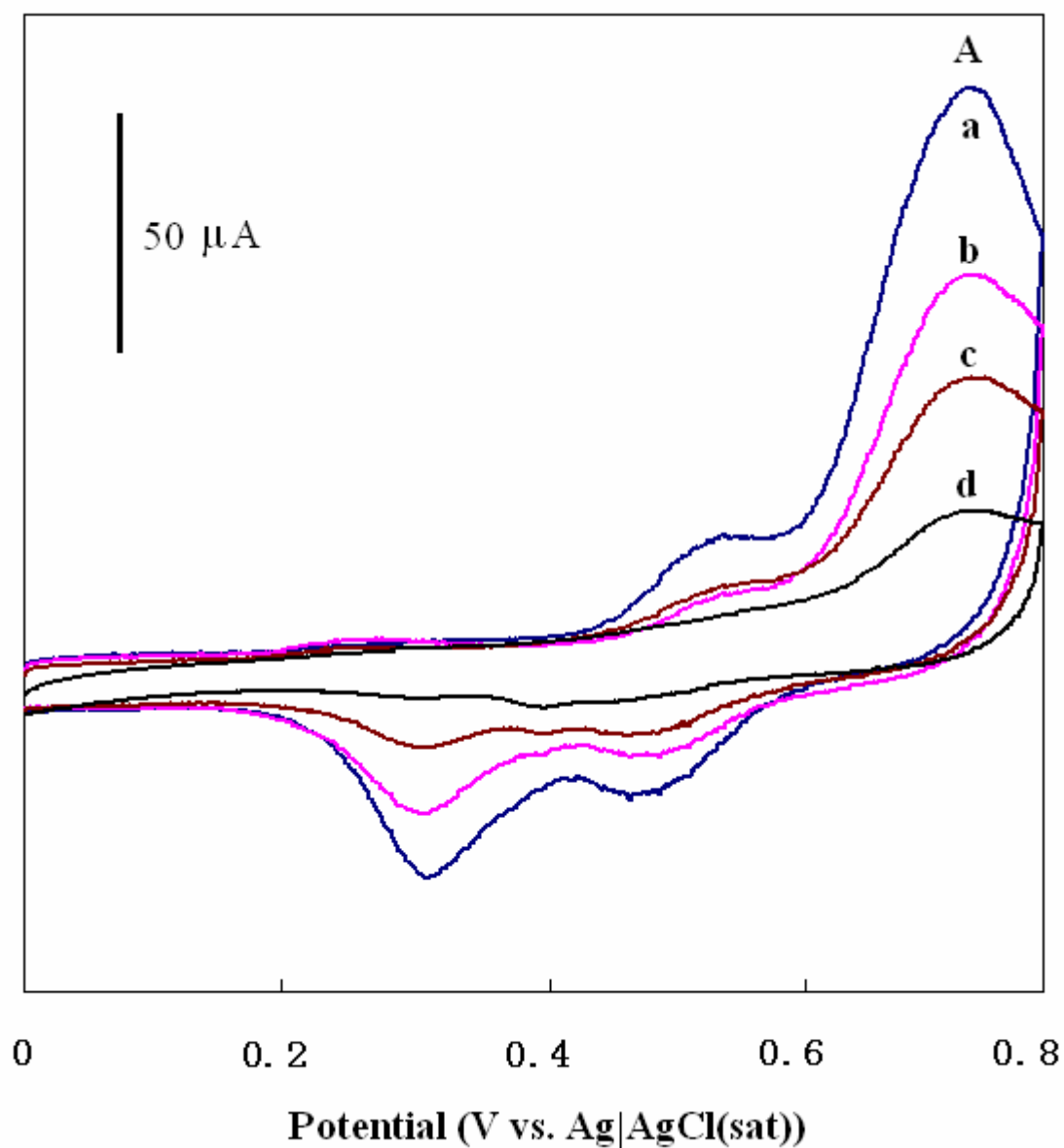


Figure 3.2. Voltammetric behavior of a 4-ATP/DT mixed monolayer on Au in a solution containing 100 mM HClO₄ electrolyte. The anodic wave (A) at 0.73V corresponds to the oxidation of 4-ATP to the cation radical. The mole fractions of 4-ATP in the assembling solution are (a) 1.0, (b) 0.9, (c) 0.8 and (d) 0.7.

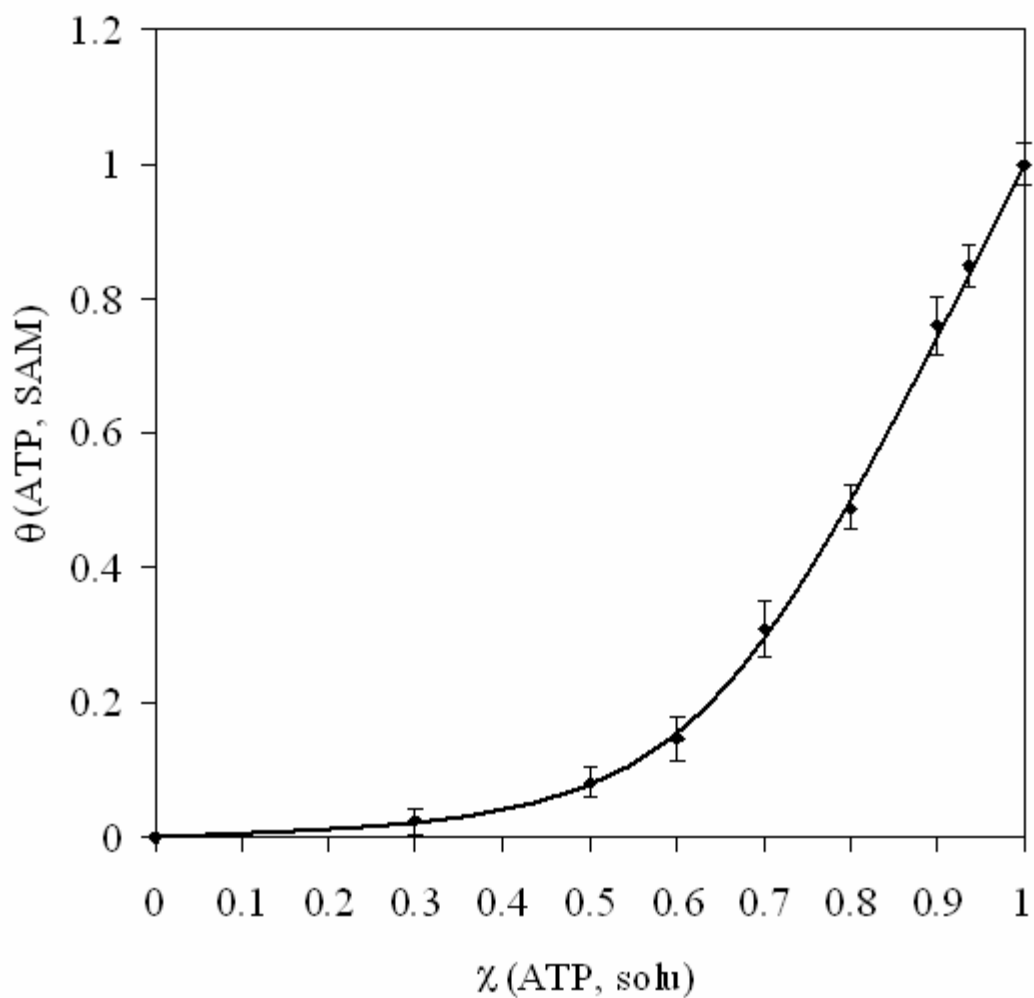


Figure 3.3. Plot of surface coverage of 4-aminothiophenol in mixed SAM as a function of the mole fraction of 4-aminothiophenol in solution, based on the anodic peak (at 0.73 V) height of 4-aminothiophenol (4-ATP) in a solution containing 100 mM HClO_4 .²⁵

The surface coverage of 4-ATP in mixed SAM For the single-component SAM of 4-ATP self-assembled from the 4-ATP solution for 24 hours, the surface coverage of 4-ATP is assigned to be one. Here defects enclosed by 4-ATP are counted in the surface coverage of 4-ATP.

The cyclic voltammograms in Figure 3.2 show that 4-ATP peak (at 0.73 V) current density vary according to the SAMs prepared from the assembling solution of different mole fraction of 4-ATP. The peak current density was used to calculate the surface coverage. Figure 3.3 is a plot of the surface coverage of 4-ATP in mixed SAM as a function of the mole fraction of 4-ATP in the assembling solution. The plot shows that the surface coverage of the 4-ATP in the mixed SAM is lower than the mole fraction of 4-ATP in the assembling solution. From Figure 3.3 we can see that the surface coverage of 4-ATP in mixed SAMs prepared from the assembling solution containing 0.5 mole fraction of 4-ATP is around 0.08 of that in pure 4-ATP SAM. The explanation for this result lies mostly in the differences in structures of 4-ATP and DT. The DT molecule has a long chain organic tail. The noncovalent lateral interactions among the organic chains make the molecules tend to form highly ordered monolayers, which are naturally stable. By contrast, the tail group of 4-ATP is much shorter and has less noncovalent lateral interactions. The large benzene ring in the 4-ATP molecule is likely to form defects in the SAMs. In addition, the amino group of 4-ATP increases the molecule affinity for ethanol and increase its solubility in the solvent. This combination of factors makes the process of assembling 4-ATP molecules, from solution to the gold, a relatively slow process compared to DT.

If the mole fraction of 4-ATP in solution is below 0.6, the surface coverage of 4-ATP in SAM increases slowly relative to the mole fraction of 4-ATP in solution. When the mole fraction of 4-ATP in solution exceeds 0.6, the surface coverage of 4-ATP in SAM increase rapidly as the mole fraction of 4-ATP in solution increase. Precisely controlling of surface coverage of 4-ATP in SAM becomes difficult.

The surface coverage of DT in mixed SAM The surface coverage of DT in mixed SAM was measured individually. The electrode modified with mixed SAM was immersed in an aqueous solution containing 1mM $K_3Fe(CN)_6$ and 0.5 M Na_2SO_4 and cycled between -100 mV and 600 mV at a scan rate of 100 $mV s^{-1}$. The cyclic voltammograms of the electrodes modified with various mixed SAMs are shown in Figure 3.4. The peak current was measured and recorded as current density after being divided by the surface area of electrode (which is obtained experimentally). The decrease of the peak current density is proportional to the surface coverage of DT.

The total surface coverage of DT in a mixed SAM is calculated by comparing the decrease of the peak current density of mixed SAM to that of pure 4-ATP SAM. That is,

$$\text{surface coverage of DT} = \frac{i_{\text{pure 4-ATP}} - i_{\text{mixed SAM}}}{i_{\text{pure 4-ATP}}}, \text{ where } i \text{ is the current density.}$$

Figure 3.6 shows a plot of surface coverage of decanethiol in the mixed SAM as a function of the mole fraction of the decanethiol in the assembling solution. The surface coverage of decanethiol in the mixed SAM on gold ($\theta(\text{DT}, \text{SAM})$) increased quickly as the mole fraction of decanethiol in assembling solution ($\chi(\text{DT}, \text{solu})$) increased, when the $\chi(\text{DT}, \text{solu})$ was lower than 0.5. When $\chi(\text{DT}, \text{solu})$ was between 0.5 and 0.7, the increasing rate of the surface coverage of decanethiol in the mixed SAM slowed down.

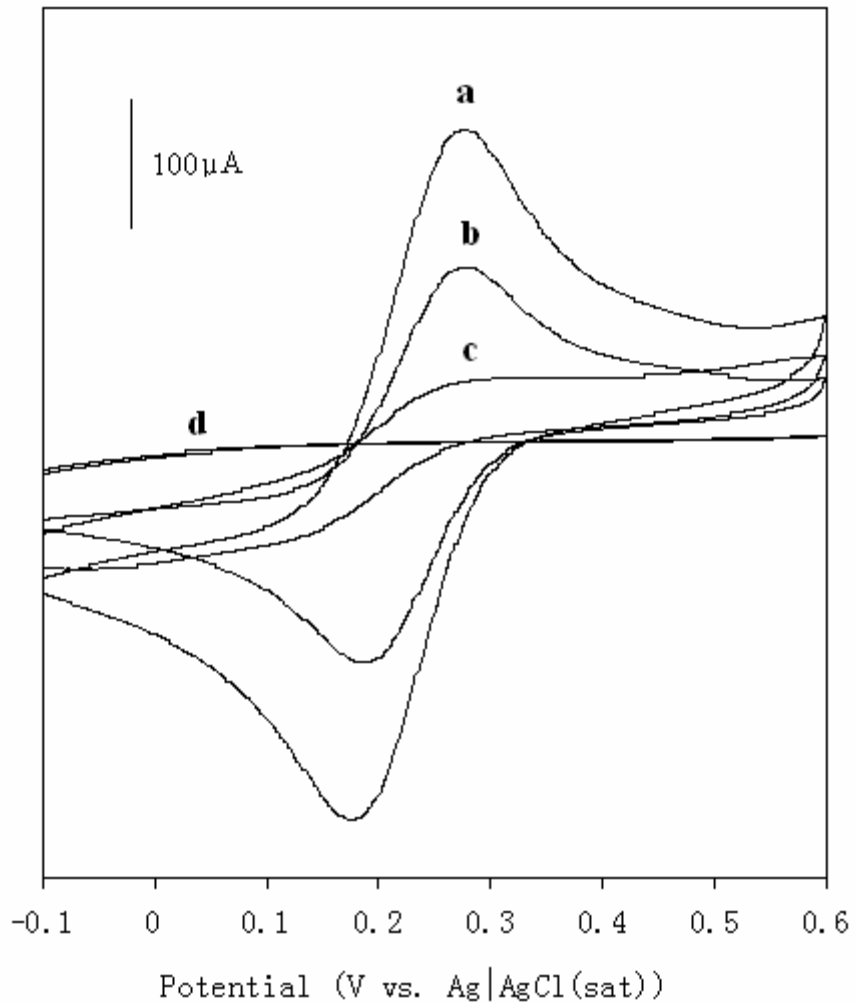


Figure 3.4. Voltammetric behavior of the mixed SAMs on Au in a solution containing 1 mM $K_3Fe(CN)_6$ and 0.5 M Na_2SO_4 supporting electrolyte. The mole fractions of decanethiol (DT) in the assembling solutions were (a) 0.0, (b) 0.5, (c) 0.67, and (d) 1.0.

When $\chi(\text{DT, solu})$ exceeded 0.7, more than 90 percent of the gold surface was covered by decanethiol and the surface coverage of decanethiol in the mixed SAM increased very slowly.

The surface coverage of decanethiol was re-plotted as a function of the mole fraction of 4-aminothiophenol in the assembling solution and was shown in Figure 3.6 as curve (b). The curve (a) in Figure 3.6 is the surface coverage of 4-aminothiophenol. By comparing the surface coverage of 4-aminothiophenol ($\theta(4\text{-ATP, SAM})$) to that of decanethiol at mole fraction of 4-aminothiophenol in solution of 0.5, it was found that $\theta(4\text{-ATP, SAM})$ is around ten times as large as $\theta(\text{DT, SAM})$, indicating that decanethiol could adsorb more strongly on the gold surface than 4-aminothiophenol under our experimental condition. This may be due to the difference tail chains of the two thiol molecules. The strong interaction between the long carbon chains of the decanethiol molecules on the gold surface enable the adsorbed decanethiol molecules to form a highly ordered monolayer which is stable on the gold surface.²⁶ Comparing to decanethiol, the 4-aminothiophenol has a much shorter chain. It is likely the 4-aminothiophenol monolayer is less stable than decanethiol monolayer on gold surface. In Figure 3.6, after the mole fraction of 4-aminothiophenol in solution exceeded 0.5, as the mole fraction of 4-aminothiophenol increased, $\theta(4\text{-ATP, SAM})$ increased and $\theta(\text{DT, SAM})$ decreased quickly. The two curves meet at mole fraction of 4-aminothiophenol in solution of 0.75, indicating that both 4-aminothiophenol and decanethiol have the surface coverage in the mixed SAM.

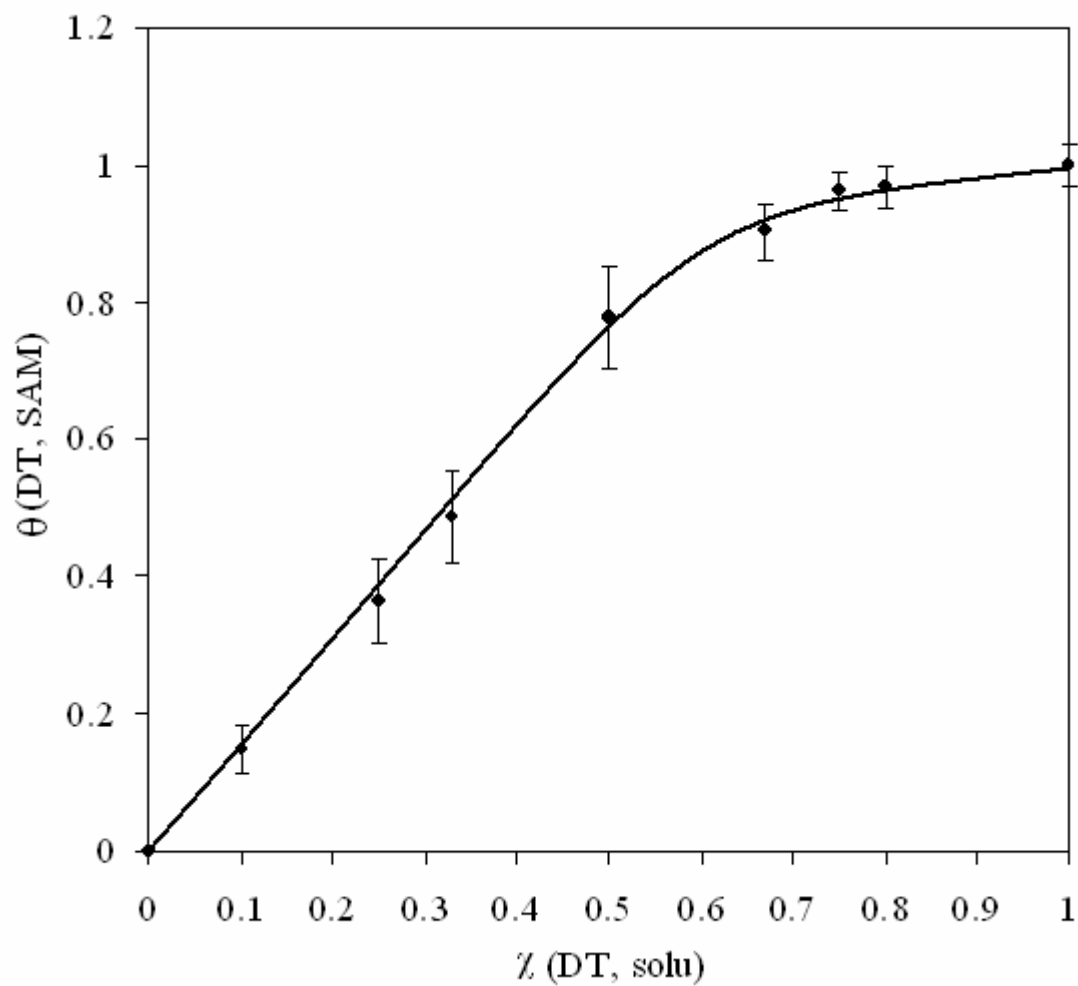


Figure 3.5. Plot of surface coverage of decanethiol in mixed SAM as a function of the mole fraction of decanethiol in solution.

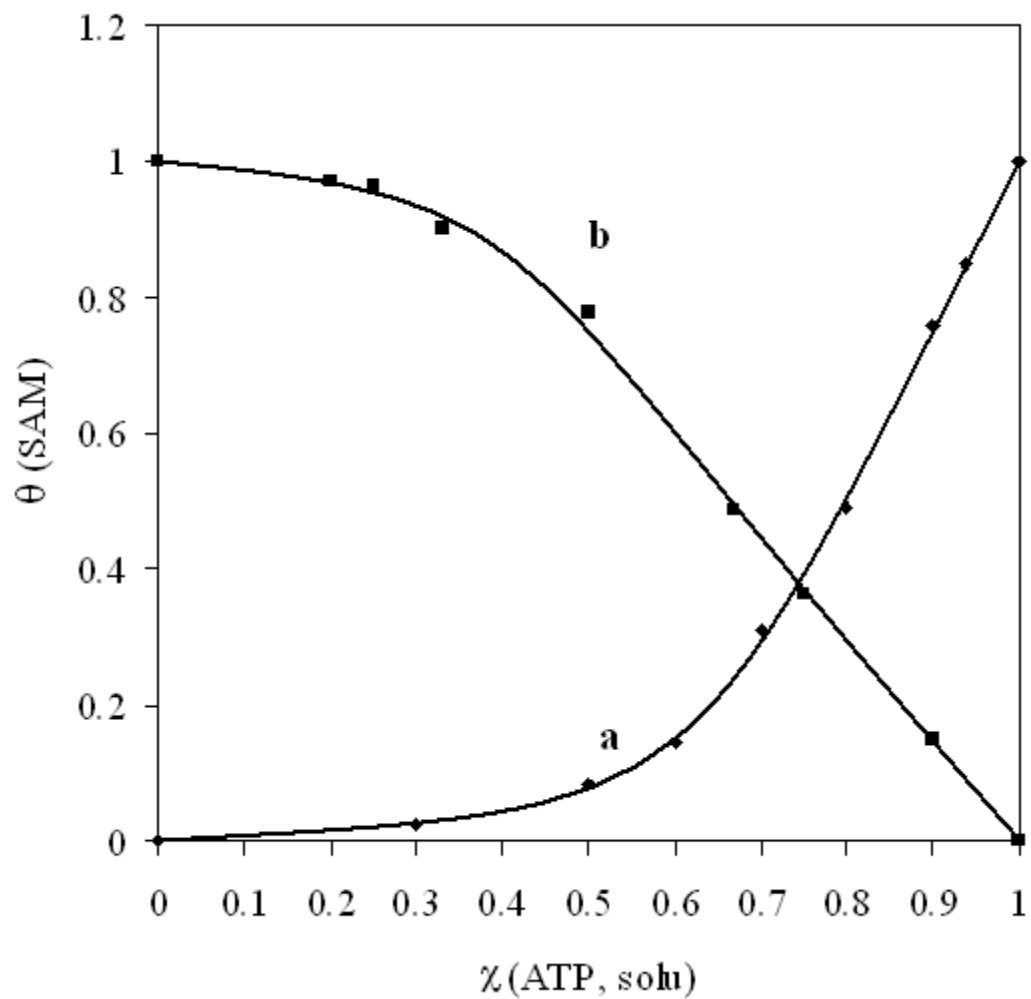


Figure 3.6. Plots of (a) \blacklozenge surface coverage of 4-ATP, (b) \blacksquare surface coverage of DT as the functions of the mole fraction of 4-aminothiophenol in solution.

3.3.2 Fabrication of polyaniline nanoelectrode ensemble through the electropolymerization of aniline on 4-ATP/DT surfaces

The electropolymerization of aniline on bare gold or mixed SAM was studied previously.^{20,23} On a bare Au, aniline was oxidized to the aniline cation radical at a potential of 0.97 V versus Ag|AgCl(sat) in an aqueous solution containing 100mM aniline and 100mM HClO₄. The polymerization of aniline at Au was carried out by potential cycling between a lower limit of 0.0V and an upper limit of 1.0 V versus Ag|AgCl(sat) at a scan rate of 0.100 V/s. After scanning the potential between 0.0 and 1.0 V for 25 cycles, a black film formed on the surface of the Au electrode. It was found that no polymer was deposited on bare gold electrodes by potential cycling when the upper potential limit was less than 0.9V.

Single-component monolayers of 4-aminothiophenol (4-ATP) and decanethiol (DT), and two-component mixed monolayers (4-ATP + DT) on Au electrodes were used as platforms for the electropolymerization of aniline. The voltammetric response of a 4-ATP SAM-modified Au electrode in 100mM HClO₄ supporting electrolyte and 100mM aniline is shown in Fig. 3.7. In this experiment, the scan was initiated at a potential of 0.0V, swept positive to an upper limit of 1.0V, and then swept cathodically back to 0.0V at a scan rate of 0.1 V/s. Two irreversible oxidation waves, labeled A'1 and A'2, were observed in this voltammogram. As discussed previously, the wave at 0.97V(A'2) corresponded to the irreversible oxidation of aniline, while the smaller wave at 0.73V (A'1) was assigned, on the basis of our previously results, as the oxidation of adsorbed 4-ATP to the 4-ATP cation radical. Potential cycling was used to electrodeposit polyaniline

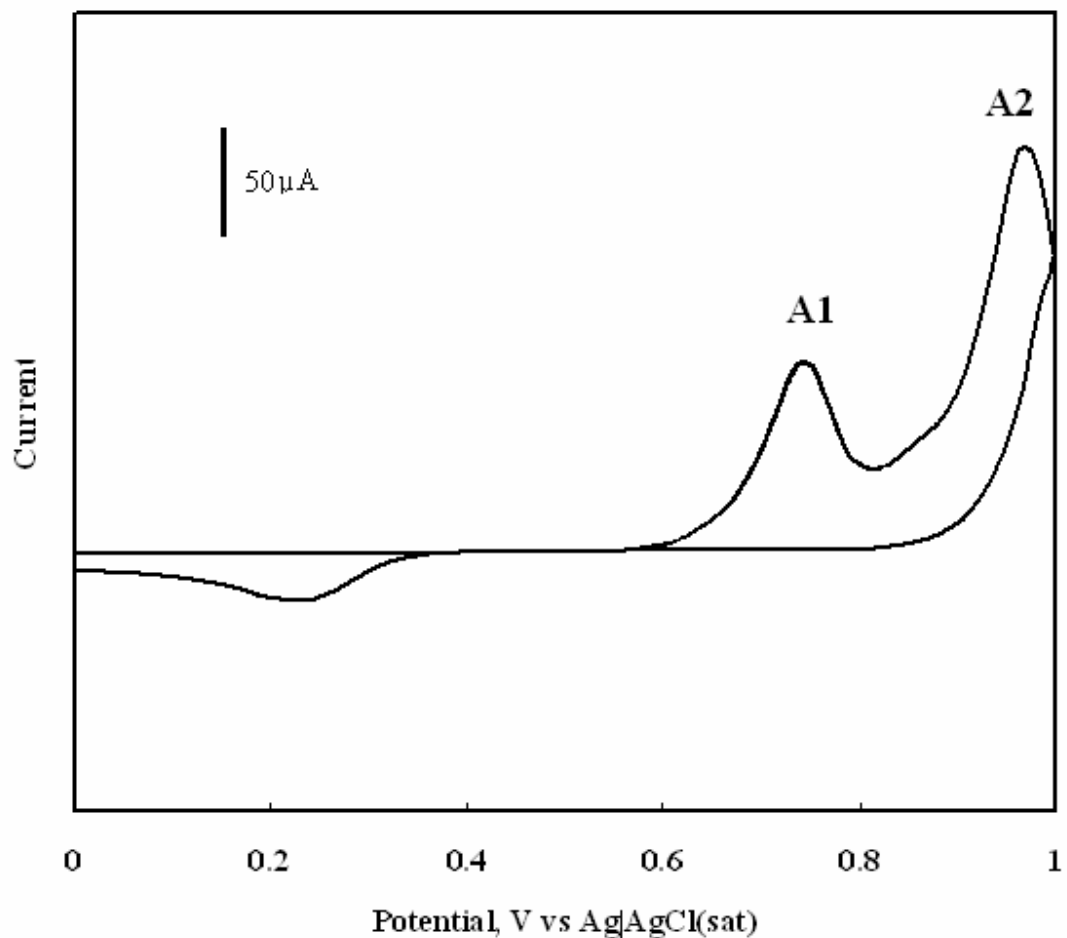


Figure 3.7 Voltammetric behavior of a 4-aminothiophenol (4-ATP) monolayer on Au immersed in a solution containing 100mM aniline and 100mM HClO₄ supporting electrolyte. The anodic wave at 0.97 V corresponds to the oxidation of solution phase aniline to the aniline cation radical. The smaller wave at 0.73V is assigned as the one electron oxidation of 4-ATP to its cation radical.

films on to SAM-modified Au electrodes from solutions that were 100mM in both HClO₄ and aniline. In these experiments, the switching potential was more positive than the oxidation potential of 4-ATP (0.73 V), but negative of the oxidation potential of aniline itself (0.97 V). After 25 cycles, polyaniline films were observed (by visual inspection) forming only in the case of SAMs in which $\Gamma(4\text{-ATP, SAM}) > 0.33$. The cyclic voltammetry experiment in 100mM HClO₄ electrolyte also proved the presence of polyaniline on the mixed SAM.

As mentioned previously, there was no polymer formation observed on bare Au electrodes when the switching potential was less than 1.0V. When results were combined, a conclusion could be reached that the growth of polyaniline was initiated from 4-ATP cation radicals on the modified electrode surface.

3.3.3 AFM characterization of aniline nanoelectrode arrays

AFM analysis was used to visualize polyaniline grown on the surface of the mixed SAM. The mixed SAM of DT/4-ATP was self-assembled on to the Au(111) surface and then polyaniline was electropolymerized on to the mixed SAM. The SAM-based on a mixed SAM containing DT and 4-ATP (surface coverages of 4-ATP is 0.0834 and polyaniline electrode ensemble prepared on Au(111) was then scanned by AFM with contact mode. Figure 3.8 and 3.9 represent the contact mode AFM images of polyaniline (0.3600 respectively). By comparing AFM images before and after depositing polyaniline, one can easily conclude that the high spots shown in Figure 3.8 are the polyaniline electropolymerized on 4-ATP. The randomly distributed polyaniline electrodes have a

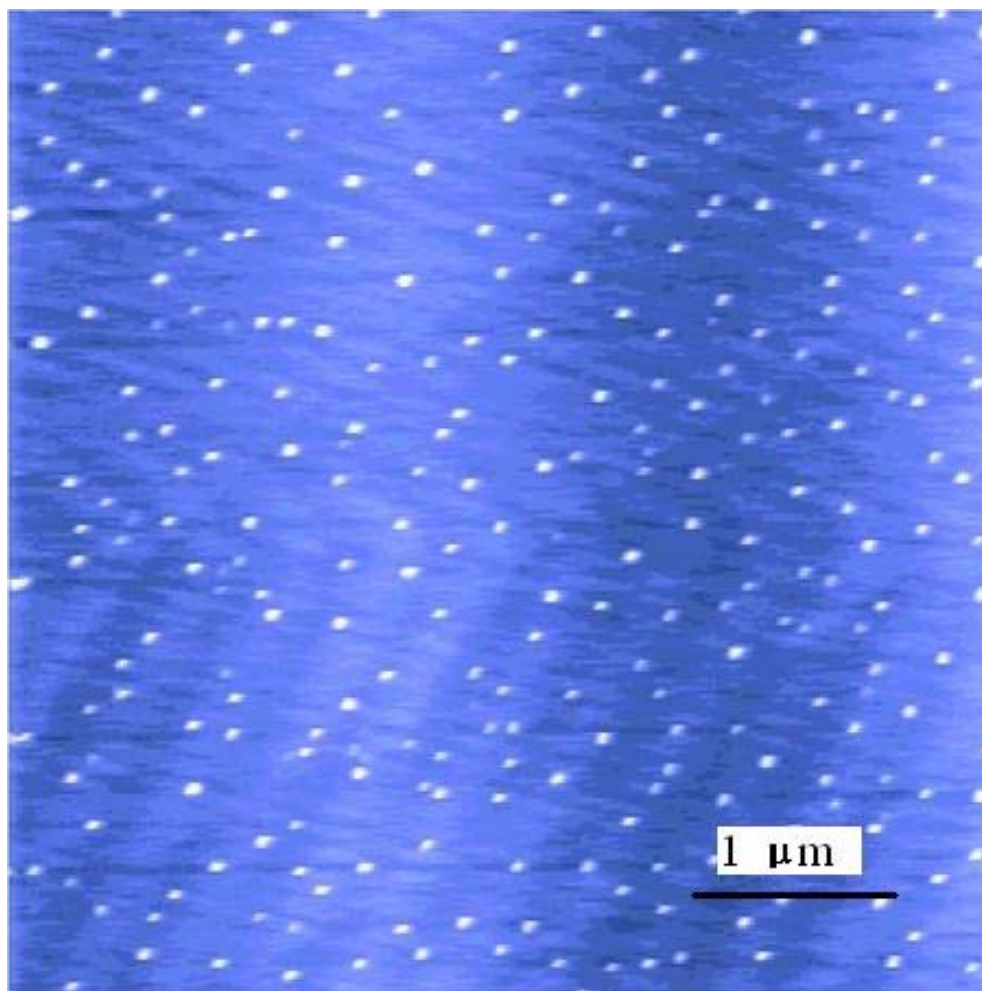


Figure 3.8. AFM image of polyaniline nanoelectrode assemble. The mole fraction of 4-ATP in assembling solution is 0.4. The surface coverages of 4-ATP is 0.0834. The scale bar = 1 μm .

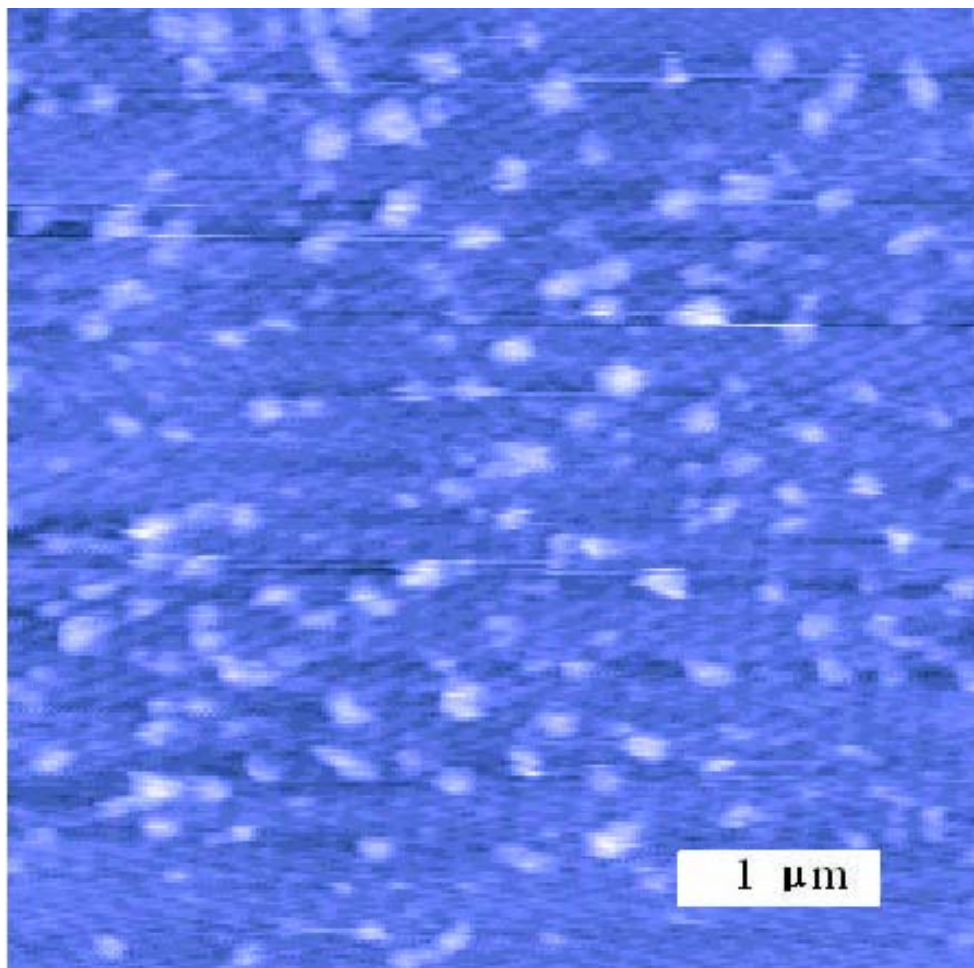


Figure 3.9. AFM image of polyaniline nanoelectrode assemble. The mole fraction of 4-ATP in assembling solution is 0.7. The surface coverages of 4-ATP is 0.3600. The scale bar = 1 μm .

rather narrow size distribution when the mole fraction of 4-ATP in the assembling solution was low. When the mole fraction of 4-ATP in the assembling solution increased, the size distribution broadened. Considering that the contact mode AFM overestimates the lateral dimension when the feature size is comparable to the tip size, a correction was made to the size value of polyaniline electrodes.

The obtained number density and the average radius of the polyaniline electrodes are shown in Table 3.1. From Table 3.1, we can see that as the 4-ATP mole fraction in solution increase from 0.4 to 0.7, the average radius of the polyaniline electrodes increase around 150% and the number density increase around 100%.

Table 3.1. Number density and average radius of polyaniline electrodes on 4-ATP from AFM analysis.

4-ATP mole fraction in solution	Number density, $\times 10^8 \text{ cm}^{-2}$	Radius, nm
0.4	8 ± 1	53 ± 5
0.5	10 ± 2	78 ± 8
0.6	13 ± 2	95 ± 14
0.7	16 ± 3	128 ± 23

3.3.4 Theoretical simulation for polyaniline electrode arrays

Theoretical studies of ordered arrays of ultramicroelectrodes are extensive.³⁰⁻³⁷ However, the theory for random array is very limited. In 1988, Scharifker³⁸ developed an analytical solution of the time-dependent diffusion current to random arrays of ultramicroelectrodes based on the overlap of circular diffusion zones. The statistical

overlap of diffusion zones arising from a uniform distribution of microelectrodes was treated through the Avrami-Kolmogorov theorem.³⁹⁻⁴¹ In this section, the Scharifker's theory will be applied for obtaining the theoretical value of n and r_0 for the polyaniline electrode ensembles. A brief overview of the theory is given here. Details refer to Scharifker's paper.³⁸

In the theory, an adimensional time³⁸ was defined as

$$u = n r_0 (\pi D t)^{1/2} \quad (3.1)$$

where n is the number density of microelectrodes, r_0 is the radius of microelectrode, D is the diffusion coefficient.

After the treatments with the Avrami-Kolmogorov theorem, the current density to the ensemble of electrodes was obtained as

$$I / \pi n r_0 z F D c = 1 / \pi u \{1 - \exp[-\pi(u + n r_0^2)]\} \quad (3.2)$$

By substituting equation 3.1 into equation 3.2, equation 3.3 was achieved after several simple mathematic steps.

$$I = z F D c \{1 - \exp[-n \pi r_0 (\sqrt{\pi D t} + r_0)]\} / \sqrt{\pi D t} \quad (3.3)$$

To obtain theoretical values of n and r_0 , the plot of I as a function of $t^{-1/2}$ must be obtained through experiment. The chronoamperometric experiments was carried out at 600 mV in the solution containing 1 mM $K_4Fe(CN)_6$ and 0.5 M Na_2SO_4 , for the ensembles of polyaniline grown on the mixed SAMs with different surface coverage of 4-ATP. The raw chronoamperometric data was processed to obtain the values of current density, I and $t^{-1/2}$. The current density, I , was plotted versus $t^{-1/2}$ as the scatter charts shown in the Figure 3.10.

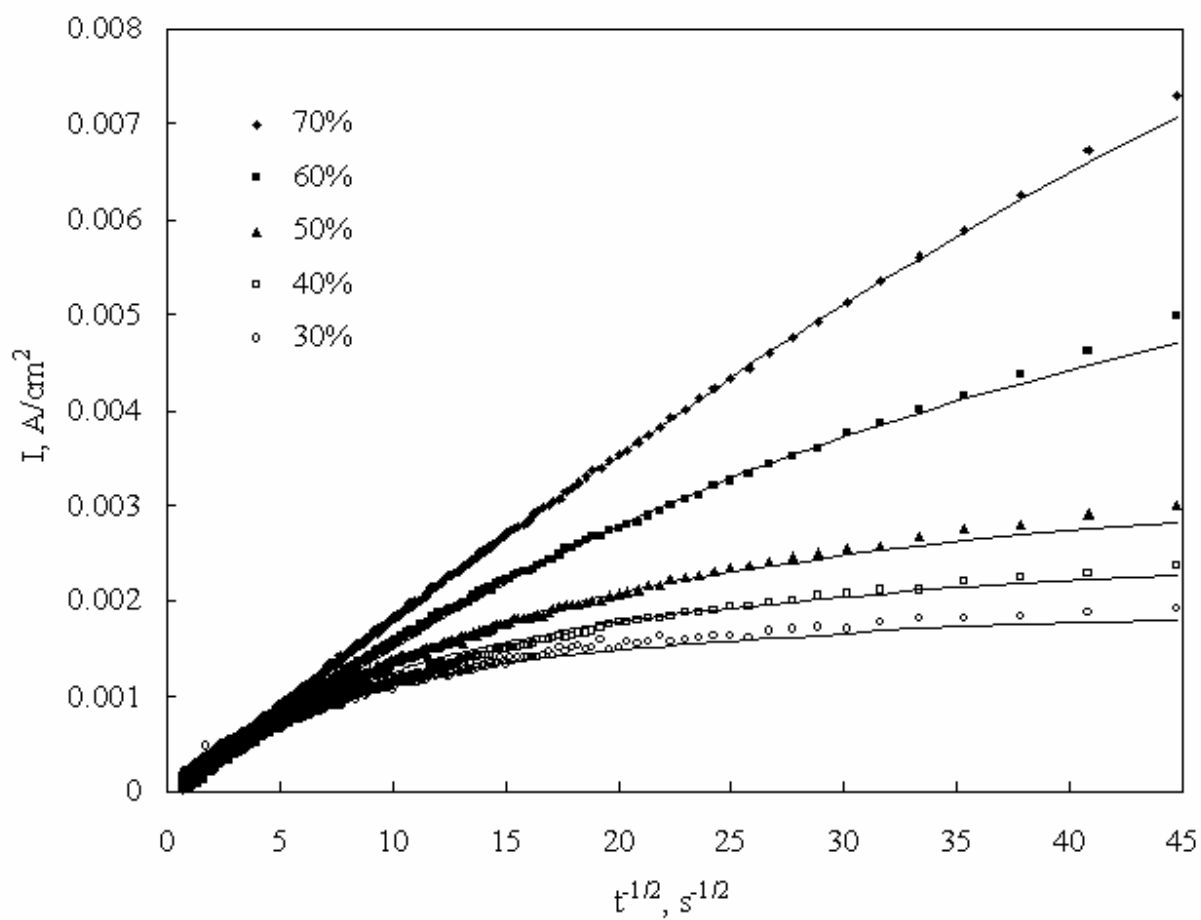


Figure 3.10. Plots of I vs $t^{-1/2}$ obtained by chronoamperometry with polyaniline nanoelectrode arrays with surface coverages of 4-ATP of 0.360, 0.136, 0.0834, 0.0424, 0.0230. Solid curves are the theoretical ones.

Table 3.2. The number density and radius of polyaniline electrodes from fitting results and from AFM measurement.

4-ATP mole fraction in solution	n from fitting, $\times 10^8 \text{ cm}^{-2}$	r_0 from fitting, nm	n from AFM, $\times 10^8 \text{ cm}^{-2}$	r_0 from AFM, nm
0.3	2.43	56	N/A	N/A
0.4	2.84	64	8 ± 1	53 ± 5
0.5	3.26	86	10 ± 2	78 ± 8
0.6	4.42	102	13 ± 2	95 ± 14
0.7	4.85	148	16 ± 3	128 ± 23

The “nonlinear curve fit” program in the software “Origin Pro 7.5” was used to obtain the theoretical values of n and r_0 . The function used is expressed in the Equation 3.3. The values of n and r_0 achieved from AFM analysis were used as the initial values of n and r_0 for nonlinear curve fit. The maximum number of iterations is set to 100. The fitting plots are shown in Figure 3.10 as the solid curve. We can see that after 100 iterations, the fitting curve agrees very well with the experimental curve.

From Figure 3.10, several conclusions were made: (1) all curves approach to origin at long time ($t^{1/2} < 5$), (2) for long time range ($t^{1/2} < 5$), all curves have the same slope which corresponds to the Cottrell equation for the electrode surface area of 1 cm^2 , (3) for short time range ($t^{1/2} \geq 5$), the curves of the electrodes covered with SAMs of low 4-ATP surface coverage (e.g. < 0.1) bend right, showing the characteristic of microelectrode array. As the surface coverage of 4-ATP increases (e.g. > 0.3), the curve of I versus $t^{1/2}$ get close to the Cottrell line, showing the characteristics of macroelectrode.

The fitting results of n and r_0 are shown in Table 3.2. The radius polyaniline electrodes obtained from the fitting are slightly larger than those measured by AFM. The reason may be in several aspects. First, the electrodes considered in theory are in-laid electrodes, while the polyaniline electrodes were three-dimension electrodes and the geometric surface of the polyaniline electrode was not smooth. Thus, the surface area of the polyaniline electrode was much larger than the smooth inlaid electrode. Second, in mixed SAM, some of 4-ATP molecules form large “islands”, on which polyaniline grown could be detected by AFM as is shown in Figure 3.8. While, there are individually distributed 4-ATP molecules, which may be under the detection limit of the AFM. There are also some defects present in the mixed SAM. These individual 4-ATP molecules and the defects make the diffusion zones overlap earlier than expected. Thus, the size and the density of polyaniline electrodes were overestimated and the average distance between two close electrodes was underestimated.

Table 3.3. Surface coverage of polyaniline electrodes or surface coverage of 4-aminothiophenol (4-ATP)

4-ATP mole fraction in solution	surface coverage of polyaniline from fitting	surface coverage of 4-ATP from Figure 3.3
0.3	0.0235	0.0230
0.4	0.0367	0.0425
0.5	0.0760	0.0834
0.6	0.144	0.176
0.7	0.333	0.360

The number densities measured from AFM are around three times as large as those obtained from fitting. The reason may be that area scanned by AFM was limited and that images selected for measurement usually had higher number density than the average number density of whole Au electrode, since those areas that contain rarely or no polyaniline electrode were not scanned.

Table 3.3 shows three sets of surface coverages of 4-aminothiophenol in the mixed SAMs which were obtained respectively from curve fitting, electrochemical measurement and AFM measurement. It is interesting that the surface coverage of polyaniline calculated from the fitting matches well with the surface coverage of 4-ATP measured from Figure 3.3.

3.3.5 Study the binding between polyaniline and protein

The interactions between polyaniline and the proteins immobilized on polyaniline were usually viewed as electrostatic force.⁴² Han and Jeng⁴³ found that reduction and substitution events were concurrent when polyaniline emeraldine base was immersed in the solution containing nucleophiles such as amine and thiol. Since the proteins contain abundant electron-donating amino or thio groups, the covalent bonds between polyaniline and the attached proteins are expected.

Here, we were interested in how fast the reactions between polyaniline and nucleophiles (amine and alkanethiol) are in mild conditions. The polymerization of polyaniline was carried out by potential cycling between 0.0 and 0.8 V versus Ag|AgCl(sat) for 25 cycles in a solution containing 100mM aniline and 0.5 M H₂SO₄. Polyaniline was oxidized in a 0.5M sulfuric acid solution at 600 mV for 3 minutes. The

polyaniline electrode was immersed in an ethanol solution containing 1mM decanethiol or glycine for a time and rinsed with copious amounts of distilled water upon emersion.

The polyaniline electrode was scanned between -350 mV and 50 mV in an solution containing 1 mM $\text{Ru}(\text{NH}_3)_6\text{Cl}_3$ and 0.5 M NaNO_3 , before and after immersion in the amine or alkanethiol solution. In Figure 3.11, the cyclic voltammograms of $\text{Ru}(\text{NH}_3)_6\text{Cl}_3$ show that the polyaniline emeraldine base had good conductivity before being immersed in the decanethiol solution. After being immersed in the decanethiol solution for 5 minutes, the emeraldine base was reduced by decanethiol and formed leucoemeraldine base which is a nonconductive product. Figure 3.12 shows the voltammetric behavior of $\text{Ru}(\text{NH}_3)_6\text{Cl}_3$ on oxidized polyaniline before and after reacting it with amine. The peak height decreases slightly after polyaniline being immersed with amine for 5 minutes and significantly after polyaniline was immersed with amine for 30 minutes. This means that the reduction of polyaniline happened at a slower rate in the amine solution than in the decanethiol solution. This result agrees with Han and Jeng's conclusion that alkanethiols react with emeraldine base at a much higher rate than amines.⁴¹

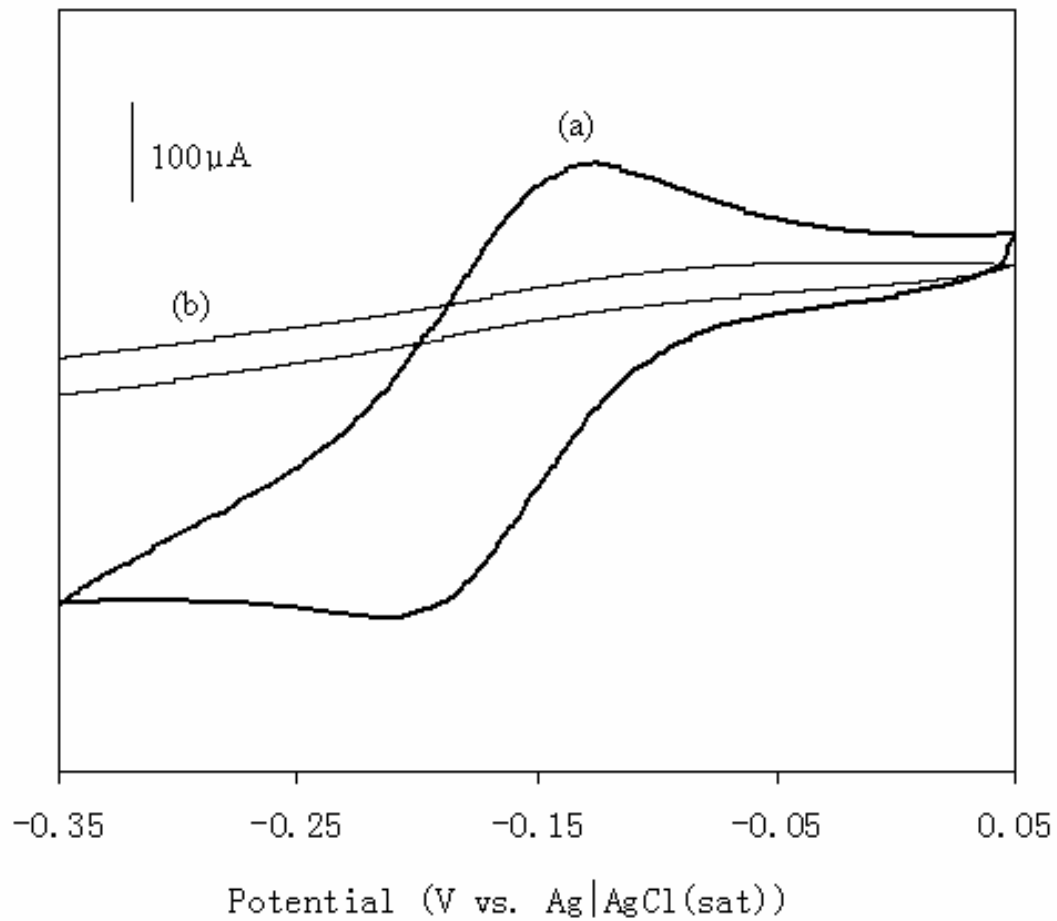


Figure 3.11 . Voltammetric behavior of $\text{Ru}(\text{NH}_3)_6\text{Cl}_3$ on oxidized polyaniline (a) before and (b) after reacting with decanethiol.

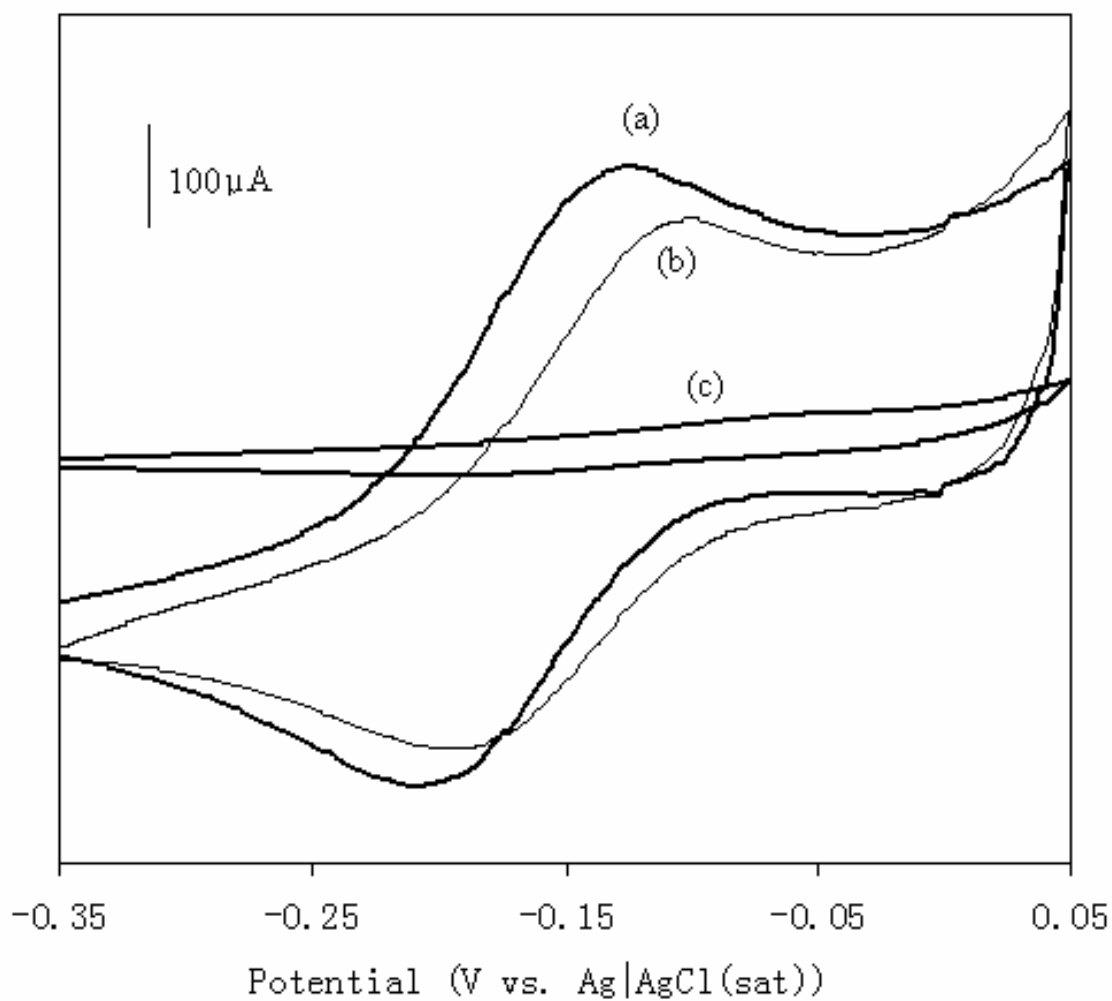


Figure 3.12. Voltammetric behavior of $\text{Ru}(\text{NH}_3)_6\text{Cl}_3$ on oxidized polyaniline (a) no reaction, (b) after reacting with glycine for 5 min, and (c) after reacting with glycine for 30 min

3.3.6. Investigation the efficiency of protein immobilization on SAM-polyaniline electrodes

Because of their low double-layer capacity, nanoelectrodes may have dramatically improved detection limits. In addition, the sensors using the nanoelectrodes can have very short response time.⁴⁴ Myler et al. reported biosensors using alcohol oxidase enzyme micro-electrode array. The electrodes were prepared by first depositing an insulating polydiaminobenzene film on gold electrode, followed by the sonication and ablation to obtain exposed discrete areas of the underlying gold electrode which act as the microelectrodes. Then aniline/biomolecules (e.g. glucose oxidase) was polymerized on the exposed gold areas. The enzymatic sensors developed include ethanol, oxalate, DNA hybridization and affinity antibody/antigen based sensors. Due to the hemispherical diffusional profiles, the enhanced sensitivities and lower detection limits are likely to be achieved. In this work, nanoelectrode array was fabricated by selectively depositing polyaniline on the 4-aminothiophenol. Comparing to Myler's work, the SAM-based electrodes have at least two advantages: first, fabrication of SAM-based electrodes is simpler and less expensive, because the preparation SAM is a simple one-step procedure; second, the size of SAM-based electrodes can be tuned to the nano-scale. As the size of electrodes decrease, the improved sensitivities and detection limits would likely to be achieved, according to the properties of microelectrodes.⁴⁵

Figure 3.13 is a plot of polyaniline peak current as a function of the mole fraction of 4-aminothiophenol in mixed SAM. As shown in Figure 3.12, the amount of polyaniline grown on mixed SAM was linearly proportional to the mole fraction of 4-ATP in mixed SAM. The labeled anti-rabbit IgG were immobilized on the oxidized

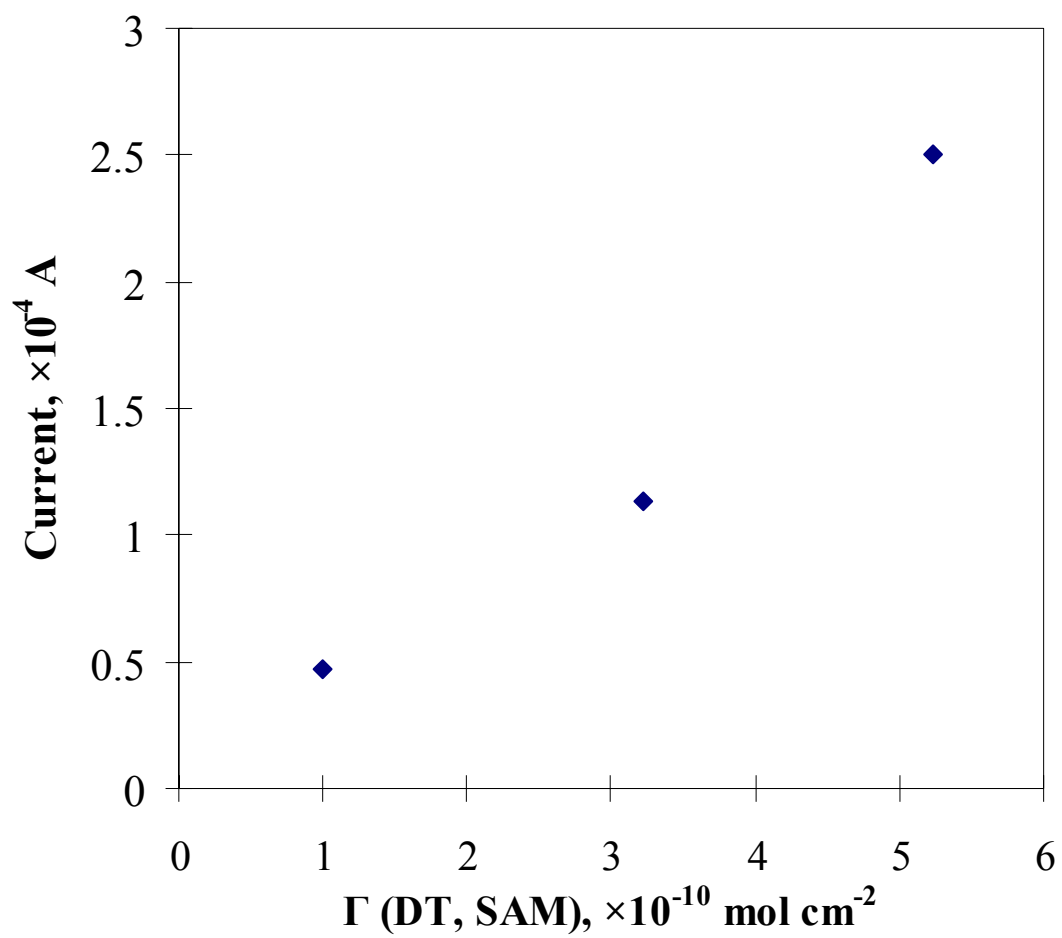


Figure 3.13. Plot of polyaniline peak current as a function of the mole fraction of 4-aminothiophenol in mixed SAM.

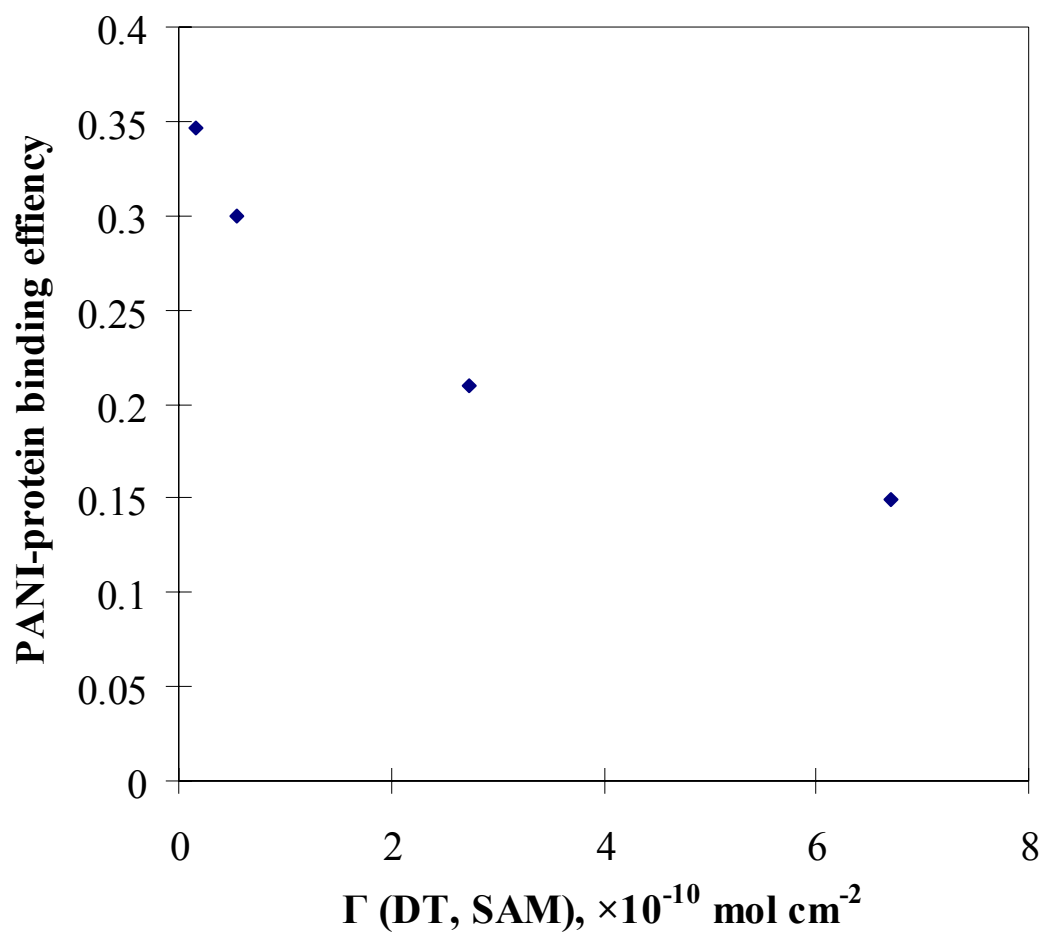


Figure 3.14. Plot of protein-polyaniline binding efficiency as a function of the mole fraction of 4-aminothiophenol in mixed SAM.

polyaniline. Figure 3.13 is a plot of protein-polyaniline binding efficiency as a function of the mole fraction of 4-aminothiophenol in mixed SAM. The protein-polyaniline binding efficiency was calculated by dividing the normalized (at pure 4-ATP) protein signal to the mole fraction of 4-ATP in mixed SAM. From Figure 3.14, one can conclude that the protein-polyaniline binding efficiency increased as the mole fraction of 4-ATP in mixed SAM decreased.

3.4 Conclusions

The selective deposition of polyaniline on mixed SAM of 4-ATP/DT is a promising approach for developing biosensors, in which the immobilization of biosensing molecules become simple.

The comparison of electropolymerization of aniline on bare gold electrode and ATP-modified gold electrode disclosed that aniline electropolymerization happened on ATP modified gold electrode when cycling between 0 and 0.8 V was induced by the cation radical of ATP. AFM images show that polyaniline deposited on mixed SAM of ATP and DT displays a random array of nanoelectrode. The theoretical fitting values of density and radius agree with the experimental values.

Polyaniline can react with both alkanethiol and amine in a mild environment, while the alkanethiol has much higher reaction rate than amine. As the protein contains the amino and thio groups, the covalent bonding between protein and polyaniline may exist. The efficiency of binding protein on to polyaniline increase significantly as the mole fraction of 4-ATP in the mixed 4-ATP/DT SAM decrease.

3.5 References

1. Yan, L.; Huck, W. T. S.; Whitesides, G. M. *J. Macromole. Sci.C.* **2004**, *44*, 175.
2. Azzaroni, O.; Schilardi, P.L.; Salvarezza, R.C. *Electrochim. Acta.* **2003**, *48*, 3107.
3. Hickman, J. J.; Ofer, D.; Laibinis, P. E.; Wrighton M. S. *Science* **1991**, *252*, 688.
4. Casero, E.; Darder, M.; Takada, K.; Abruna, H. D.; Pariente, F.; Lorenzo, E. *Langmuir* **1999**, *15*, 127.
5. Bardea, A.; Katz, E.; Willner, I.; *Electroanalysis* **2000**, *12*, 731.
6. Turyan, I.; Mandler, D. *Anal. Chem.* **1994**, *66*, 58.
7. Turyan, I.; Mandler, D. *Anal. Chem.* **1997**, *69*, 894.
8. Stora, T.; Hovius, R.; Dienes, Z.; Pachoud, M.; Vogel, H. *Langmuir* **1997**, *13*, 5211.
9. Gooding, J. J.; Hibbert, D. B. *TrAC - Trends Anal. Chem.* **1999**, *18*, 525.
10. Gooding, J. J.; Erokhin, P.; Hibbert, D. B. *Biosensors Bioelectronics* **2000**, *15*, 229.
11. Willner, I.; Lion-Dagan, M.; Marx-Tibbon, S.; Katz, E. *J. Am. Chem. Soc.* **1995**, *117*, 6581.
12. Gooding, J. J.; Hall, E. A. H.; Hibbert, D. B. *Electroanalysis* **1998**, *10*, 1130.
13. Levicky, R.; Herne, T. M.; Tarlov, M. J.; Satija, S. K. *J. Am. Chem. Soc.* **1998**, *120*, 9787.
14. Mazur, M.; Krysinski, P.; Palys, B. *J. Electroanal. Chem.* **2002**, *533*, 145.
15. Mazur, M.; Krysinski, P.; Jackowska, K. *Thin Solid Films* **1998** *330*, 167.
16. Mekhalif, Z.; Lang, P.; Garnier, F. *J. Electroanal. Chem.* **1995** *399*, 61.
17. Mekhalif, Z.; Delhalle, J.; Lang, P.; Garnier, F.; Caudano, R. *J. Electrochem. Soc.* **1999**, *146*, 2913.
18. Sayre, C.; Collard, D.M. *Langmuir* **1997**, *13*, 714.
19. Hayes, W.; Shannon, C. *Langmuir* **1998**, *14*, 1099.
20. Abaci, S.; Shannon, C. *Electrochim. Acta.* **2005**, *50*, 2967

21. Sabatani, E.; Gafni, Y.; Rubinstein, I. *J. Phys. Chem.* **1995**, *99*, 12305.
22. Chen, Y.; Kang, E.T.; Neoh, K.G.; Wang, P.; Tan, K.L. *Synthetic Metals* **2000**, *110*, 47.
23. Ladd, J.; Boozer, C.; Yu, Q.; Chen, S.; Homola, J.; Jiang, S. *Langmuir* **2004**, *20*, 8090.
24. Dong, Y. *Biosensing Based on Self-Assembled Monolayers, Atomic Force Microscopy and Electrochemistr; Ph.D. Dissertation* **2001**, Auburn University, Auburn, AL.
25. Liu, H. *Characterization of Two-component Organothiol Mixed Monolayers on Gold and Quantification of Nonspecific Adsorption on Mixed SAM Biosensor Platforms Using Electrochemical Enzyme Immunoassay; M.S. Thesis* **2007**, Auburn University, Auburn, AL.
26. Raj, C. R.; Kitamura, F.; Ohsaka, T. *Langmuir* **2001**, *17*, 7378/
27. Yang, Y. W.; Fan, L. J. *Langmuir* **2002**, *18*, 1157.
28. Poirier, G. E. *Langmuir* **1999**, *15*, 1167.
29. Fitts, W. P.; White, J. M. *Langmuir* **2002**, *18*, 2096.
30. Hayes, W.; Kim, H.; Yue, X.; Perry, S.; Shannon, C. *Langmuir* **1997**, *13*, 2511.
31. Pekmez, N.; Pekmez, K.; Yildiz, A. *J. Electroanal. Chem.* **1994**, *370*, 223.
32. Rajendran, L.; Sangaranarayanan, M. V. *J. Phys. Chem. B* **1997**, *101*, 4583.
33. Kolev, S. D.; Stmons, Jo H. M.; van der Linden, W. E. *Anal. Chim. Acta* **1993**, *273*, 71.
34. Rajendran, L.; Ananthi; S.P. *J. Electroanal. Chem.* **2001**, *501*, 210.
35. Oldham, K. B. *J. Electroanal. Chem.* **1991**, *291*, 317.
36. Phillips, C. G. *J. Electroanal. Chem.* **1992**, *333*, 11.
37. Bond, A. M.; Luscombe, D.; Oldham, K. B. Zoski, C. G. *J. Electroanal. Chem.* **1988**, *249*, 1.
38. Scharifker, B. R. *J. Electroanal. Chem.* **1988**, *240*, 61.
39. Avrami, M. *J. Chem. Phys.* **1939**, *7*, 1103.

40. Avrami, M. *J. Chem. Phys.* **1940**, *8*, 212.
41. Avrami, M. *J. Chem. Phys.* **1941**, *9*, 177.
42. Grennan, K.; Killard, A. J.; Hanson, C. J.; Cafolla, A. A.; Smyth, M.R. *Talanta* **2006**, *68*,1591.
43. Han, C-C.; Jeng R-C. *Chem. Commun.* **1997**, 553
44. Nowall, W.; Kontha, N.; Kuhr, W. G. *Biosensors Bioelectronics* **1998**, *13*, 1237.
45. (a) Barton, A. C.; Collyer, S. D.; Davis, F.; Gornall, D. D.; Law, K. A.; Lawrence E. C. D.; Mills, D. W.; Myler, S.;Preitchard, J. A.; Thompson, M.; Higson, S. P. J. *Biosensors Bioelectronics* **2004**, *20*, 328. (b) Myler, S.; Collyer, S. D.; Davis, F.; Gornall, D. D.; Higson, S. P. J. *Biosensors Bioelectronics* **2005**, *21*, 666

CHAPTER 4
FABRICATION OF FILMS CONTAINING PERIODIC NANOFEATURES
BASED ON NANOSPHERE LITHOGRAPHY

4.1 Introduction

Electron beam lithography and x-ray lithography, which are the current leading nanolithographic fabrication techniques, are powerful tools for achieving good resolution of submicron features¹⁻⁴. Electron beam lithography has better resolution (1~2 nm) and x-ray lithography has better throughput because of its parallel processing capabilities. However, electron beam lithography has limited throughput due to the serial processing and x-ray lithography has limited resolution, and both technique are of high cost. Researchers were interested in developing alternative techniques that combine the advantages of the resolution of electron beam lithography and the high throughput of the x-ray lithography, and ideally be low-cost and simple. “Nanosphere lithography” is a technique that has the potential to fabricate inexpensive parallel nanostructures with fine resolution.⁵⁻¹⁰

The nanosphere was used as a surface material. The close packed hexagonally arranged spheres compose a crystal surface which can be used for optical devices. The nanospheres may also be modified, e.g. by ion etching, to obtain surfaces with desirable optical properties.^{6,11-13}

However, more often, the nanosphere lithography is used to fabricate templates which are able to produce surfaces containing regular featured arrays in nanoscale. For example, various surfaces were made by physically depositing desired species (metals or nonmetals) through the modified or unmodified nanosphere templates at various angles. A typical result is an array of nanoparticles arranged in various styles dependent on the depositing angle. The shape and size of the nanoparticles could be further tuned by thermal annealing. Other typical results of physical deposition are the array of nanorods or nanowires and the array of nanopores. The nanorods or nanowires could also be obtained by reactive ion etching.^{8,13-19} Electrochemical deposition was also used to achieve two-dimensional or three-dimensional porous films of metal or semiconductor which is grown in the interstitial spaces of the nanosphere lithographic templates on the electrical conductive substrates. The porous films have some unique magnetic, optical or surface wetting properties. Electroless plating has extended the porous structures onto insulators.^{9,21-25}

Compared to the physical deposition, the electrochemical deposition and the electroless plating have the advantage of being able to produce a large area of homogeneous structure (include three-dimension structures). However, the types of surface features made from physical deposition are more versatile. The aim of this work is to fabricate the nano-feature arrays via nanosphere templates, and explore the feasibility of the resulting surface features through tuning the electrochemical deposition conditions. The obtained nano-arrays should be able to be applied in analytical chemistry, for example, being used to study electrochemistry and used in the fabrications of sensors.

4.2 Experimental Section

Materials. Monodisperse polystyrene latex spheres (diameters 300, 600, 1000 and 3600(\pm 20) nm) were purchased from Interfacial Dynamics Corporation (Portland, OR), as 8.1 wt% solutions in water. Silver nitrate, zinc oxide, copper sulfate were obtained from Sigma-Aldrich. All solvents and chemicals were of reagent quality and were used without further purification. Substrate electrodes were prepared by sputter coating 50 nm of gold on to newly-cleaved mica and were cleaned by sonication in propanol for 20 minutes and then stored in deionized water before use. All solutions were prepared using reagent grade water (18.2 M Ω cm) from a Barnstead “NANO infinity” ultrapure water system.

Polystyrene nanosphere templates prepared by spin coating. Nanosphere templates were created by spin coating 600(\pm 20) nm polystyrene nanospheres on to the substrates at 900 - 3600 rpm on a custom-built spin coater. The physical dimensions of the substrates were chosen to be in the range 0.25–1.0 cm² and the entire substrate was spun coated with nanospheres. The nanospheres were received from the manufacturer as a suspension in water and then further diluted in a solution of the surfactant Triton X-100/methanol (1:400 by volume) before spin coating. The surfactant was used to assist the solutions in wetting the substrate. The specimen-to-specimen reproducibility of NSL mask preparation was excellent.

Polystyrene nanosphere templates prepared by assembling. The preparation of polystyrene nanosphere templates was carried out by sticking a 1.0 cm diameter Teflon ring onto the gold-coated mica substrate using double-sided tape. The polystyrene nanospheres were diluted to 0.5 wt% with water and a volume of 0.1 - 0.3 cm³ was

spread over the area of the gold electrode enclosed by the Teflon ring. We then used sedimentation and attractive capillary force to pack the spheres. The sedimentation of the spheres was achieved by keeping the samples in a well-closed chamber and they were allowed to sediment over a period of 1 to 3 days depending on sphere diameter. Once the latex spheres settled on to the gold substrate, a clear water layer was observed on the top of the deposit. This water layer was then allowed to evaporate over a period of 1–2 days. The attractive capillary forces pack the spheres within the template. After the complete evaporation of water, the Teflon ring was removed to leave a circular area covered by the template. The template free gold area was covered with silicone gel to prevent any electrodeposition on to it.

Table 4.1. The components of the aqueous plating solutions and the potential applied.

Species	Plating solution components	Potential (mV) vs Ag/AgCl
Cu	10 mM CuSO ₄ , 100 mM Na ₂ SO ₄	-400~0 mV
Ag	10 mM AgNO ₃ , 100 mM NaNO ₃	0 ~ +300 mV
CdSe	200mM CdSO ₄ , 1mM SeO ₂ , 50mM HClO ₄	-600 mV
ZnO	100 mM Zn(NO ₃) ₂	-700 ~ -1000 mV

Electrochemical deposition Electrodeposition was carried out using Cypress Systems Omni-101 potentiostat and workstation. A standard three-electrode system was used with a platinum net counter electrode and a Ag|AgCl(sat) reference electrode. Chronoamperometry or controlled potential electrolysis was used to deposit desired

species. The composition of the plating solution and the potential in the chronoamperometric technique are given in Table 4.1.

Removal of Nanospheres. After deposition of the desired species, the polystyrene nanospheres were removed from the substrate by dissolving them in dichloromethane with sonication from 1 to 3 min.

AFM analysis. All AFM images were acquired using an atomic force microscope autoprobe CP (Park Scientific) in a contact mode, equipped with an acquisition module (Thermomicroscope). The tips with a force constant of 0.12N/m were purchased from Digital Instruments Co. The samples were scanned on a 100 μm piezoelectric scanner. A video camera integrated with a microscopic objective piece was used to monitor laser beam location on the silicon cantilever. The images obtained were analyzed with PSI ProScan 1.5 data analysis software.

4.3 Result and discussion

4.3.1 Nanosphere template

The substrates were prepared by sputter coating a layer of Au on to clean mica without adding the adhesive layer between the Au layer and the mica. Au was selected because of its capability of forming a robust layer on mica. The sputter-coated layers of other metals such as Pt and Ag are often separated from the mica in solution during the process of electrodeposition or removal of polystyrene spheres in dichloromethane.

In this work, the nanosphere lithographic templates were mostly prepared by spin coating. For the spheres whose diameters ranged from 300 nm to 1000 nm, templates prepared by the spinning coating were successfully coated with large domains of defect-

free packing over the entire substrate surface. However, for the larger sized spheres (eg. $d = 3600(\pm 20)$ nm), spin coating did not work well. The spheres could not stay on the gold surface and the templates were mostly sphere free when the spinning rate was above 900 rpm. (The solution containing the polystyrene spheres did not spread well on Au surface if the spinning rate was below 900 rpm)

Assembling works well with all of the spheres of all sizes. The sphere templates prepared by this method were normally multilayer and had very good surface coverage of spheres on the area inside the Teflon ring.

Templates prepared by both methods were very stable in aqueous solution. Spheres did not liftoff from the gold layer in the aqueous solution even with the aid of ultrasonication. Templates coated with nanospheres with a diameter of 600 or $1000(\pm 20)$ nm produced different colors depending on their view angle. However, this phenomenon was not observed from the templates of nanospheres with small (e.g. $300(\pm 20)$ nm) or large diameters (e.g. $3600(\pm 20)$ nm), due to the fact that the pore diameter of these two template are not in the range of wavelengths of visible light.⁹

Figure 4.1 is an AFM picture of polystyrene nanosphere lithography templates. The nanospheres are arranged in a well-defined hexagonal pattern. There are six interstice spaces surrounding a polymer sphere.

4.3.2. Periodic pore-array film

After a certain amount of desired species were deposited on to the Au electrode under the sphere template, the spheres were removed from the substrate. One of the common results obtained was the formation of a periodic pore film on the gold surface.

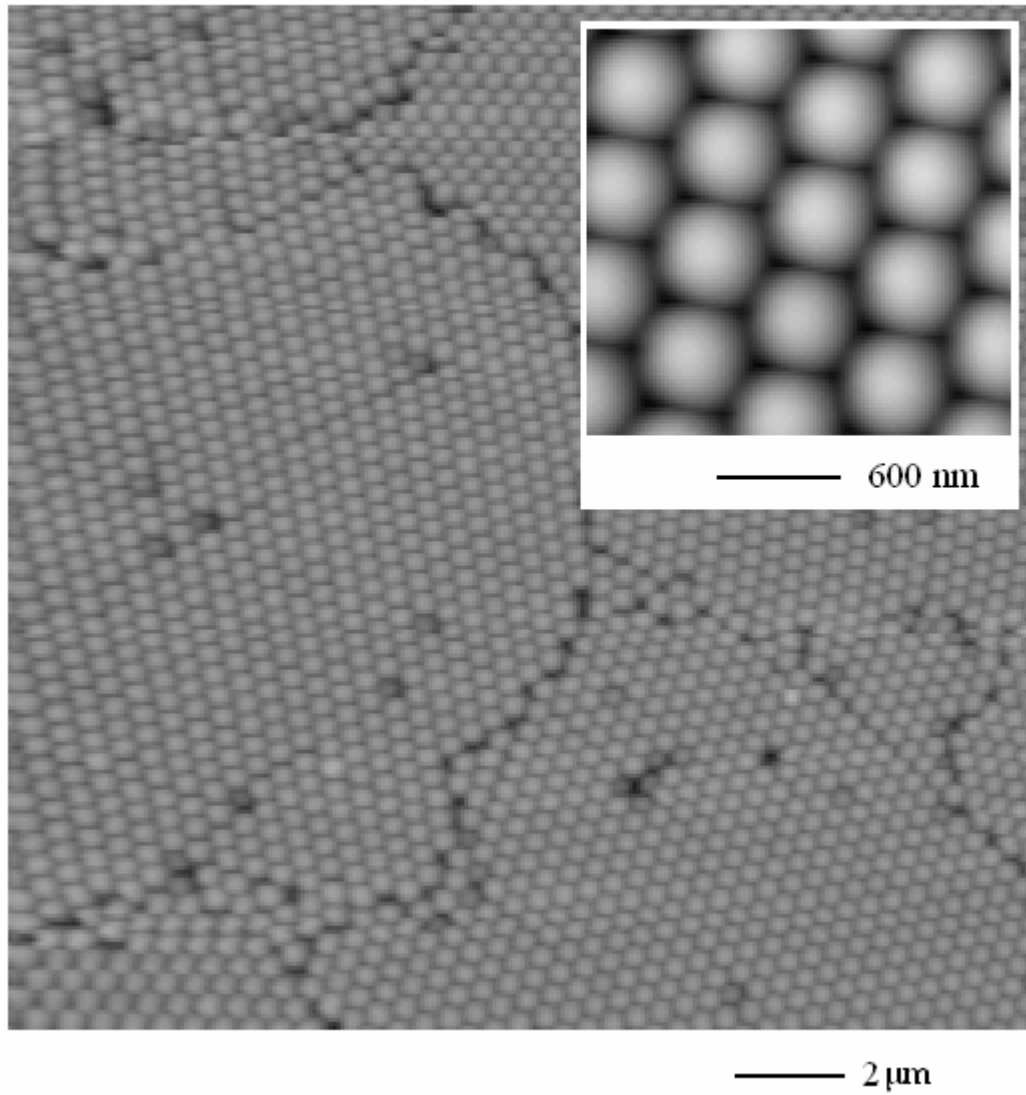


Figure 4.1. AFM image of the template spin-coated from 600(\pm 20) nm diameter polystyrene spheres.

The AFM and SEM data showed that nanosphere lithography was able to produce a large area of periodic pore film. Figure 4.2 and 4.3 show two AFM images of the periodic pore copper films that were deposited through two different templates. The template used to produce the copper film in Figure 4.2 was spin-coated using 600(\pm 20) nm diameter polystyrene spheres. The spherical pores in Figure 4.2 are arranged in the same hexagonal format as the polystyrene spheres in Figure 4.1. The template used to produce the copper film in Figure 4.3 was assembled using 3600(\pm 20) nm diameter polystyrene spheres. From Figure 4.3, we observe by vision that at the bottom of each pore, there is a large circular area of gold surface left uncovered.

These nanopore arrays may be used in electrochemical sensors. When electrochemical sensors have one dimension that is smaller than the diffusion length of the analyte, their performance might be dramatically improved sensitivities and detection limits because of their increased mass transport towards the electrode (due to the radial diffusion), reduced double-layer capacity, and reduced Ohmic drop (small currents).²⁶ Due to the small physical sizes, nanoelectrode arrays are good for trace amount of sample. They are also suitable in a small environment of being integrated in a portable device. Zhou et al.²⁷ have fabricated a DNA sensor by immobilizing HS-ss-DNA on gold surface through replacing one component of mixed self-assembled monolayer. The DNA hybridization efficiency was greatly improved, probably due to the separation between the single strand DNA probes. The nanopore-array electrodes fabricated in this work are expected to improve the DNA hybridization efficiency if the HS-ss-DNA is immobilized in the pores. The films containing nanopores have many other applications such as being used as substrates for NIR-SERS²⁸ or as special materials.²³

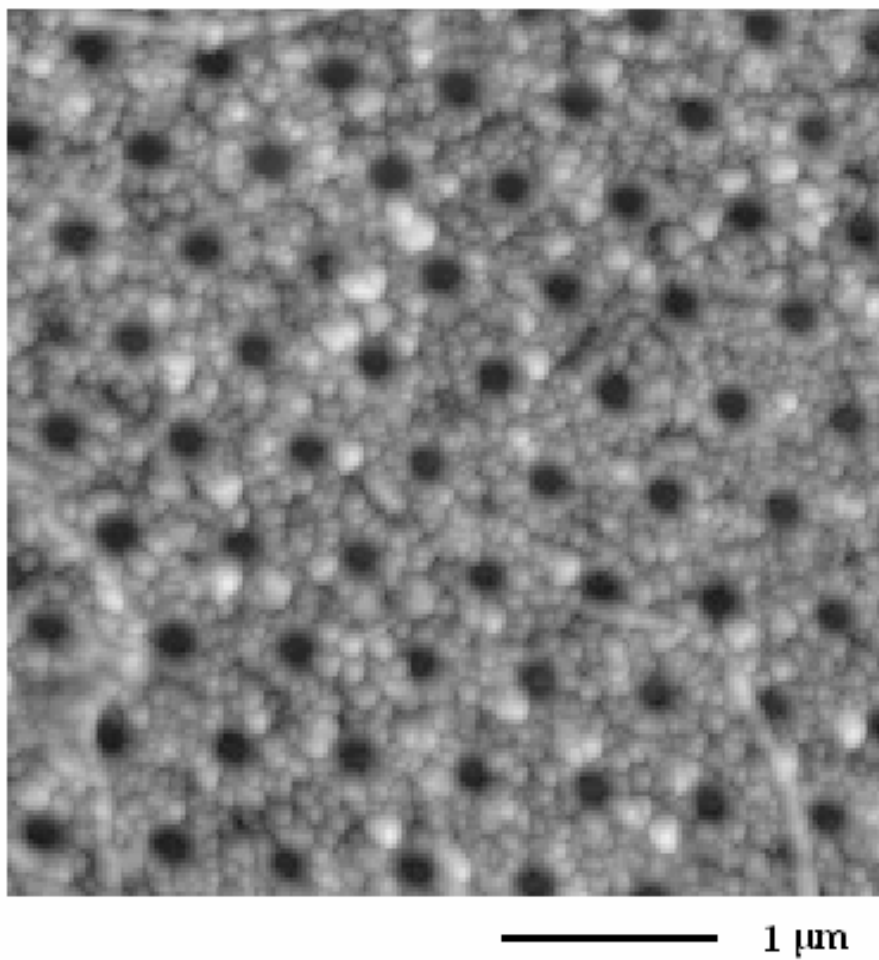


Figure 4.2. Periodic porous films electrochemically deposited through the sphere template. The diameter of the sphere = $600(\pm 20)$ nm.

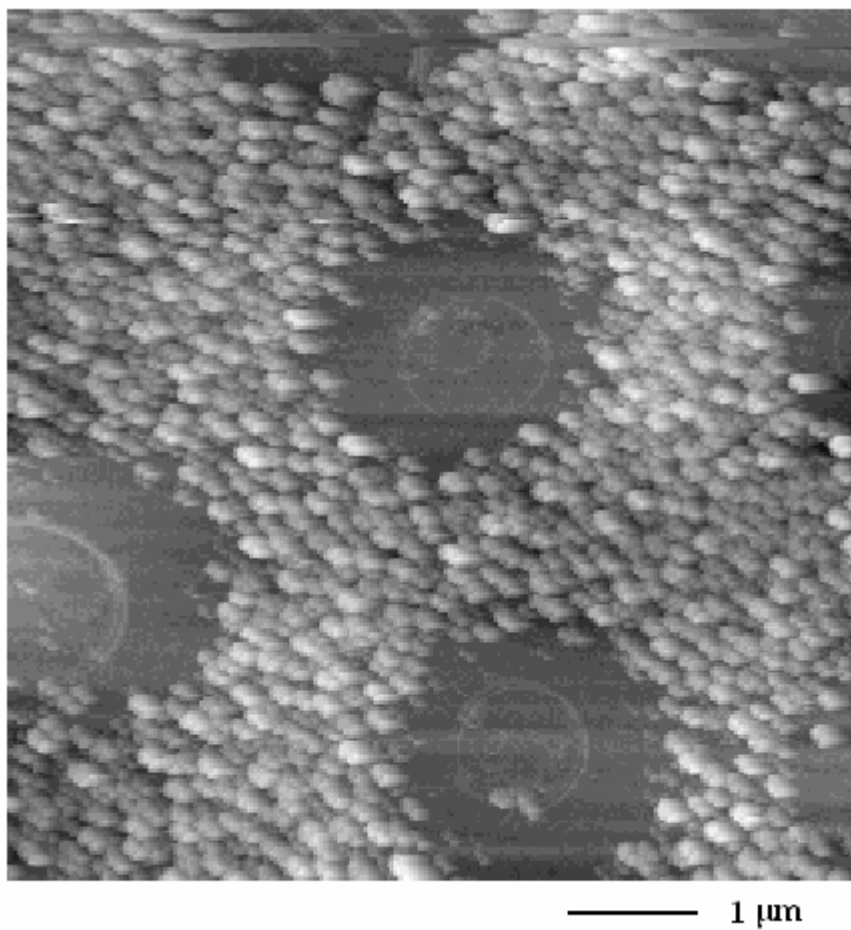
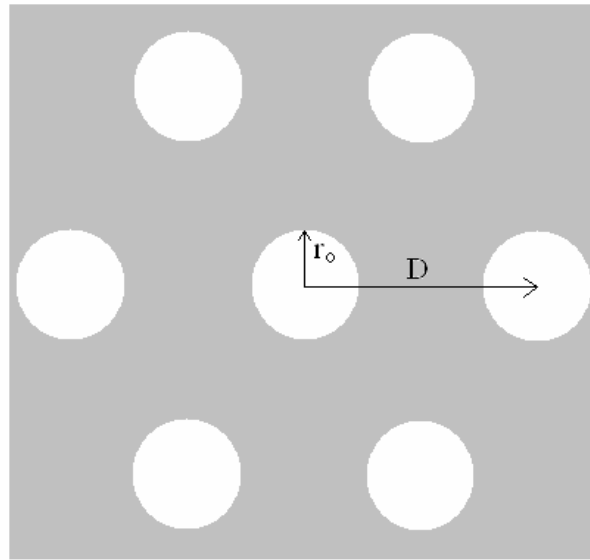


Figure 4.3. Periodic porous films electrochemically deposited through the sphere template. The diameter of the sphere = $3600(\pm 20)$ nm.

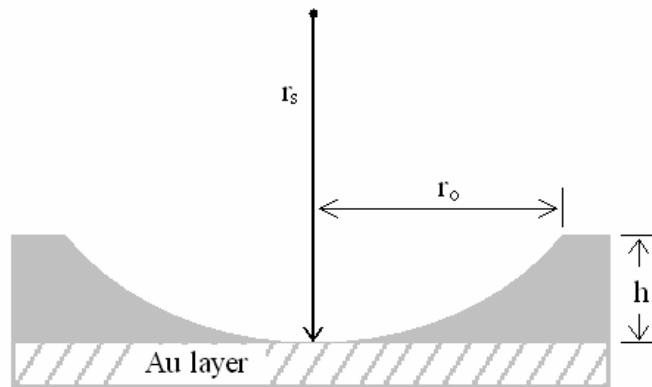
Terms. In order to better describe the film, some terms must be defined. In Figure 4.4, the radius of the polystyrene sphere is assigned as r_s . The distance between the centers of two neighboring spherical pores is D ($D = 2r_s$). The thickness of the film electrochemically deposited is assigned as h . The radius of the circular opening area at the top of the hemispherical pore is assigned as r_o . From Figure 4.4(b), it is clear that the r_o is dependent on the thickness of the film, h . For an ideal spherical pore,

$$r_o = \sqrt{r_s^2 - (r_s - h)^2} \quad (4.1)$$

Investigation of the pores. The radius of the circular opening area at the top of the hemispherical pore, r_o , is very important to its electrochemical behavior. While, there was no research on r_o in earlier work. Here, the variation of r_o with film thickness was investigated. Figure 4.5 shows plots of the values of r_o , measured from AFM or calculated from equation 4.1, as the function of film thickness. In the Figure 4.5, for the film fabricated from the polystyrene template coated by 600(\pm 20) nm diameter spheres, the measured r_o values of the pores (curve a) at different thickness agree with those calculated using equation 4.1 (curve a'), which assume that the pore was occupied by perfect sphere. This means, the polystyrene sphere did not significantly change its shape after being coated on to the Au surface. Therefore, the radius of the spherical mouth of pore, r_o , in the film can be controlled simply through tuning the film thickness, h , using equation 4.1. Figure 4.6 shows that the film thickness increases linearly as the electrochemical deposition time increases. Combination of the above two results gives that the value r_o can be controlled using the electrochemical deposition time.



(a)



(b)

Figure 4.4. Terms of the film. (a) The schematic top view of the periodic pore film. The white circular areas are the pores, which is previously occupied by polystyrene spheres. (b) The schematic cross section view of an ideal spherical pore in the periodic pore film.

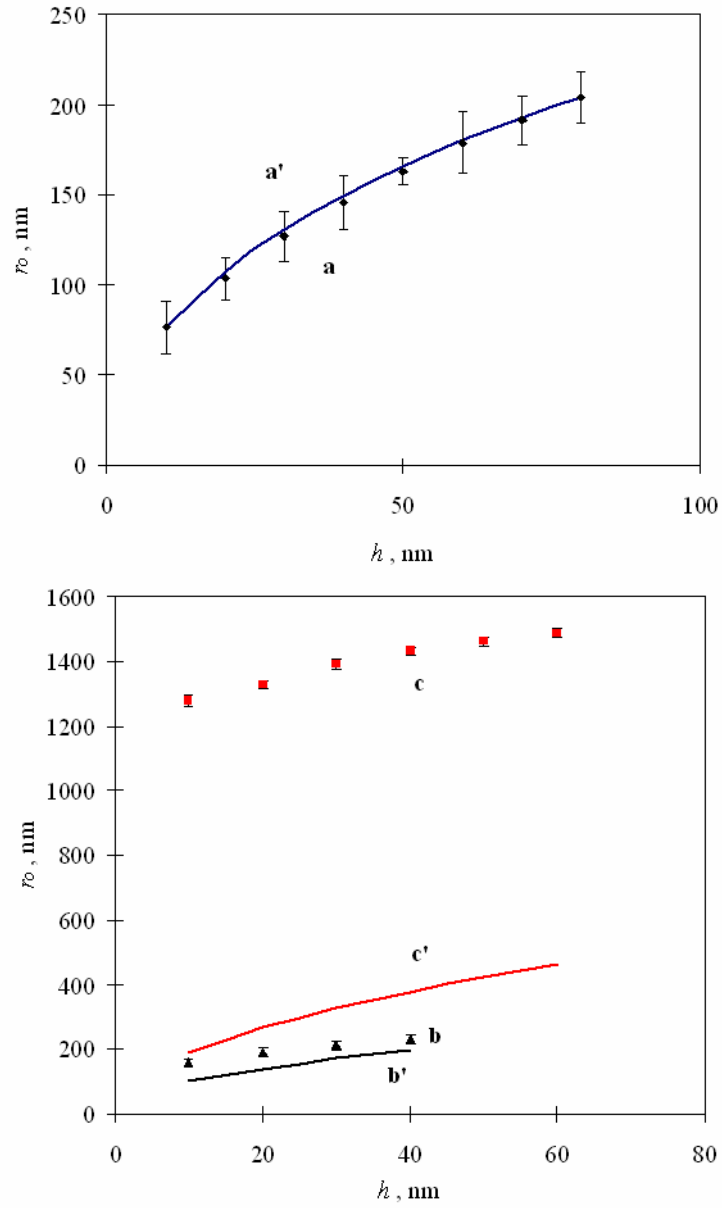


Figure 4.5. Plots of r_o as the functions of film thickness. (a) \blacktriangle measured value, $r_s = 300$ nm, (a') calculated value, $r_s = 300$ nm, (b) \blacksquare measured value, $r_s = 500$ nm, (b') calculated value, $r_s = 500$ nm, (c) \blacklozenge measured value, $r_s = 1800$ nm, (c') calculated value, $r_s = 1800$ nm.

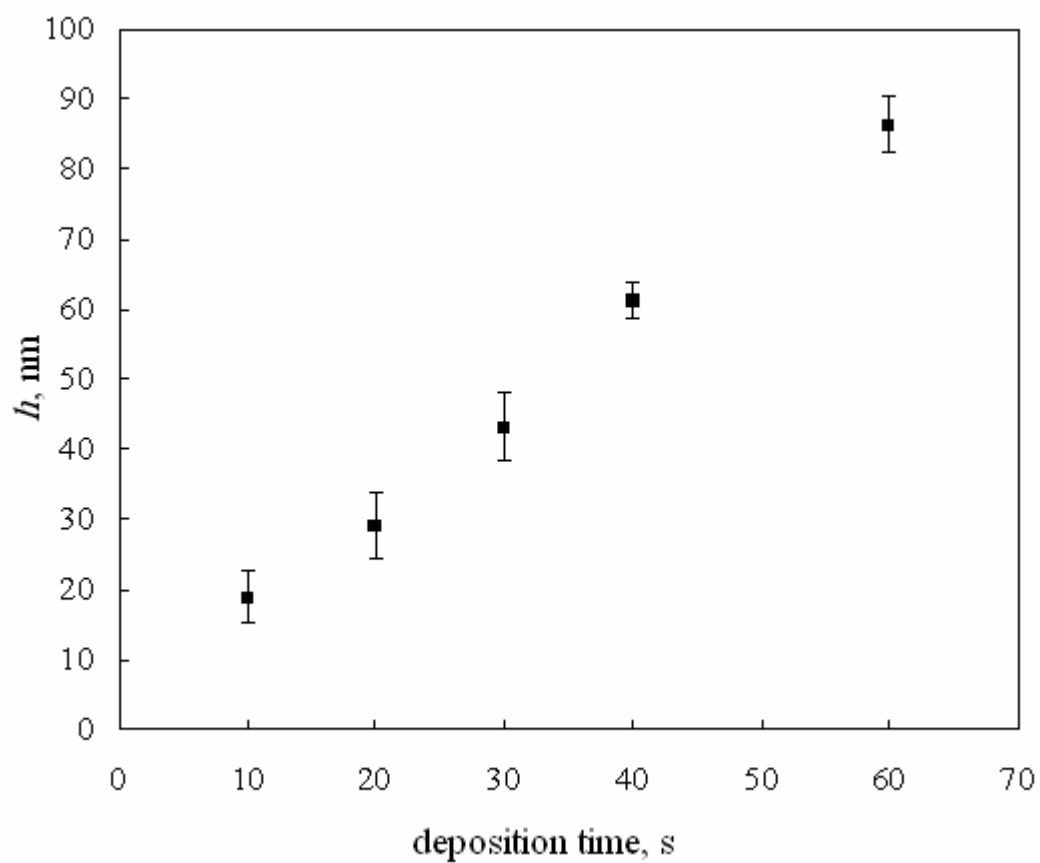


Figure 4.6. Film thickness as a function of electrochemical deposition time. The diameter of the sphere on the template is $600(\pm 20)$ nm.

Table 4.2 shows the values of r_b and D/r_b for at different r_s . As the radius of polystyrene sphere (r_s) of the template increases, the radius of the circular area at the bottom of pore (r_b) increases at a higher rate. Thus D/r_b decreases with the increase of r_s .

Table 4.2. The value of r_b and D/r_b for the copper films deposited through three different templates.

r_s nm	r_b	D/r_b
1800	1015.2	3.4
500	135.1	7.4
300	71.1	8.4

Cyclic voltammetry of recess electrode assemblies.

Because micro-/nanoelectrodes have at least one dimension that is smaller than the diffusion lengths, the diffusion of the analyte to micro-/nanoelectrodes is three-dimensional (radial). The cyclic voltammogram of a single micro-/nanoelectrode shows sigmoidal curve. For a micro-/nanoelectrode array, the diffusion profile may vary from linear to radial, depending on the overlap of the diffusion profile on each micro-/nanoelectrode. Therefore, the cyclic voltammogram of a micro-/nanoelectrode array may also vary from “duck” shape to sigmoidal shape. Here, ZnO (bandgap = 3.37 eV) films were deposited through the nanosphere templates. The deposited ZnO formed an insulate layer on the gold surface. Thus, the electrochemical events will happen mostly at the pore where the gold surface was exposed. The cyclic voltammogram of the gold electrode covered with a ZnO pore film in a solution containing 1mM $K_3Fe(CN)_6$ and 0.5 M

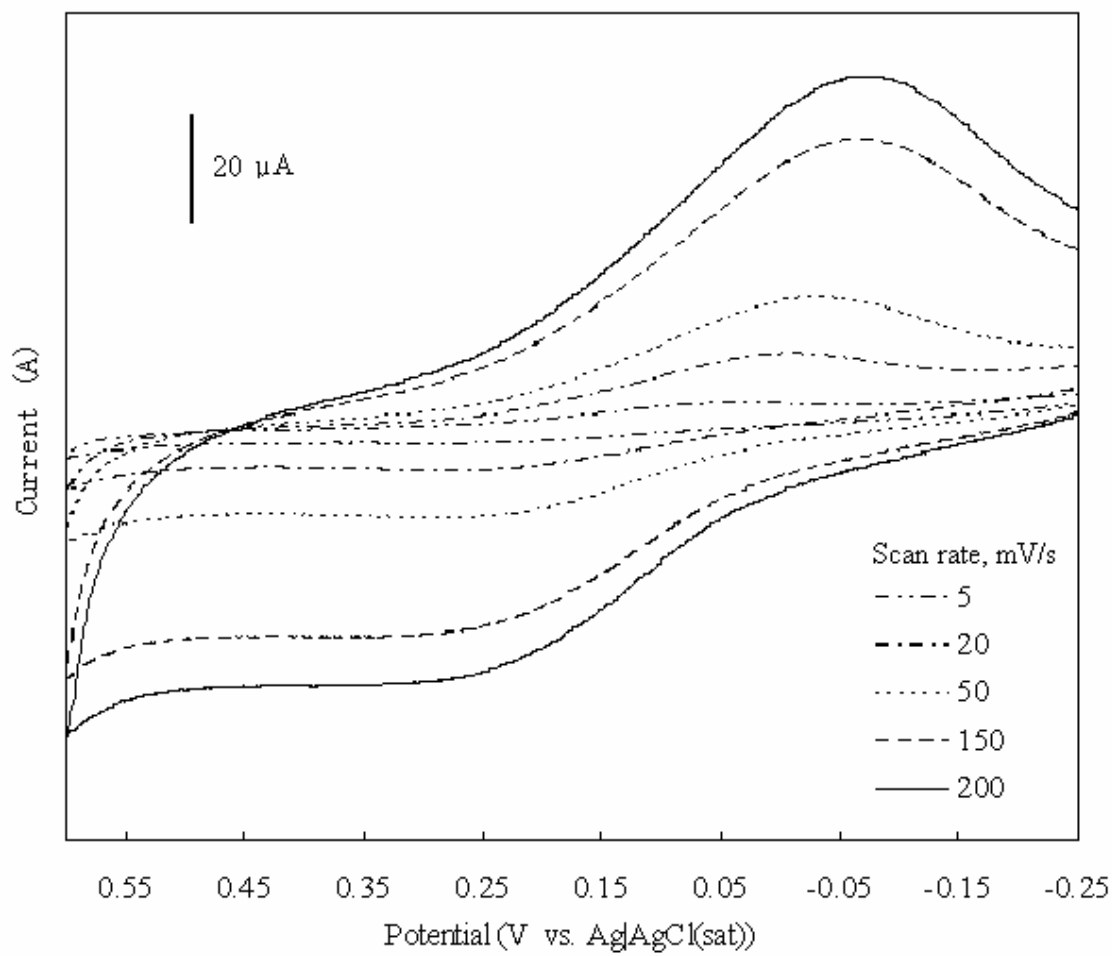
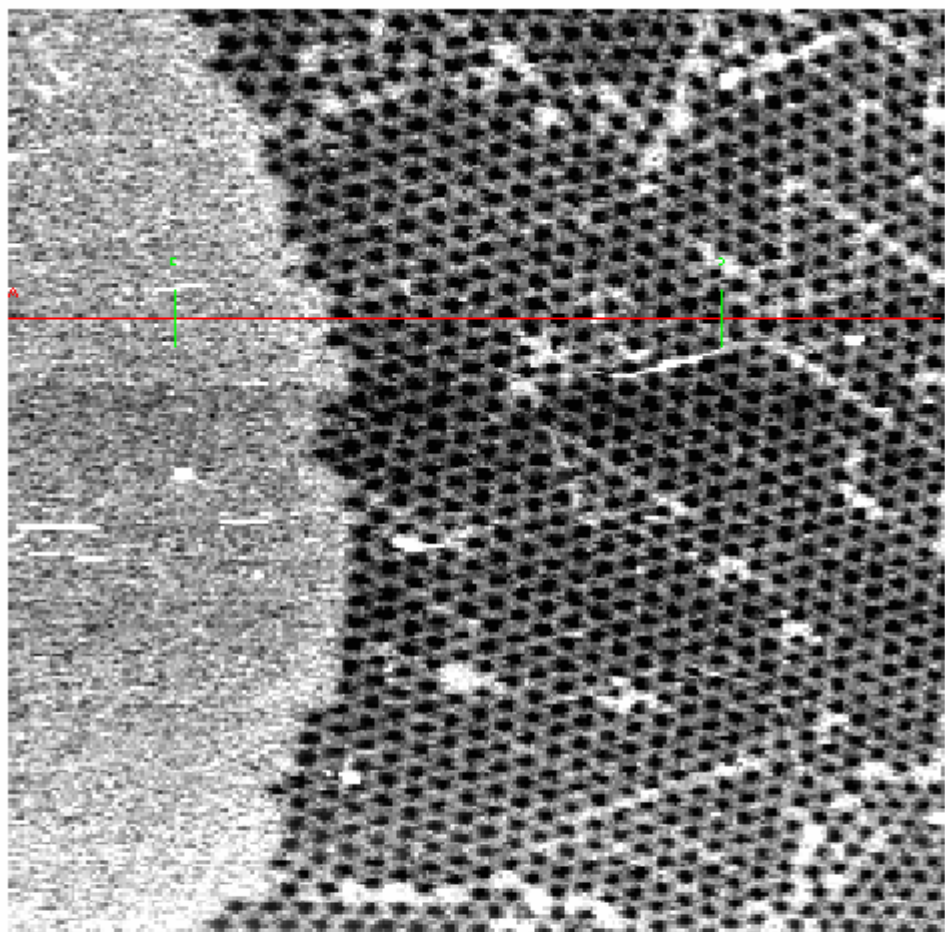


Figure 4.7. Cyclic Voltammetric behavior of ZnO pore film in 1mM $\text{K}_3\text{Fe}(\text{CN})_6$ and 0.5 M Na_2SO_4 with various scan rates.

Na₂SO₄ is shown in Figure 4.7. The scan rate ranges from 5 to 200 mV/s. The recess electrode assemble shows the characteristics of macroelectrode when the scan rate is high. As the scan rate decreases, the cyclic voltammogram shows characteristics of the microelectrode. Still, the sigmoidal curve was not obtained. Failure in showing the behavior of the microelectrode may be explained by the relatively small size of the individual recess electrode and the D/r_b .

Sandison etc.³⁰ pointed out that D/r is a very important parameter that greatly affects the behavior of the microelectrode ensemble. A large D/r is ideal for producing the sigmoidal shape cyclic voltammetric curve, which means the radial diffusion to the electrode. For the microelectrode ensemble with an individual electrode diameter of 5 μ m, an approximate value of $D/r = 40$ is required to achieve radial diffusion. As the individual electrode diameter increases, an even larger D/r is needed to maintain the radial diffusion for the micro-/nanoelectrode ensemble. Table 4.2 shows that the values of r_b and D/r_b for three different templates. Here, all the diameters of the pores in any of the films are smaller than 5 μ m and all the D/r_b are less than 40, the diffusion to the nanopore electrode is not expected to be radial. Table 4.2 shows that as the r_s decreases, r_b decreases very fast, leading to a significant increase of the D/r_b . Thus, a smaller r_s is desirable to achieve radical diffusion. This explanation is consistent with Ito et al.'s work.³⁰ The cyclic voltammetry of recessed nanodisk-array electrodes fabricated from track-etched polycarbonate membranes showed the transition between linear and radial diffusion modes, depending on the inter electrode distance.



— 2 μm

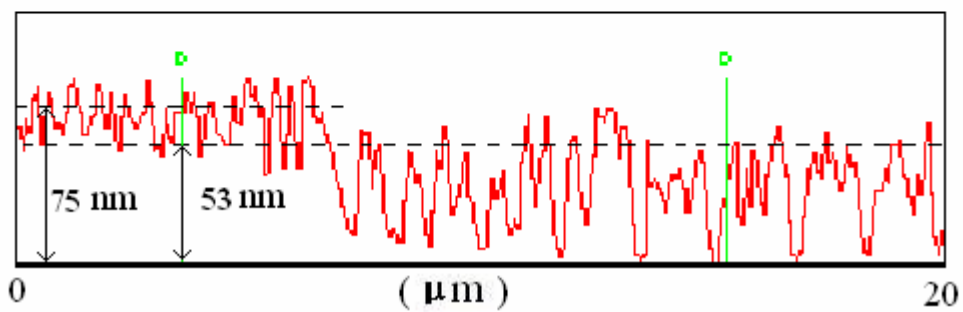
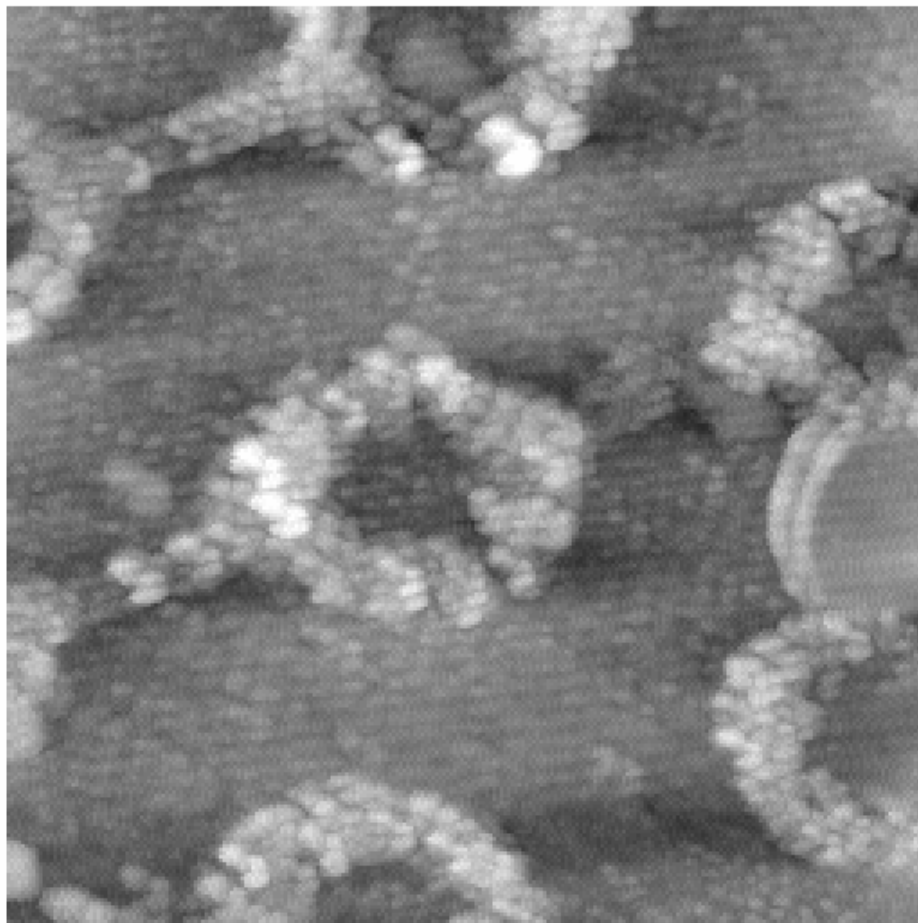


Figure 4.8. AFM image of copper film containing the areas previously covered or uncovered by polystyrene template. The diameter of the sphere = $600(\pm 20)$ nm.

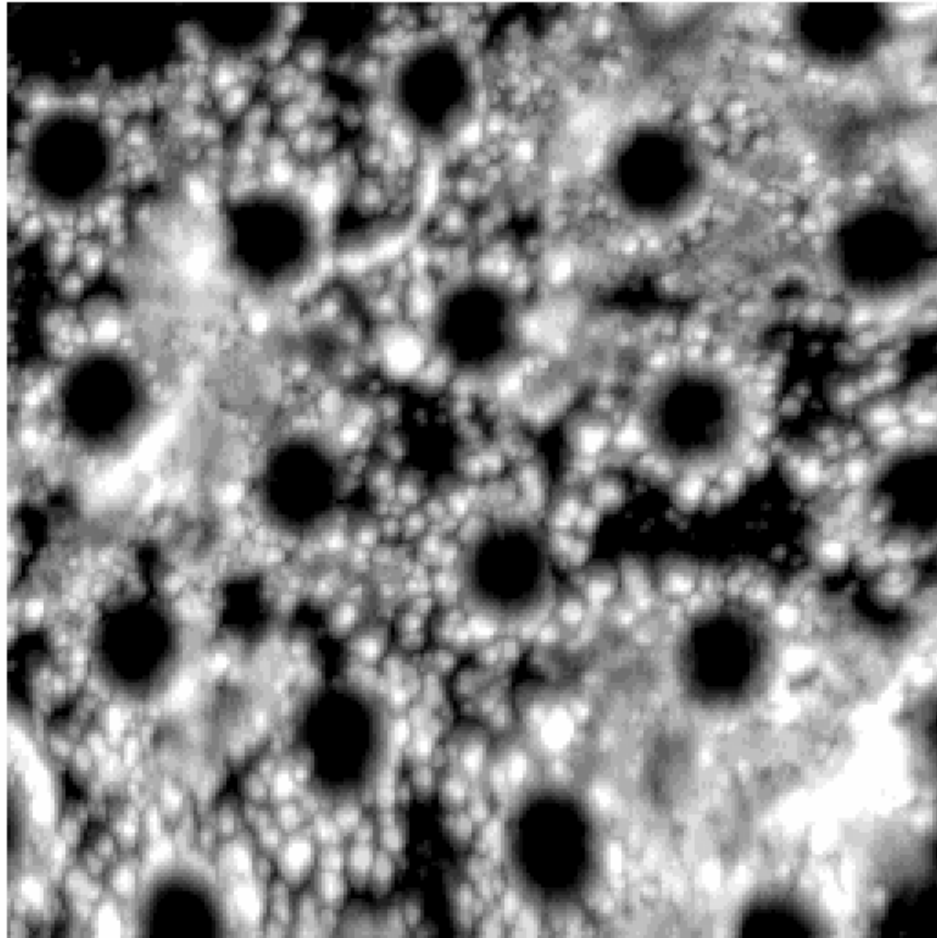
Difference of the film thickness between the areas previously covered with polystyrene spheres and open area. The area previously covered with polystyrene sphere turned out to be the pore film after electrochemical deposition. However, some areas on the gold electrode were not covered by polystyrene spheres. On these open areas, usual electrochemical plating took place and a pore-less layer of copper was formed. Figure 4.8 shows an AFM image of the copper film containing pore and pore-less areas. The cross-section view of the copper film obtained from AFM analysis is given under the AFM image. It is shown in the cross-section view that the thickness of pore-free film was slight larger than that of pored film. The reason of this difference in thickness is that the polystyrene mask formed on the gold surface slows down the movement of copper ions from bulk solution to the interstice space. After a deposition of 30 seconds or more, the concentration of copper ion in the interstice space will be significantly lower than the one in the bulk solution. Therefore, the rate of electrochemical deposition on the area covered by the sphere template is slower than on the open area.

A proposed growing process of film. To understand how the film is grown on to the gold surface under the polystyrene spheres, the electrochemical deposition time was reduced while the deposition potential kept constant. Figure 4.9 and 4.10 show AFM images of copper deposited on gold surface at a potential of -100mV for 3 or 8 seconds, respectively. Based on the images in the Figure 4.9 and 4.10, a possible film growing process is proposed - due to the sulfate groups on the polystyrene sphere surface, the polystyrene sphere surface carries negative charges (the charge density is around $5 \times 10^5 \mu\text{m}^{-2}$). The cations in the solution are attracted to the surface of the polystyrene sphere



— 100 nm

Figure 4.9. AFM image of copper deposited on gold surface through sphere template. The diameter of the sphere = $600(\pm 20)$ nm. Potential = -100 mV. Time = 3 seconds.



————— 500 nm

Figure 4.10. AFM image of copper deposited on gold surface through sphere template. The diameter of the sphere = $600(\pm 20)$ nm. Potential = -100 mV. Time = 8 seconds.

and the ring-shape area surrounding the sphere has much higher concentration of Cu^{2+} . Thus, the nucleation of copper ions on this area is much faster than other place and the rings formed, which is shown in the Figure 4.9. As the copper rings form, the nucleation expands out and the size of the ring grows as is shown in Figure 4.10. The nucleation continue expanding until the all the area between the rings that is filled. Now, a film of periodic pore-array forms. After that, the surface coverage of copper does not increase.

The Na^+ ions in the solution of the electrolyte were also attracted by the negative charges on the surface of the polystyrene sphere. It was suspected that the Na^+ ions may reduce the effect of negative charge of the polystyrene sphere on the formation of the rings. However, the rings were still found on the Au surface when the concentration of the electrolyte, Na_2SO_4 , was increased from 100mM to 1000mM while the concentration of CuSO_4 was kept at 10mM.

When 20mM of EDTA^{4-} was added to the plating solution which contains 10mM CuSO_4 and 500mM Na_2SO_4 and the plating potential was set to -900mV, no ring was found on the Au surface. The reason was that as the EDTA^{4-} was added in the plating solution, the Cu^{2+} was bound by EDTA^{4-} and forms CuEDTA^{2-} , thus the negative charge of the polystyrene sphere repels CuEDTA^{2-} and the concentration of CuEDTA^{2-} of the solution close to the polystyrene sphere is reduced.

If a cationic surfactant, Cetyltrimethylammonium bromide (CTAB)/methanol (1:200 by mass), was used to dilute the nanosphere suspension before the template preparation, CTAB adsorbing on the surface of polystyrene spheres in the template.³² The positive charges carried by CTAB neutralized the negative charges on the surface of

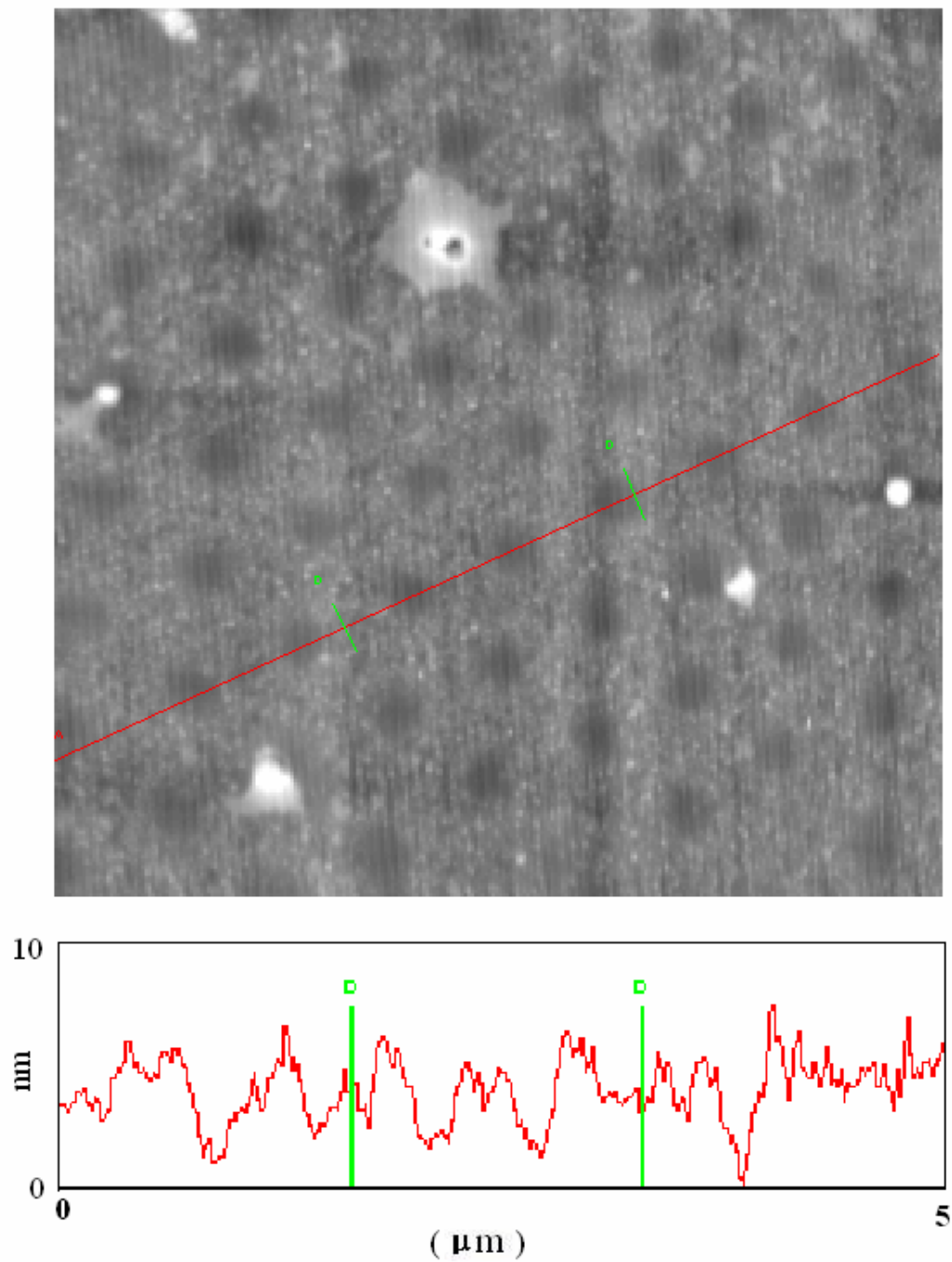


Figure 4.11. AFM image of copper deposited on gold surface through sphere template. The diameter of the sphere = $600(\pm 20)$ nm. Potential = -100 mV. Time = 2 seconds. CTAB/methanol (1:200 by mass), was used to dilute the nanosphere suspension before the template preparation.

polystyrene spheres. Thus, the attraction of Cu^{2+} by to the polystyrene spheres was reduced or eliminated. Figure 4.11 show AFM image and the height analysis of the copper film deposited. It was shown that no ring formed even the film thickness is as small as 7nm.

4.3.3. Periodic particle-array film electrochemically deposited through a 600 nm diameter sphere template

Another interesting surface feature found on the Au electrode was the triangular particles arranged in a hexagonal pattern. In one experiment, a nanosphere lithography template was immersed in a solution containing 10mM CuSO_4 and 100mM Na_2SO_4 . Copper was deposited on to the gold surface under the polystyrene spheres via chronoamperometric technique in which a current of 500nA was applied. After electrochemical deposition for 30 min, the polystyrene mask was removed, revealing the growth of triangular particles on the gold surface. An AFM image of periodic particle array is presented in Figure 4.12. From the figure, we can see that the triangular particles are arranged hexagonally around a pore, which was occupied by a nanosphere whose diameter was 600 (± 20)nm. The in-plane diameter of the triangle particle is defined as the perpendicular bisector of the largest inscribed equilateral triangle. The average in-plane diameter of the particle was 250(± 10) nm. The average out-of-plane height of the particles was 24(± 3) nm. Each pore connects to the neighboring pore by the valley between two triangular particles.

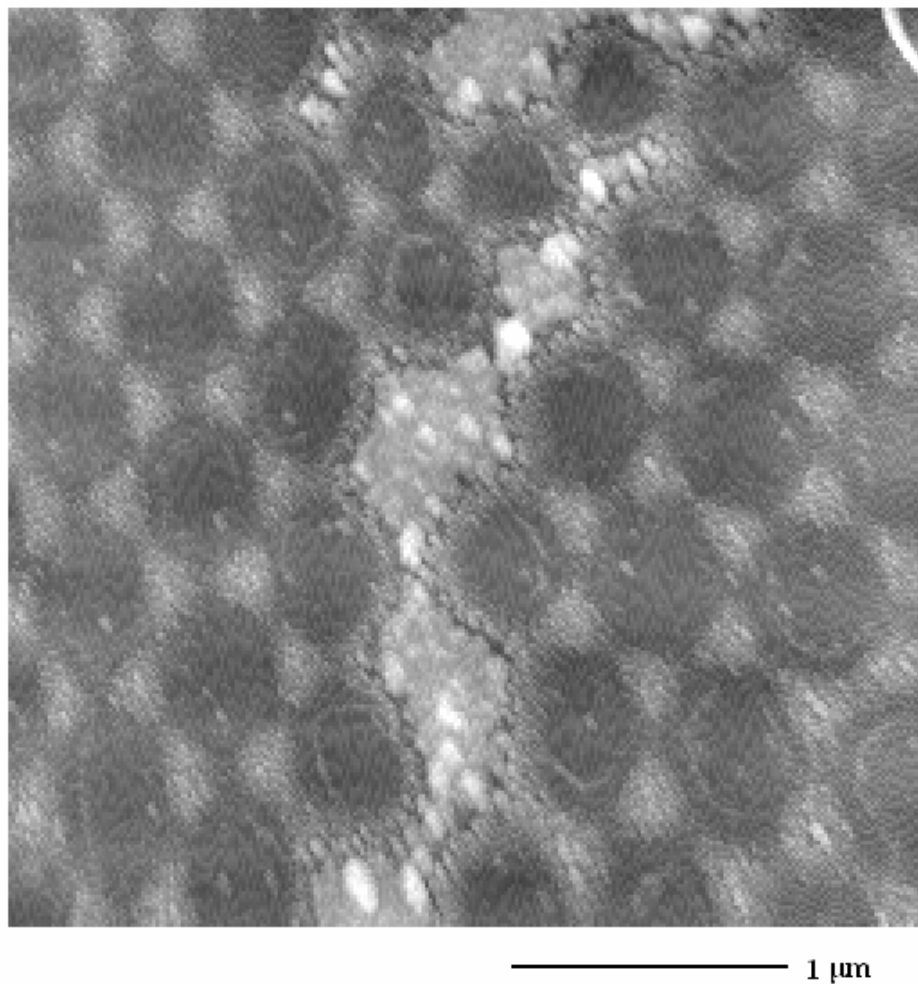


Figure 4.12. Periodic particle array electrochemically deposited through a 600(\pm 20) nm diameter nanosphere template

Similar nanoparticle arrays were also obtained by the technique of vacuum vapor deposition through nanosphere lithography template in Van Duyne's group.^{7,8} The nanoparticle arrays were extensively studied with (localized) surface plasmon resonance spectroscopy. In their method, deposition to the substrate under the sphere layers can happen only to single sphere or double sphere layers. Deposition does not occur on surface areas covered by three or more layers. The resulting particle shapes deposited through single layer and double layer are different from each other. All these limitations, plus the difficulty in fabricating a large area of single polystyrene sphere layer,¹⁴ makes it very difficult to fabricate a large area of uniform particle array.

In our work, because the nanoparticle arrays were fabricated by the electrochemical deposition in a liquid environment, the limitations that confine the technique of vacuum vapor deposition do not apply to our technique. The nanoparticle arrays could be produced through single layer, double or multiple layers of polystyrene spheres. Thus, electrochemical deposition through sphere template provides a novel method that has the potential to fabricate a large area of uniform nanoparticle ensemble.

4.4 Conclusions

Nanosphere templates were fabricated by spin-coating or assembling polystyrene spheres on a layer of gold on mica. Nanopore films of copper, silver, CdSe and ZnO were successfully deposited through nanosphere templates. AFM analysis of the pores shows that the polystyrene sphere in a diameter of 600nm is perfectly spherical, while those in diameter of 1000nm and 3600nm change their shapes after being coated on the substrate. The nanopore film of ZnO on Au substrate constructs an array of recess microelectrodes.

The distance between the microelectrodes is not sufficient for the diffusion to the microelectrodes to be radial. Nanorings were fabricated due to increased copper ion concentration attracted by the negative charges on the surface of the polystyrene sphere. A growth mechanism of the porous film was proposed and supported by two experimental evidences.

Combination of nanosphere lithography and the electrochemical deposition provides a new method that has the potential to fabricate a large area of uniform nanoparticle ensemble.

4.5 References

1. Craighead; H.; Mankiewich; P. *J. Appl. Phys* **1982**, *53*, 7186.
2. McCord; A, M. *J. Vac. Sci. Technol. B* **1997**, *15*, 2125.
3. Dial; O; Cheng; C, C.; A, S. *J. Vac. Sci. Technol. B* **1998**, *16*.
4. Chou; Y, S.; Krauss; R., P.; Zhang; W.; Guo, L.; Zhuang; L. *J. Vac. Sci. Technol. B* **1997**, *15*.
5. Deckman, H. W.; Dunsmuir, J. H. *Appl. Phys. Lett.* **1982**, *41*, 377.
6. Deckman, H. W.; Dunsmuir, J. H. *J. Vac. Sci. Technol., B* **1983**, *1*, 1109.
7. Hulteen, J. C.; Van Duyne, R. P. *J. Vac. Sci. Technol., A* **1995**, *13*, 1553.
8. Hulteen, J. C.; Treichel, D. A.; Smith, M. T.; Duval, M. L.; Jensen, T. R. Van Duyne, R. P. *J. Phys. Chem. B* **1999**, *103*, 3854.
9. Bartlett, P. N.; Ghanem, M. A.; Hallag, I. S. E.; Grootb, P. d.; Zhukov, A. *J. Mater. Chem.* **2003**, *13*, 2596.
10. Abdelsalam, M. E.; Bartleet, P. N.; Baumberg, J. J.; Coyle, S. *Adv. Mater.* **2004**, *16*, 90.
11. Goldeberg, L. M. *Material Science and Engineering C* **2002**, *22*, 233.
12. Briseno, A. L.; Zhou, F. *Langmuir* **2004**, *20*, 219.
13. Whitney, A. V.; Myers, B. D.; Duyne, R. P. V. *Nano Letters* **2004**, *4*, 1507.
14. Ng, V.; Lee, Y. V.; Chen, B. T.; Adeyeye, A. O. *Nanotechnology* **2002**, *13*, 554.
15. Boneberg, J.; Burmeister, F.; Schafle, C.; Leiderer, P. *Langmuir* **1997**, *13*, 7080.
16. Li, N.; Zinke-Allmang, M. *Japanese Journal of Applied Physics, Part 1: Regular Papers, Short Notes & Review Papers* **2002**, *41*, 4626.
17. Fuhrmann, B.; Leipner, H. S.; Hoche, H.-R.; Schubert, L.; Werner, P.; Gosele, U. *Nano letters* **2005**, *5*, 2524.
18. Fan, H.; Fuhrmann, B.; Scholza, R.; Syrowatkab, F.; Dadgar, A.; Krost, A.; Zacharias, M. *J. Cryst. Growth* **2006**, *287*, 34.
19. Park, K. H.; Lee, S.; Koh, K. H.; Lacerda, R.; Teo, K. B. K.; Milne, W. I. *J. Appl. Phys.* **2005**, *97*, 024311.

20. Cheung, C. L.; Nikolic, R. J.; Reinhardt, C. E.; Wang, T. F. *Nanotechnology* **2006**, *17*, 1339.
21. Bartlett, P. N.; Baumberg, J. J.; Coyleb, S.; Abdelsalam, M. E. *Faraday Discuss.* **2004**, *125*, 117.
22. Bartlett, P. N.; Ghanem, M.A.; El Hallag, I. S.; Groot, P. de; Zhukov, A. *J. Mater. Chem.* **2003**, *13*, 2596.
23. Braun, P.V.; Wiltzius, P. *Nature* **1999** *402* 603.
24. Mahajan, S.; Abdelsalam, M.; Suguwara, Y.; Cintra, S.; Russell, A.; Baumberg, J.; Bartlett, P. *Phys. Chem. Chem. Phys.* **2007**, *9*, 104.
25. Takeyasu, N.; Tanaka, T.; Kawata, S. *Jpn. J. Appl. Phys.* **2005**, *44*, 1134.
26. Wittstock, G. *Anal. Bioanal. Chem.* **2002**, *372*, 16.
27. Satjapipat, M.; Sanedrin, R.; Zhou, F. *Langmuir* **2001**, *17*, 7637.
28. Mahajan, S.; Abdelsalam, M.; Suguwara, Y.; Cintra, S.; Russell, A.; Baumberg, J.; Bartlett, P. *Phys. Chem. Chem. Phys.* **2007**, *9*, 104.
29. Boneberg, J.; Burmeister, F.; Schafle, C.; Leiderer, P. *Langmuir* **1997**, *13*, 7080.
30. Sandison, M. E.; Anicet, N.; Glidle, A.; Cooper, J. M. *Anal. Chem.* **2002**, *74*, 5717.
31. Ito, T.; Audi, A. A.; Dible, G. *Anal. Chem.* **2006**, *78*, 7048.
32. Zhao, J.; Brown, W. *Langmuir* **1995**, *11*, 2944.

CHAPTER 5

WIRE CONNECTIONS BETWEEN ANODE AND CATHODE THROUGH DIRECT ELECTRODEPOSITION

5.1 Introduction

The application of nanomaterials in analytical chemistry, especially in life and biomedical science, has attracted increasing attention from researcher in recent years. Nanomaterials provide a new area of developing ultrasensitive, miniaturized biosensors.¹ Nanomaterials have many applications in optical and electrochemical sensors. Recently, nanowires and nanotubes were used to develop a new type of sensor for label-free, direct real-time electric detection of biomolecule binding.²⁻⁴ A typical example is Hahm and Lieber's⁴ "nanowire nanosensor". A single p-type silicon nanowire was installed between two electrically conductive sites on sensor device. Then peptide nucleic acid (PNA) receptors were immobilized on to the surface of the p-type silicon nanowire. The conductance of the silicon nanowire was monitored to detect the binding of PNA and target DNA. The "nanowire nanosensor" exhibited good sensitivity and detection limit. However, this "nanowire nanosensor" has a disadvantage. There is no efficient way to install nanowire on to the sensor device. If the nanowire was created directly between the two electrically conductive sites, the step of immobilizing the nanowire could be avoided.

Electrical contacts between two copper particles were created by Bradley et al.⁵ using directed electrochemical growth. Copper particles placed in an electric field were polarized and each particle contained both anode and cathode poles (Figure 5.1). The oxidation of copper to cupric ions and reduction of water occur at the beginning. After the application of an electric field, the concentration of cupric ions in the interparticle space increases and deposition of copper begins on the particle until a copper wire is formed between the two particles. This discovery has stimulated our interest in exploring the possibility of creating direct connections between anode and cathode.

There has been a tremendous work in fabricating one-dimension (1 D) nanostructures of metals, semiconductors and oxides over the last few years. Synthetic strategies developed for nanowires could be generally classified into the vapor phase growth and the solution-based growth. The vapor phase growth starts with a simple evaporation technique in an appropriate atmosphere to produce elemental or oxide nanowires. The vapor phase growth includes: (1) Vapor–liquid–solid growth; (2) Oxide-assisted growth; (3) Vapor–solid growth and (4) Carbothermal reactions.⁶⁻⁸

Solution-based growth achieves nanowires through anisotropic growth dictated by the crystallographic structure of the solid material, confined and directed by templates, kinetically controlled by supersaturation, or by the use of an appropriate capping agent. Some materials, such as polysulphurnitride, selenium, tellurium and molybdenum chalcogenides, can easily form nanowires due to their anisotropic bonding in structure. An anisotropic bonding causes the crystallization to occur along the c-axis. Template-based synthesis is a versatile way to fabricate nanowires. The usual templates are porous

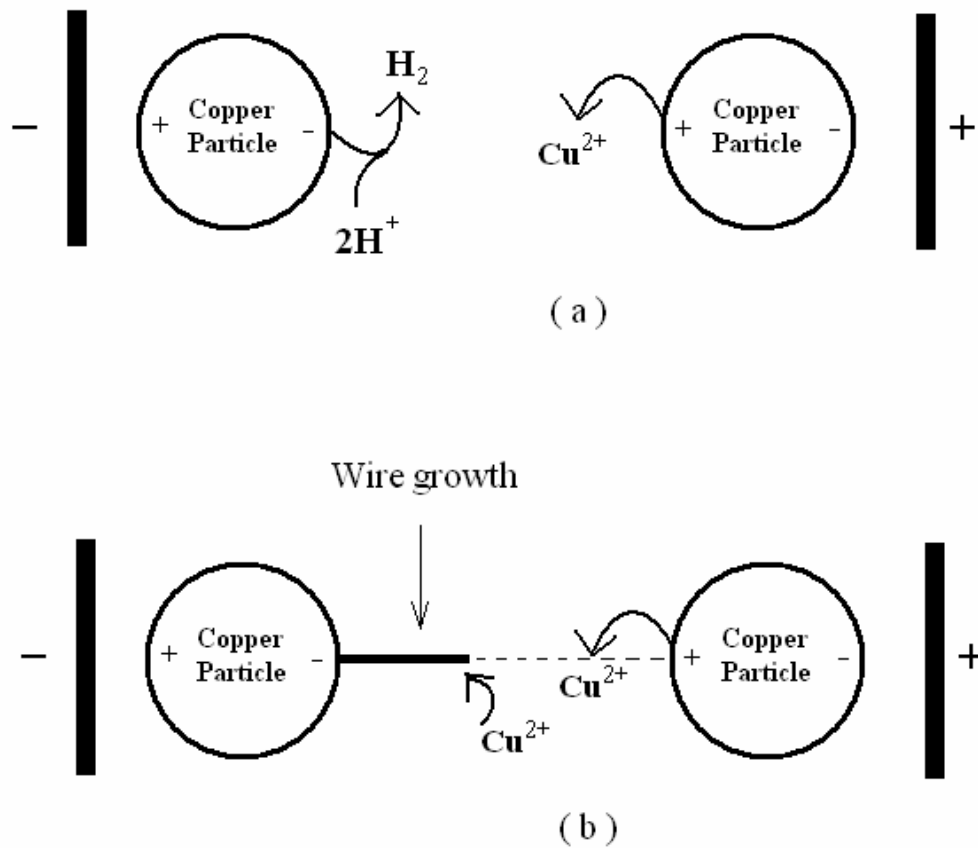


Figure 5.1. Diagram of wire formation between two particles under bipolar conditions. (a) Two copper particles are placed in an aqueous environment and an electric field is applied. The copper particles are polarized. Initially, particles on the right of the diagram release cupric ions while particles on the left reduce water. (b) When the concentration of cupric ions near the left-hand particle is high enough for electrodeposition, copper wire starts to grow on the negative-charged side of the left-hand particle. The process of the wire growth in the interparticle region continues until the two particles are connected.

alumina and polycarbonate membranes. After the channels in the templates are filled with target species, the matrix is removed with the nanowires left behind. The nanowires made from this method are usually amorphous. A third method, solution–liquid–solid process, is able to generate single-crystalline nanowires. The last method in the solution-based growth of nanowires is the solvent thermal methodology. In this method, a mixture of solvent, metal precursors and crystal regulating agent is placed in a condition with specific temperatures and pressures to carry out crystal growth.⁹⁻²⁹

In the present study, we try to create connections of micro-/nanowire between cathode and anode using electrochemical growth and to understand the reactions of the electrochemical deposition.

5.2 Experimental

Chemicals. All chemicals were purchased from Sigma-Aldrich of reagent quality and were used without further purification. All solutions were prepared using reagent grade water (18.2 M Ω cm) from a Barnstead “NANO infinity” ultrapure water system.

Electrochemistry. All electrochemistry experiments were carried out using a BAS Epsilon Potentiostat workstation. A conventional three electrode configuration was employed and all cell components were constructed from either Teflon or Kel-F. Ag|AgCl(sat) was the reference electrode. The working and counter electrodes were custom made from metal wires by polishing.(Figure 5.2)

5.3 Results and Discussion

5.3.1 Growth of copper wire between copper-copper electrodes

Figure 5.2 shows the diagram of wire growth between the two copper electrodes. The custom-made copper working electrode and counter electrode (the two electrodes were aligned in a straight line) were placed in a solution containing 0.1 M CuSO₄ and Na₂SO₄. When a potential between 0.0 V and -0.3 V vs Ag|AgCl(sat) was applied to the working electrode, a video recording showed that copper began to deposit on the working electrode and the copper wire grew in a direction from the working electrode to the counter electrode until contact was made on counter electrode. The chronoamperometric curve of the growing process is shown in Figure 5.3. Initially, the chronoamperometric curve shows normal electrochemical deposition behavior. After around 670 seconds of deposition, the current increased from around 1.5mA to the maximum limit, which was set to 10mA. This dramatic increase of current is an indicator of the connection between the two electrodes by copper wire. The SEM image shown in Figure 5.4 confirmed the connection of the two copper electrodes. From the figure, we can see that the gap between the two electrodes is 50μm and the diameter of the wire grown is around 25μm.



The electrochemical reaction occurs on the working electrode is the reduction of cupric ions from solution to metal copper, as is shown in formula 5.1. The reaction at the counter electrode may be the oxidation of copper or water. The potential measured at counter electrode was between 0.17 V and 0.35 V vs Ag|AgCl(sat). Since the standard

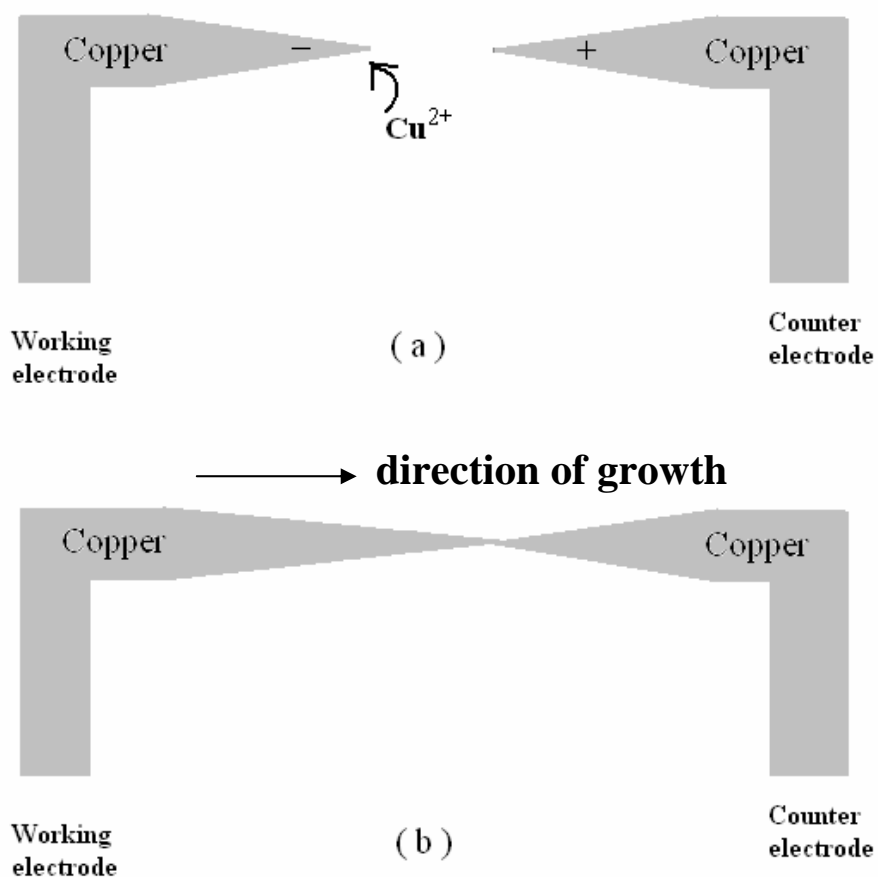


Figure 5.2. Diagram of wire formation between two copper electrodes. (a) Two copper electrodes are placed in a solution containing 0.1 M CuSO_4 and Na_2SO_4 . Cupric ion from the solution are reduced and deposited at the working electrode. (b) Two copper electrodes are connected.

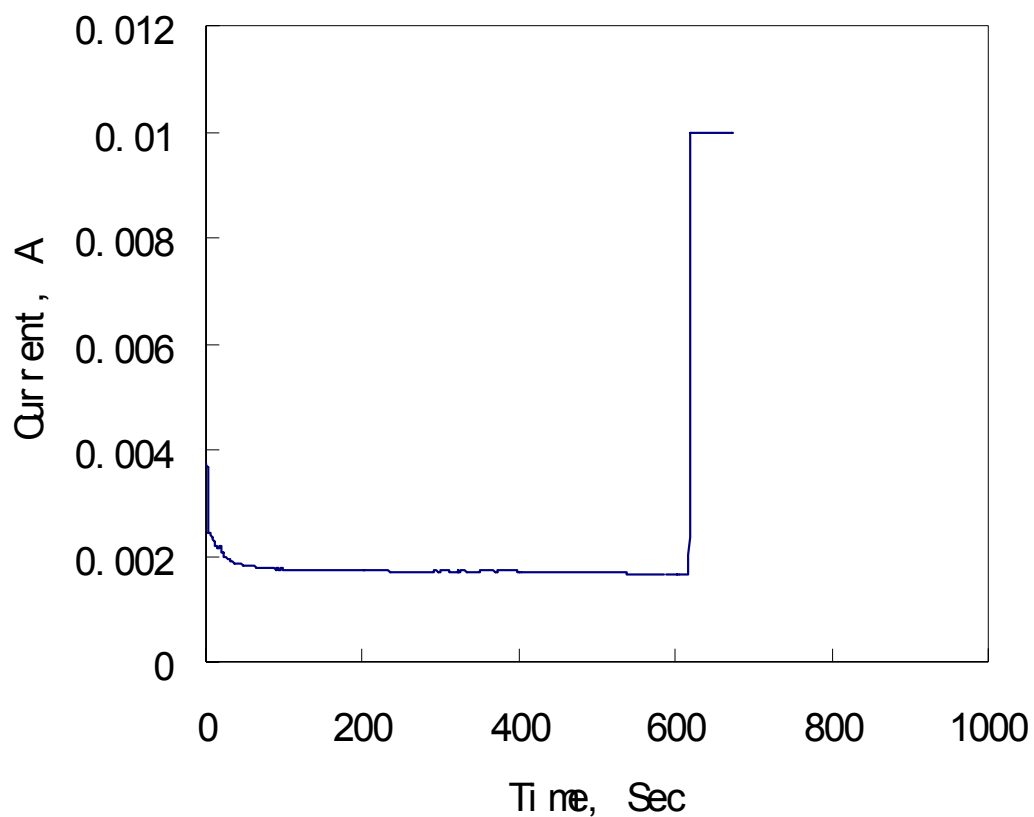


Figure 5.3 Chronoamperometric curve of copper wire growth between copper-copper electrodes in a solution containing 100 mM CuSO_4 and 100 mM Na_2SO_4 supporting electrolyte. Potential applied is -0.2 V vs $\text{Ag}|\text{AgCl}(\text{sat})$. The drastic current increase at 670 second is due to the connection between anode and cathode.

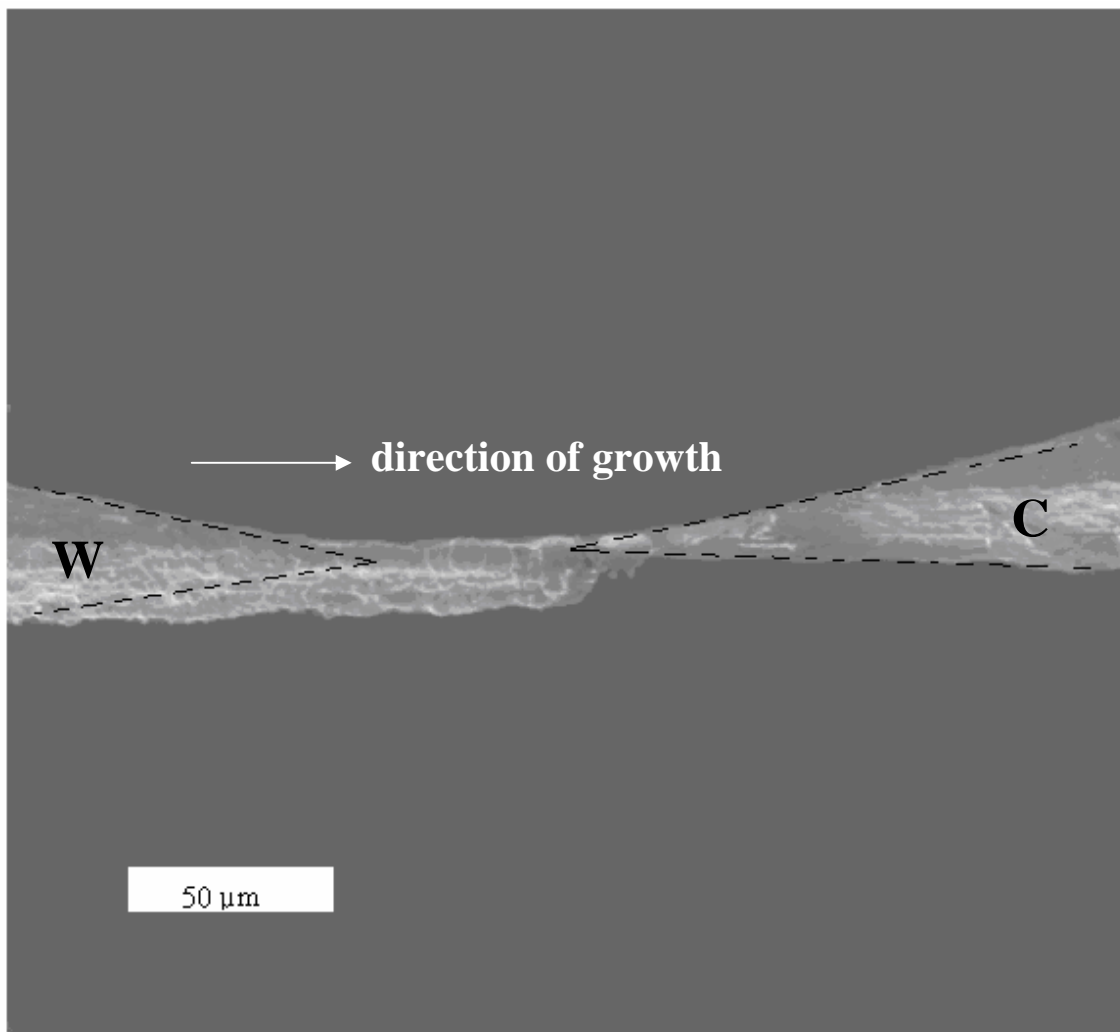


Figure 5.4. SEM image of the copper wire grown between two copper electrodes in a solution 100mM CuSO_4 and 100mM Na_2SO_4 supporting electrolyte. The dashed lines represent the original position of the electrodes before electrodeposition. Wire grew from working electrode (left) to counter electrode (right).

oxidation potential of water (1.23V) is much higher than the potential at counter electrode, the oxidation of water is not likely to happen. The half reaction on the counter electrode is the oxidation of copper, which is shown in formula 5.2.

5.3.2 Growth of other wires between copper-copper electrodes

To verify that the proposed reaction happens at the counter electrode, silver wire and CdSe wire were electrochemically deposited between the copper-copper electrodes.

The experimental setup is same as shown in Figure 5.2. The potential and solution for deposition is listed in Table 5.1.

Table 5.1. Experimental conditions of electrochemical deposition.

species	Potential vs Ag AgCl(sat)	solution
CdSe	-600 mV	200mM CdSO ₄ , 1mM SeO ₂ , 50mM HClO ₄
Cu	-300~0 mV	100mM CuSO ₄ , 100mM Na ₂ SO ₄
Ag	0 mV	5mM AgNO ₃ , 100mM NaNO ₃
Ag	Open circuit	5mM AgNO ₃ , 100mM NaNO ₃ , 10 mM HClO ₄

In neutral plating solution, the process for depositing silver with a potential of 0 mV is fast relative to the one for copper. As shown in Figure 5.5, the connection was created within several minutes. The appearance of the silver wire was similar to the copper wire shown in Figure 5.4. The elemental composition of the deposited wire was analyzed with EDS. In Figure 5.6, a strong silver peak was observed.

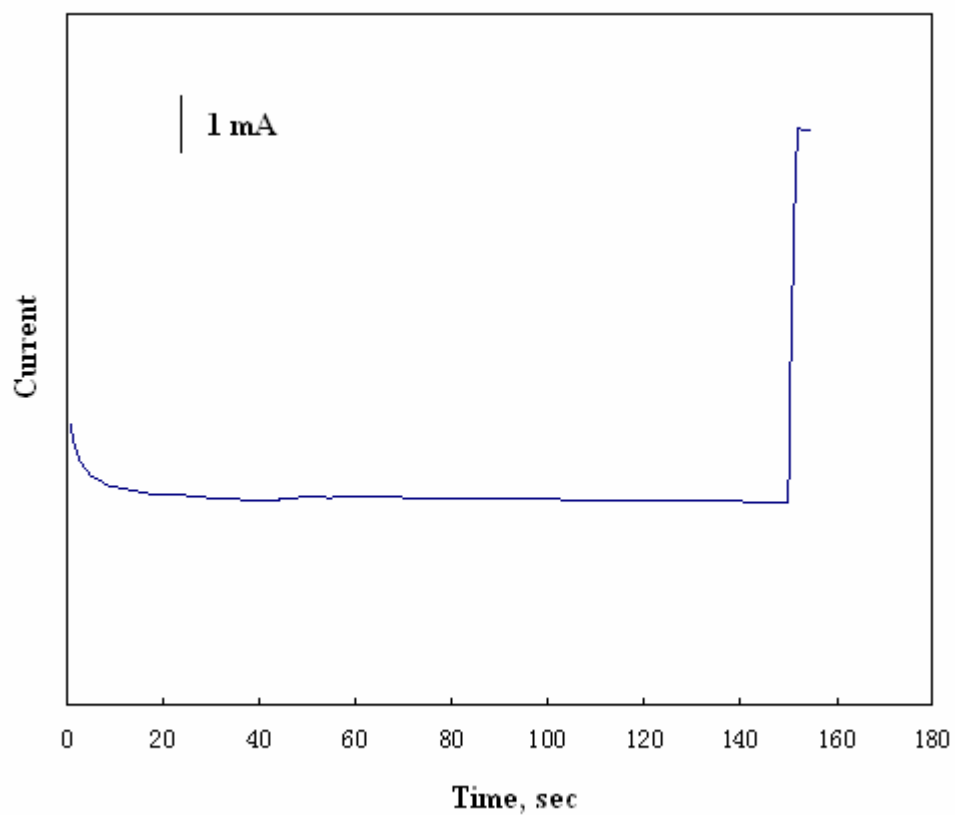


Figure 5.5. Chronoamperometric curve of Ag wire growth between copper-copper electrodes in a solution containing 5 mM AgNO₃ and 100 mM NaNO₃. Potential applied is 0 V vs Ag|AgCl(sat). Connection happened after depositing for around 150 second.

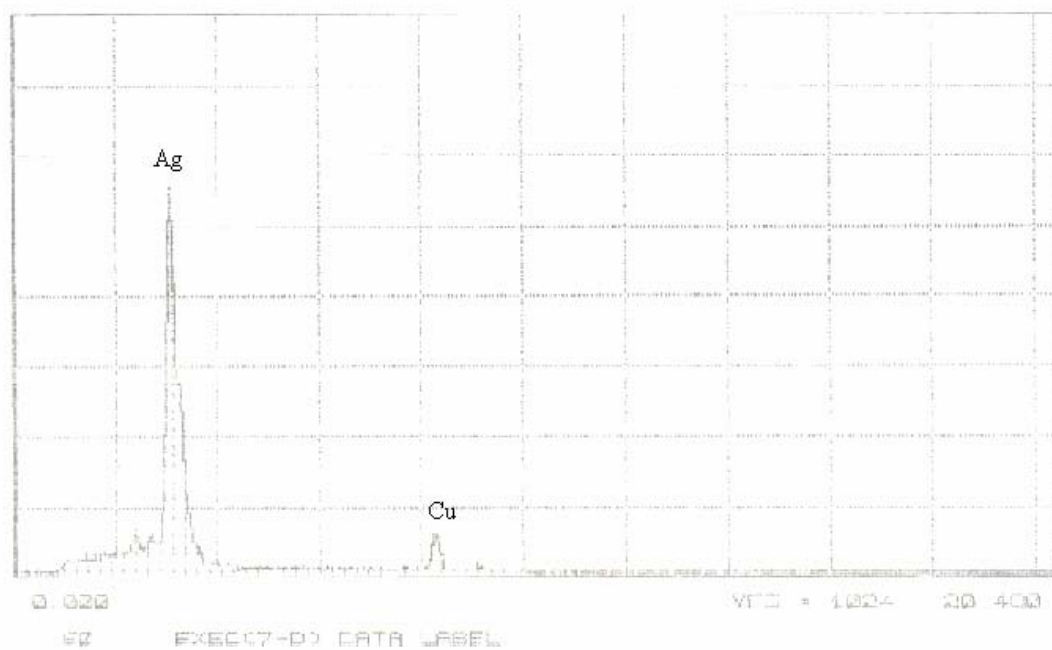


Figure 5.6. EDS of the wire deposited between copper-copper electrodes in a solution containing 5 mM AgNO_3 and 100 mM NaNO_3 . Potential applied is 0 V vs $\text{Ag}|\text{AgCl}(\text{sat})$.

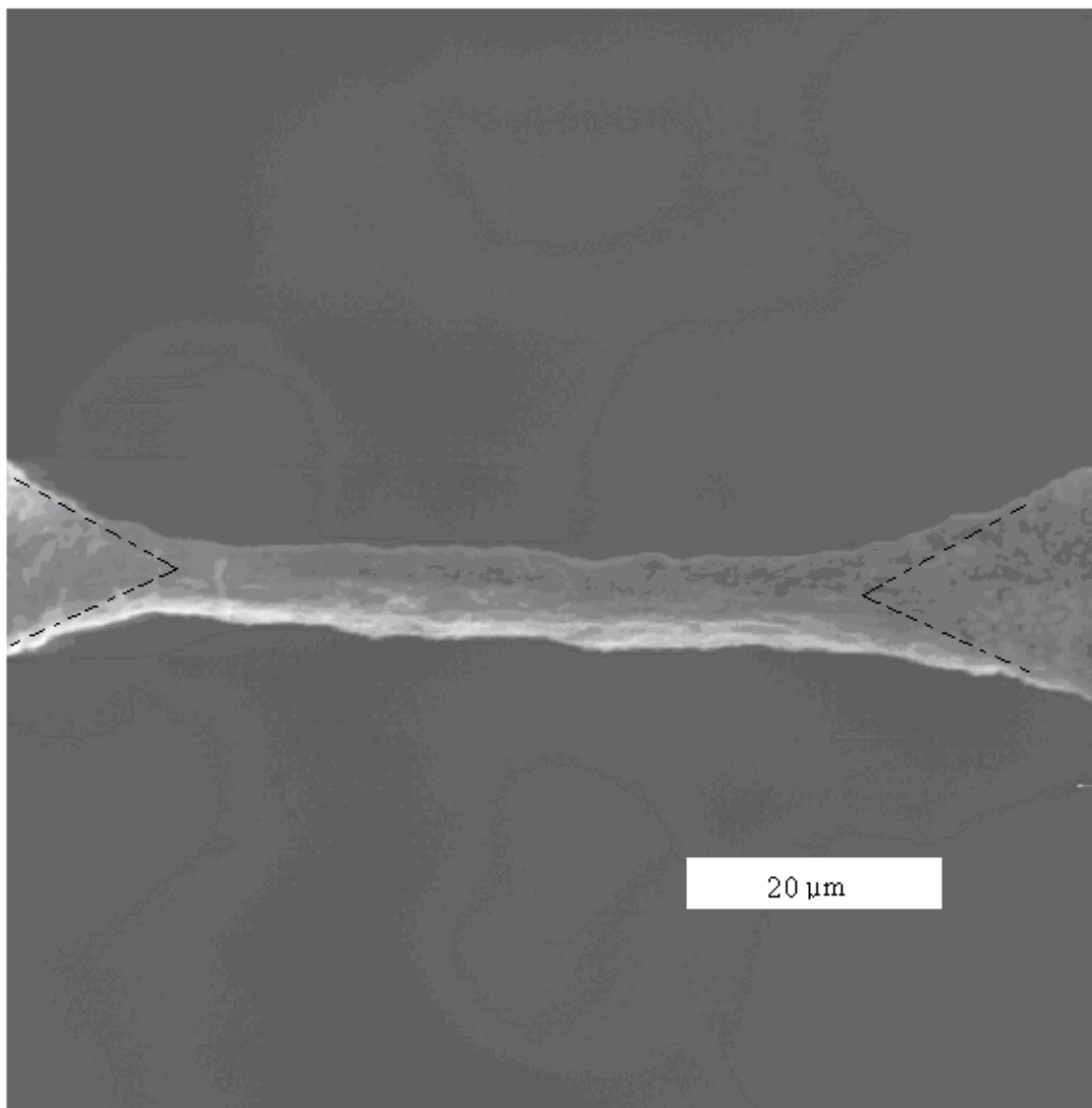


Figure 5.7 SEM image of the silver wire between two copper electrodes grown at open circuit in a solution containing 5 mM 100 mM NaNO_3 and 100 mM H_2SO_4 . The dashed lines represent the original position of the electrodes before electrodeposition.

In an acidic condition (pH=1.0), silver deposition took place at open circuit. An SEM image illustrating silver wire deposited at open circuit is shown in Figure 5.7. The wire in the image does not have the joint. The diameter of wire is around 10 μm .

CdSe, a semiconductor wire was also created between copper-copper electrodes (Figure 5.8). The current was still within the detection limit after the connection of CdSe between anode and cathode was created, indicating that CdSe wire have higher resistance than copper or silver wires made in this work.

Figure 5.9 shows the EDS of the wire deposited between copper-copper electrodes in a solution containing 200mM CdSO_4 , 1mM SeO_2 and 50mM HClO_4 . Besides the cadmium and selenium peaks, a very strong copper peak was observed, indicating the wire contains a significant amount of copper.

5.3.3 Growth of copper wires between copper-gold electrodes

If the copper counter electrode was substituted with gold wires and the working electrode remained to be copper, the deposition of copper on the working electrode was observed at a potential of -0.2V vs $\text{Ag}|\text{AgCl}(\text{sat})$ in a solution containing 100mM CuSO_4 and 100mM Na_2SO_4 supporting electrolyte. However, the wire connection between anode and cathode was not always created. The failure of connection-creating maybe primarily due to stirring caused by the large amount of gas produced on gold counter electrode. The pH measurement of the aqueous solution showed that the pH decreased as the electrochemical deposition time increase, indicating that the concentration of H^+ increased.

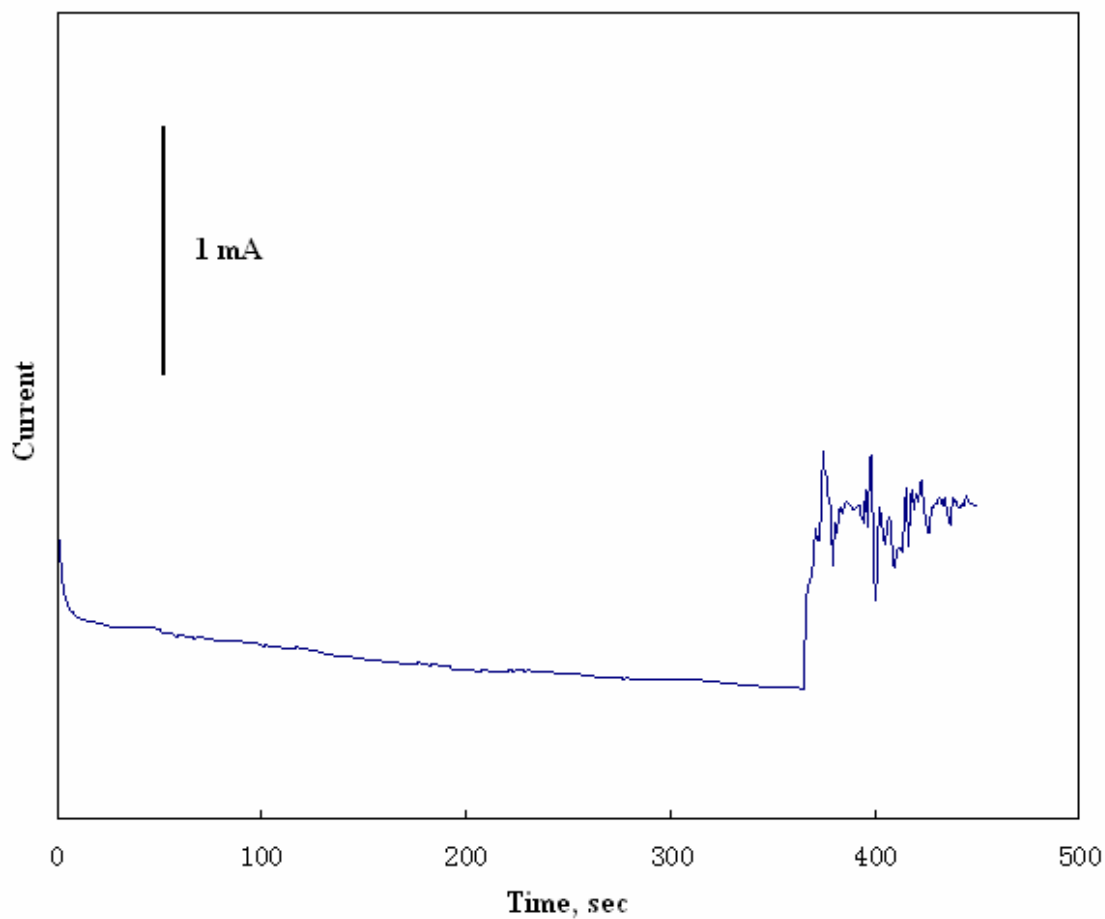


Figure 5.8. Chronoamperometric curve of wire growth between copper-copper electrodes in a solution containing 200 mM CdSO₄, 1 mM SeO₂ and 50 mM HClO₄. Potential applied is -0.6 V vs Ag|AgCl(sat).

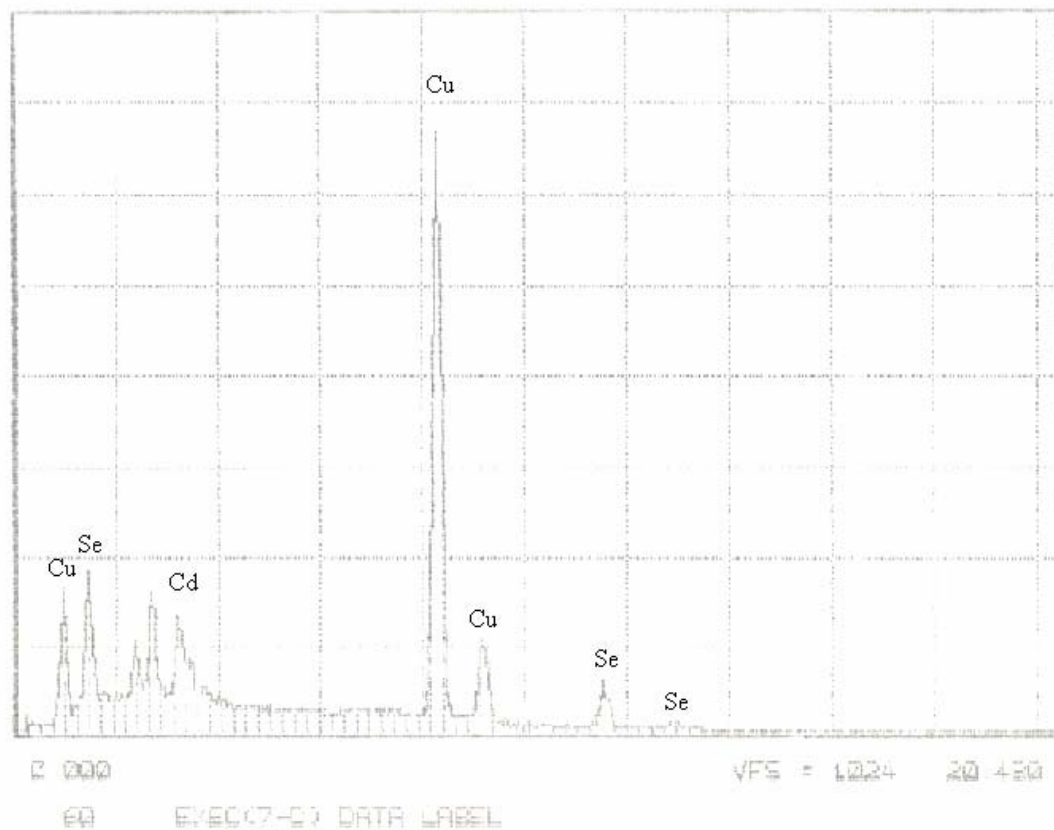


Figure 5.9. EDS of the wire deposited between copper-copper electrodes in a solution containing containing 200 mM CdSO₄, 1 mM SeO₂ and 50 mM HClO₄. Potential applied is -0.6 V vs Ag|AgCl(sat).

If a gold electrode pre-deposited with an amount of copper was used as counter electrode, as the copper wire grew on the working electrode, no gas was produced on the counter electrode before the copper on the gold counter electrode was used up. After that, the gas production starts again. According to our observation, the total charge of copper deposited on copper working electrode is same with the total charge of the copper pre-deposited on gold counter electrode.

Table 5.2. Charge of copper deposited

Charge of copper deposited on copper working electrode, Coulomb	Charge of copper pre-deposited on gold counter electrode, Coulomb
1.234	1.276
2.371	2.398

For the case when counter electrode was copper and working electrode was other metal such as gold and nickel, the copper, silver and CdSe wires were successfully created between the two electrodes. These results demonstrate that when copper is used as counter electrode, the copper on counter electrode dissolves as the wire grows on the various working electrodes. It is expected that other metals can be used as counter electrode for the creation of copper wire connecting two electrodes when the metal an dissolve at an potential less positive than the water oxidation potential

5.3.4. Resistance of CdSe wire in aqueous solution containing electrolytes

Hahm and Lieber⁴ have pointed out that the conductance of p-type silicon nanowire increase as the negative surface charge density increase. The CdSe wires

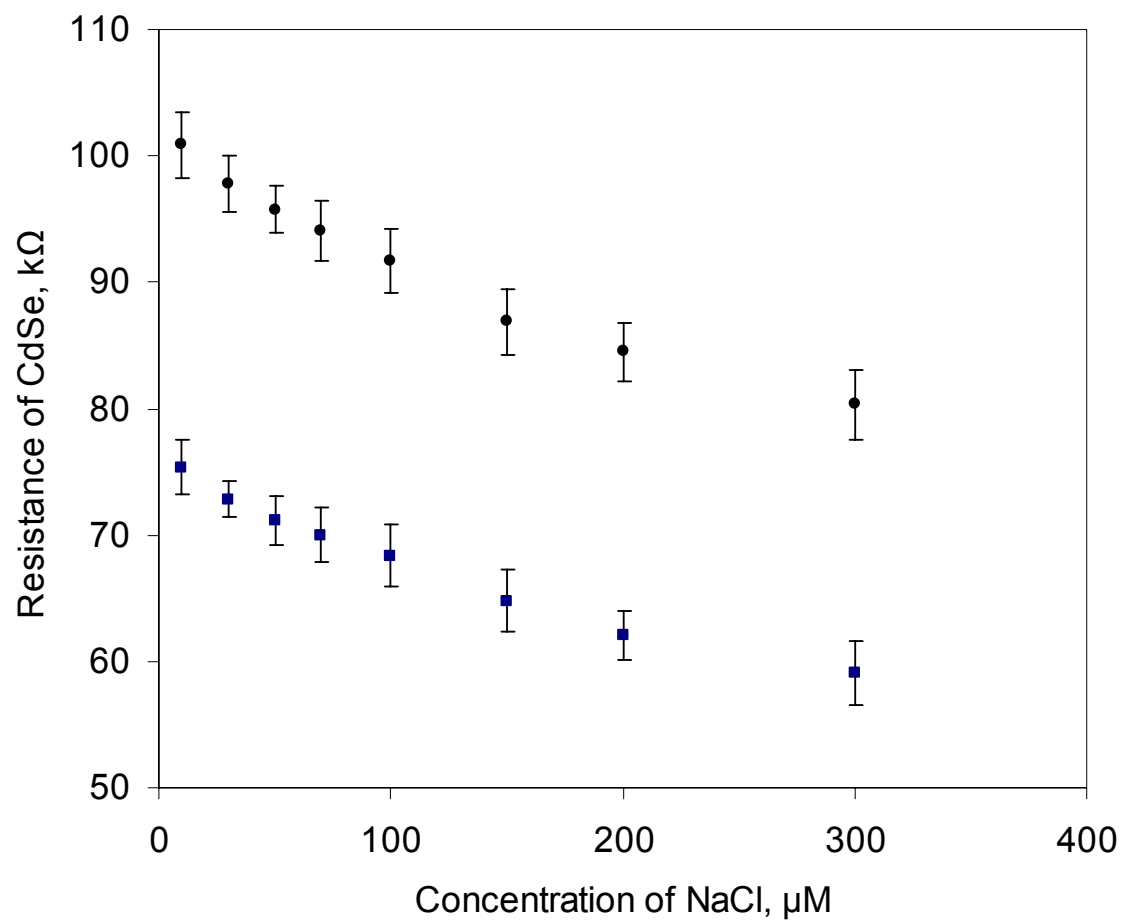


Figure 5.10. Plot of resistance of CdSe wire as a function of the concentration of NaCl in a solution containing 10mM NaNO₃.

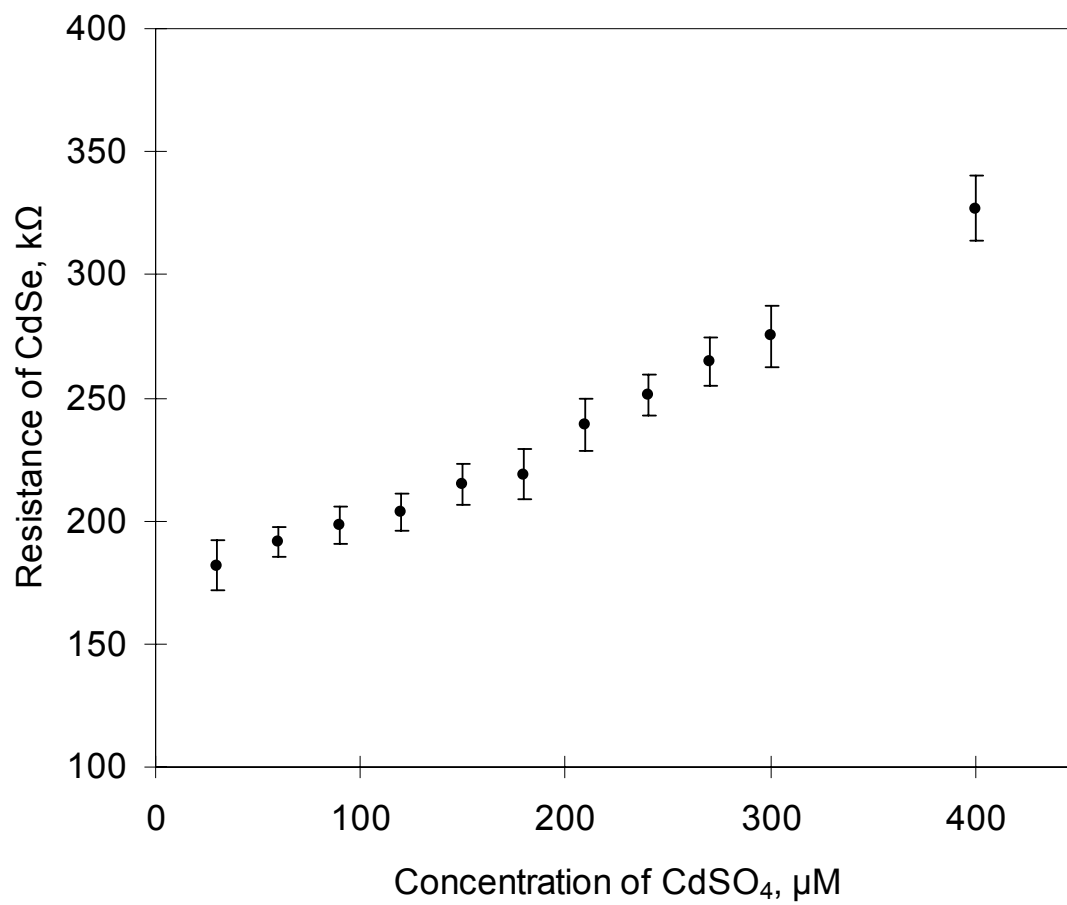


Figure 5.11. Plot of resistance of CdSe wire as a function of the concentration of CdSO₄ in a solution containing 10mM NaNO₃.

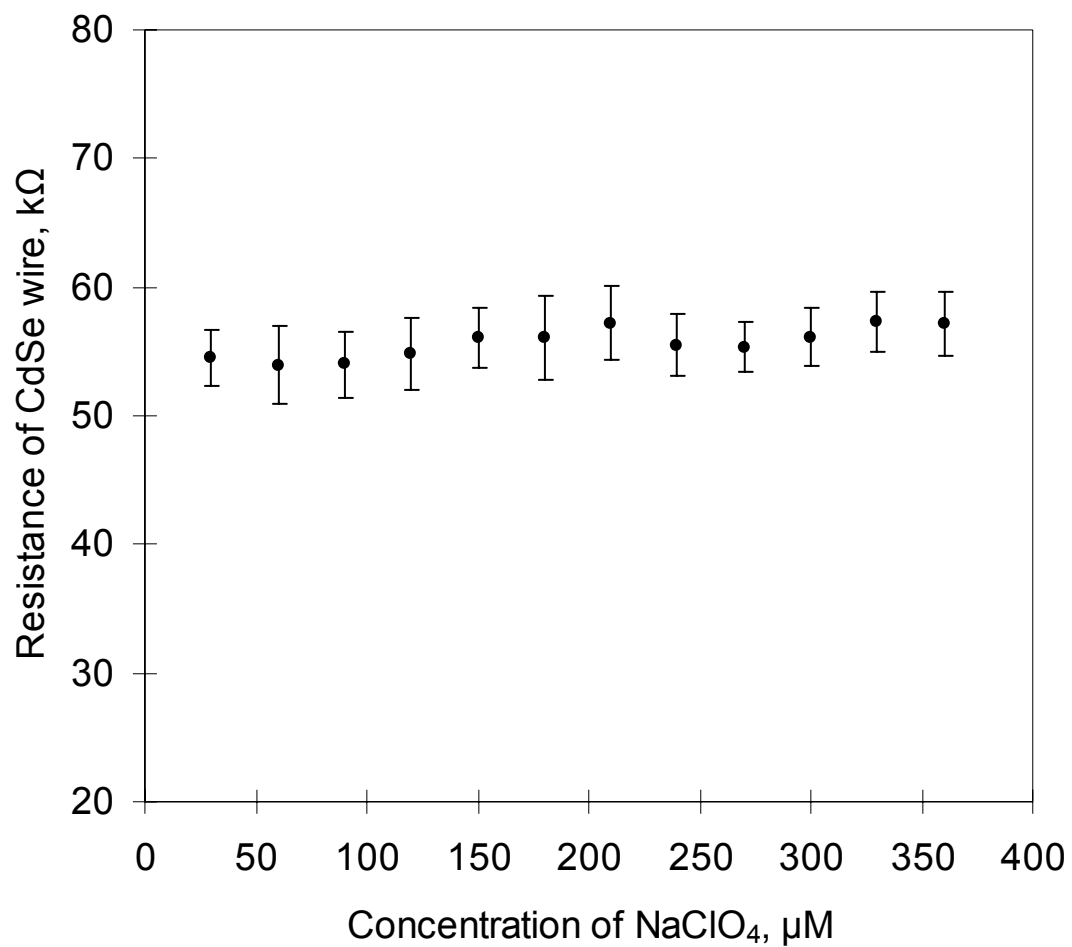


Figure 5.12. Plot of resistance of CdSe wire as a function of the concentration of NaClO₄ in a solution containing 10mM NaNO₃.

created in this work were immersed in a solution containing 10mM of NaNO₃. The resistance of the CdSe wire was monitored with a multimeter as a selected electrolyte was added into the solution. After each addition, the maximum and minimum values in 60 seconds were recorded. The average of the two values was regarded as the resistance of the CdSe wire after the addition of electrolyte. The experimental results (not shown) illustrated that the resistance of CdSe wire remained constant (change < 5%) in 10 mM NaNO₃ over 24 hours. Figure 5.10 to 5.12 shows the plots of resistance of CdSe wire as a function of the concentration of NaCl, CdSO₄ and NaClO₄ in a solution containing 10mM NaNO₃. The resistance of CdSe wire in Figure 5.10 decreased as the concentration of NaCl increased. The two curves were measured from two CdSe wires. Figure 5.10 show that the two CdSe wires have similar response to NaCl in the solution of 10mM NaNO₃. The average resistance changes were -68.5 Ω (curve (a)) and -54.5 Ω (curve (b)) for an increase of 1 μM in the concentration of NaCl. In Figure 5.11, the resistance of CdSe wire increased as the concentration of CdSO₄ increased. While the resistance of CdSe wire did not change significantly with the increase of the concentration of NaClO₄, as is shown in Figure 5.12. The different behavior of CdSe wire in the three electrolytes may be explained by the capability of ions to adsorb onto the surface of CdSe wire. As shown in Figure 5.13. A p-type of CdSe semiconductor wire was codeposited in our experimental condition (Figure 5.13a).²⁹ In NaCl solution, the chlorine anion which carries negative charges could adsorb on to the surface of CdSe wire. The chlorine anion acted as a negative gate (Figure 5.13b) and caused a decrease in the resistance of the CdSe wire. On the contrary, the resistance of the CdSe wires increase in the solution of CdSO₄ because that the adsorbed cadmium cation carrying positive charge acted as

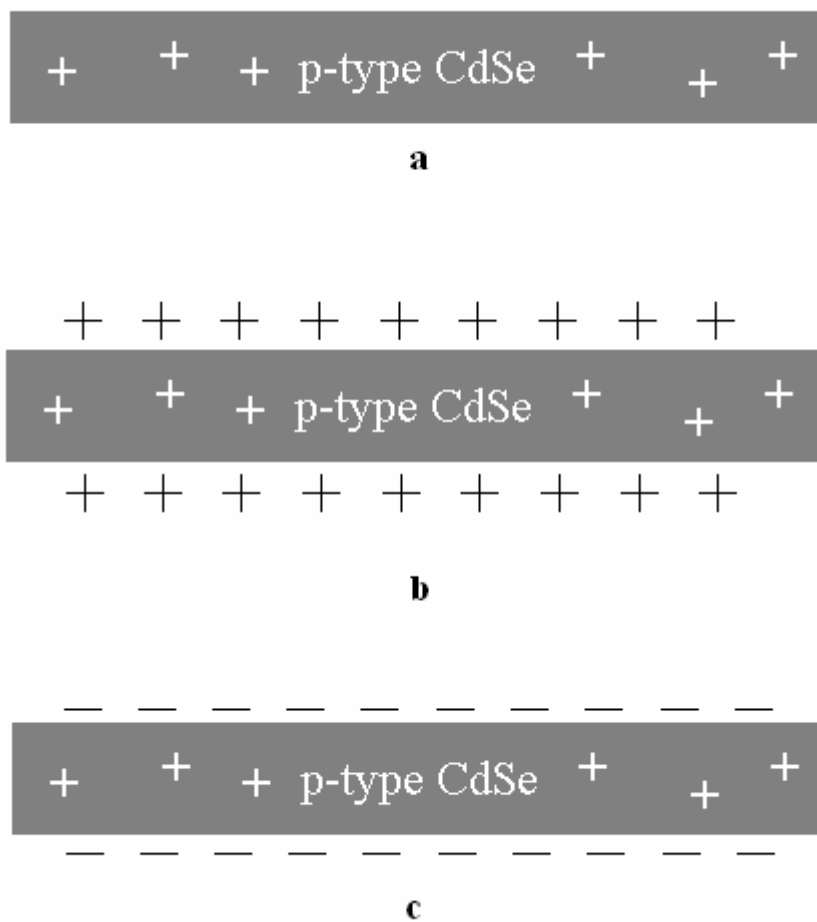


Figure 5.13. Specific adsorption leads to changes in surface charge and electrical properties of the nanowires. (a) Electrochemical codeposition of p-type CdSe. (b) Adsorption of cations: positive ‘gating’ of p-type CdSe leads to depletion of hole carriers and higher resistance. (c) Adsorption of anions: conversely, negative ‘gating’ of p-type CdSe leads to lower resistance.

positive gate (Figure 5.13c) on to the surface of CdSe wire. As for NaClO₄, either anion or cation doesn't have preference in adsorbing on to the surface of CdSe wire, the resistance of the CdSe wire doesn't increase or decrease significantly.

5.4 Conclusions

A novel method of microwire fabrication was introduced, which are expected to boost the development of sensors that are based on the micro-/nanowires. The connections of copper, silver and CdSe wire between copper anode and cathode were successfully created. Experimental results have shown that the reaction at copper counter electrode was the oxidation of copper. If other metals, such as gold and nickel, were used for the working electrode and if copper was used as the counter electrode, the wire connection between the two electrodes could be created. When gold were used as counter electrode, the reaction on the counter electrode is the oxidation of water. The gas produced could form a protection layer that prevents the wire from reaching the counter electrode. The connection between anode and cathode become less possible. The diameter of the wire created could reach less than 10 μ m. The resistance of the CdSe wires created in this work was sensitive to the variation of charge density adsorbed on to surface.

5.5 References

1. Gasparac, R.; Taft, B. J.; Lapierre-Devlin, M. A.; Lazareck, A. D.; Xu, J. M.; Kelley, S.O. *J. Am. Chem. Soc.* **2004**, *126*, 12270.
2. Star, A.; Gabriel, J-C. P.; Bradley, K.; Gruner G. *Nano Lett.* **2003**, *3*, 459.
3. Murray, B. J.; Newberg, J. T.; Walter, E. C.; Li, Q.; Hemminger, J. C. Penner, R. M. *Anal. Chem.* **2005**, *77*, 5205.
4. Hahm, J.; Lieber, C. M. *Nano Lett.* **2004**, *4*, 52.
5. Bradley, J.J.; Chen, H-M.; Crawford, J.; Eckert, J.; Ernazarova, K.; Kurzeja, T.; Lin, M., McGee, M.; Nadler, W.; Stephens, S.G. *Nature*, **1997**, *389*, 268.
6. Wu, Y.; Yang, P. *J. Am. Chem. Soc.* **2001**, *123*, 3165.
7. Wang, N; Tang, Y.H.; Zhang, Y.F.; Lee, C.S.; Lee, S.T. *Phys. Rev. B* **1998**, *58*, R16024.
8. Stejny, J.J.; Trinder, R.W.; Dlugosz, J. *J. Mater. Sci.* 1981, *16*, 3161.
9. Stejny, J.J.; Dlugosz, J. J.; Keller, A. *J. Mater. Sci.* **1979**, *14*, 1291.
10. Gates, B.; Mayers, B.; Cattle, B.; Xia, Y. *Adv. Funct. Mater.* **2002**, *12*, 219.
11. Mayers, B.; Xia, Y. *J. Mater. Chem.* **2002**, *12*, 1875.
12. Song, J.; Messer, B.; Wu, Y.; Kind, H.; Yang, P. *J. Am. Chem. Soc.* **2001**, *123*, 9714.
13. Messer, B.; Song, J.H.; Huang, M.; Wu, Y.; Kim, F.; Yang, P. *Adv. Mater.* **2000**, *12*, 1526.
14. Song, J.; Messer, B.; Wu, Y.; Kind, H.; Yang, P. *J. Am. Chem. Soc.* **2001**, *123*, 9714.
15. Martin, C.R. *Science* **1994**, *266*, 1961.
16. Zheng, M.; Zhang, L.; Zhang, X.; Zhang, J.; Li, G. *Chem. Phys. Lett.* **2001**, *334*, 298.
17. Xia, Y.; Yang, P.; Sun, Y.; Wu, Y.; Mayers, B.; Gates, B.; Yin, Y.; Kim, F.; Yan, H. ; *Adv. Mater.* **2003**, *15*, 353.
18. Rao, C.N.R.; Govindaraj, A.; Deepak, F.L.; Gunari, N.A.; Nath, M. *Appl. Phys. Lett.* **2001**, *78*, 1853.

19. Govindaraj, A.; Deepak, F.L.; Gunari, N.A.; Rao, C.N.R. *Israel J. Chem.* **2001**, *41*, 23.
20. Yin, Y.; Lu, Y.; Sun, Y.; Xia, Y. *Nano Lett.* **2002**, *2*, 427.
21. Gates, B.; Wu, Y.; Yin, Y.; Yang, P.; Xia, Y. *J. Am. Chem. Soc.* **2001**, *123*, 11500.
22. Govindaraj, A.; Satishkumar, B.C.; Nath, M.N.; Rao, C.N.R. *Chem. Mater.* **2000**, *12*, 202.
23. Trentler, T.J.; Hickman, K.M.; Geol, S.C.; Viano, A.M.; Gibbons, P.C.; Buhro, W.E. *Science* **1995**, *270*, 1791.
24. Trentler, J.J.; Goel, S.C.; Hickman, K.M.; Viano, A.M.; Chiang, M.Y.; Beatty, A.M.; Gibbons, P.C.; Buhro, W.E. *J. Am. Chem. Soc.* **1997**, *119*, 2172.
25. Markowitz, P.D.; Zach, M.P.; Gibbons, P.C.; Penner, R.M.; Buhro, W.E. *J. Am. Chem. Soc.* **2001**, *123*, 4502.
26. Holmes, J.D.; Johnston, K.P.; Doty, R.C.; Korgel, B.A. *Science* **2000**, *287*, 1471.
27. Manna, L.; Scher, E.C.; Alivisatos, A.P. *J. Am. Chem. Soc.* **2000**, *122*, 12700.
28. Rao, C.N.R.; Deepak, F.L.; Gundiah G.; Govindaraj, A. *Prog. Solid State Chem.* **2003**, *31*, 5.
29. a) Gal, D.; Hodes, G. *J. Electrochem. Soc.* **2000**, *147*, 1825. (b) Singh, K.; Upadhyay, D. N.; Pandey, V. K. *Indian J. of Chem.*, **1989**, *28A*, 832.

CHAPTER 6

CONCLUSIONS AND FUTURE WORK

In this work, we have studied the temperature dependence of the underpotential deposition of mercury onto Au(111) electrodes and several methods of micro/nanofabrication in the purpose of being applied in analytical chemistry. In chapter 2, we have studied the temperature dependence of the underpotential deposition (upd) of mercury(II) onto Au(111) electrodes from a series of electrolytes in which anion interactions could be varied from essentially zero (i.e., HClO₄) to strongly interacting with either the Au(111) substrate (i.e., H₂SO₄) or with solution phase Hg²⁺ ions (i.e., HC₂H₃O₂). Isothermal cell was used to make temperature-dependent cyclic voltammetry measurements. Analysis of the temperature dependent cyclic voltammetric curves at a constant surface coverage of Hg yielded values for the half-reaction entropy and enthalpy, $\Delta S^0(\text{upd})$ and $\Delta H^0(\text{upd})$, for the Hg upd reaction. $\Delta S^0(\text{upd})$ values of -30.9 and -18.3 J/mol K were measured for perchloric acid and sulfuric acid electrolytes, respectively. The respective $\Delta S^0(\text{upd})$ values for these electrolytes were -182 and -184 kJ/mol. In acetic acid media, thermodynamic functions were found to depend on the electrolyte pH. $\Delta S^0(\text{upd})$ increased monotonically from $+16.4$ to $+83.5$ J/mol K as the pH was increased from 2.7 to 5.3 at a constant formal acetate concentration of 0.10 M. Under the same experimental conditions, $\Delta H^0(\text{upd})$, increased from -150 to -102 kJ/mol.

The chapter 3 and chapter 4 introduced the fabrications of nanoelectrode arrays using electrochemistry method coupled with the techniques of self-assembled monolayer and nanosphere lithography. In chapter 3, the 4-ATP/DT mixed SAMs were studied and it was revealed that DT can assemble more strongly on gold surface than 4-ATP under the experimental condition. The comparison of electropolymerization of aniline on bare gold electrode and 4-ATP-modified gold electrode disclosed that aniline electropolymerization happened on 4-ATP modified gold electrode when cycling between 0 and 0.8 V was induced by the cation radical of 4-ATP. AFM images show that polyaniline deposited on the two-component mixed SAM of 4-ATP and DT displays a random array of nanoelectrodes. The polyaniline nanoelectrode arrays were characterized with electrochemistry and theoretical simulations were carried out on these nanoelectrode arrays. The theoretical fitting values of density and radius were in good agreement with the experimental values. An affinity antibody/antigen based biosensor using polyaniline nanoelectrode array demonstrated that the biosensor using nanoelectrode array has an increased antibody-polyaniline binding efficiency comparing to that using macroelectrode. In chapter 4, nanopore and nanoparticle arrays were fabricated using nanosphere templates. The profiles of the pore were investigated and used to evaluate the shape deform of polystyrene sphere in the template. The nanopore arrays were characterized by cyclic voltammetry. The growth process of nanopore was studied, and a mechanism was proposed and supported by two experimental evidences. Experimental results showed that the electrochemical deposition coupled with nanosphere lithography provides a new simple method to fabricate the triangular particle array with a large In the future works, more applications are expected on these regular and random arrays. For

example, both nanopore arrays and the polyaniline nanoelectrode arrays could be used in Myler's work.¹ Aniline/biomolecules may polymerized on the exposed gold areas in nanopores or on 4-ATP "islands" to fabricate the enzymatic sensors. The enhanced sensitivities and lower detection limits are anticipated from these sensors. In addition, the characterization of the nanopore arrays may be extended to explore their applications in other areas, for example, optical sensors.

In chapter 5, a novel method of microwire fabrication was discussed. Microwires of copper, silver and CdSe were successfully created between two copper electrodes. Preliminary tests have shown that the resistance of the CdSe wire created in our work was sensitive to the variation of charge density adsorbed on to surface. The following may be the directions of future works: 1) to fabricate more metals and semiconductors wires; 2) minimized the diameter of the microwire to a nanometer range; 3) to improve the durability of microwires created between two electrodes so that one sample could be used for multi-times; 4) better instruments be used to measure the resistance of microwires to improve accuracy; 5) sensors (e.g. Cui's nanowires nanosensors) be made to test the applicability of the semiconductor microwires in analytical chemistry.

Reference:

1. Barton, A. C.; Collyer, S. D.; Davis, F.; Gornall, D. D.; Law, K. A.; Lawrence E. C. D.; Mills, D. W.; Myler, S.; Preitchard, J. A.; Thompson, M.; Higson, S. P. J. *Biosensors Bioelectronics* **2004**, *20*, 328.
2. Cui, Y.; Wei, Q.; Park, H.; Lieber, C. M. *Science* **2001**, *293*, 1289